



저작자표시-비영리-변경금지 2.0 대한민국

이용자는 아래의 조건을 따르는 경우에 한하여 자유롭게

- 이 저작물을 복제, 배포, 전송, 전시, 공연 및 방송할 수 있습니다.

다음과 같은 조건을 따라야 합니다:



저작자표시. 귀하는 원저작자를 표시하여야 합니다.



비영리. 귀하는 이 저작물을 영리 목적으로 이용할 수 없습니다.



변경금지. 귀하는 이 저작물을 개작, 변형 또는 가공할 수 없습니다.

- 귀하는, 이 저작물의 재이용이나 배포의 경우, 이 저작물에 적용된 이용허락조건을 명확하게 나타내어야 합니다.
- 저작권자로부터 별도의 허가를 받으면 이러한 조건들은 적용되지 않습니다.

저작권법에 따른 이용자의 권리는 위의 내용에 의하여 영향을 받지 않습니다.

이것은 [이용허락규약\(Legal Code\)](#)을 이해하기 쉽게 요약한 것입니다.

[Disclaimer](#)

Ph.D. Dissertation of Engineering

**Synthesis and Functionalization of
Superparamagnetic Iron Nanoparticles for Imaging
of Subsurface Reservoirs**

지하 영상화 분야에 사용될 수 있는 초상자성 산화철
나노입자의 합성 및 기능화

February 2020

Graduate School of Engineering
Seoul National University
Energy System Engineering

Yongtae Park

Abstract

Recently, the application of nanoparticles to petroleum engineering has received significant research attention. Two important considerable factors in nanoparticle-aided petroleum engineering are the cost of nanoparticle synthesis and dispersion stability of nanoparticles under harsh subsurface conditions like high salinity. In this thesis, a process for the synthesis of superparamagnetic iron oxide nanoparticles (SPIONPs) for subsurface imaging that addresses these two factors is discussed. The SPIONPs are synthesized from steelwork byproducts during the pickling process. Using steelwork byproducts as a rich source of iron ions, high-quality SPIONPs are synthesized by co-precipitation methods. A functionalization method was developed wherein SPIONPs exhibit a stable dispersion in concentrated brine. Functionalizing SPIONPs with conventional polymers such as polyethylene glycol (PEG), polyvinyl alcohol (PVA), and polyacrylic acid (PAA) renders the stable dispersion of SPIONPs extremely difficult under high salinity. However, by functionalizing SPIONPs with sulfonated phenolic resin (SPR), a stable dispersion in 5 wt% NaCl solution at neutral to basic pH is achieved. SPR can be synthesized by mixing and heating 4-hydroxy benzene sulfonic acid and formaldehyde at a molar ratio of 1:1. Subsequently, by co-precipitating SPIONPs in an SPR solution, a one-pot synthesis/functionalization of SPIONPs is achieved. Furthermore, to improve the stability in acidic medium, the SPR shell stability is crosslinked with PVA. Consequently, a stable dispersion in 5 wt% NaCl solution under acidic conditions is achievable. Furthermore, from the crosslinking, the SPIONPs showed an enhanced dispersion stability in the presence of divalent cations such as calcium ions. Further, detailed characterizations of synthesized nanoparticles are conducted using size distribution analysis, zeta potential

measurements, TEM imaging, EDS mapping, vibrating sample magnetometer analysis, and thermogravimetric analysis. In summary, a synthesis process of SPIONPs is developed, which is applicable to subsurface imaging in oil well development; this was achieved by: (i) synthesizing SPIONPs from low-cost ingredients such as the byproducts from steelworks processes, (ii) utilizing low-cost polymers for functionalization of the nanoparticles, and (iii) mixing as well as heating reagents without using complicated processes.

Keywords: iron oxide nanoparticles; nanoparticle dispersion; surface functionalization; salinity tolerance; sulfonated phenolic resins; one-step functionalization

Student Number: 2013-23179

Table of Contents

List of Figures	vi
List of Tables	xi
Chapter 1. Introduction	1
1.1. Nanotechnology and the Petroleum Industry	1
1.1.1. Oil Field Exploration and Development.....	4
1.1.2. Oil Well Stimulation and Production.....	6
1.1.3. Enhanced Oil Recovery	8
1.1.4. Produced Fields Processing	11
1.2. Thesis Research Objectives.....	12
1.3. Synopsis of Thesis	14
Chapter 2. Research Background.....	15
2.1. Recycling of Pickling Solution from Steelworks Process	15
2.2. Superparamagnetic Iron Oxide Nanoparticles	17
2.2.1. Magnetism and Superparamagnetic Iron Oxide Nanoparticles.....	17
2.2.2. Synthesis of Superparamagnetic Iron Oxide Nanoparticles.....	20

2.3. Particle Dispersion Theory	26
2.4. Functionalization of Superparamagnetic Iron Oxide	
Nanoparticles	29
2.4.1. Functionalization by Small Organic Molecules	30
2.4.2. Functionalization by Polymers	33
2.4.3. Functionalization by Inorganic Materials	35
Chapter 3. Materials and Methods.....	39
3.1. Synthesis of Superparamagnetic Iron Oxide Nanoparticles	
from Steelworks Byproducts.....	40
3.2. Functionalization of Superparamagnetic Iron Oxide	
Nanoparticles with Several Polymers	43
3.3. Functionalization of Superparamagnetic Iron Oxide	
Nanoparticles with Sulfonated Phenolic Resin	46
3.4. Functionalization of Superparamagnetic Iron Oxide	
Nanoparticles with Crosslinked Shell of SPR and PVA	49
3.5. Analysis of Physical and Chemical Properties of Synthesized	
Nanoparticles.....	51
Chapter 4. Results and Discussion.....	54
4.1. Synthesis of Superparamagnetic Iron Oxide Nanoparticles	
from Steelworks Byproducts.....	54
4.2. Functionalization of Superparamagnetic Iron Oxide	

Nanoparticles with Several Polymers	63
4.3. Functionalization of Superparamagnetic Iron Oxide	
Nanoparticles with Sulfonated Phenolic Resin	66
4.4. Functionalization of Superparamagnetic Iron Oxide	
Nanoparticles with Crosslinked Shells of SPR and PVA.....	81
4.5. Discussions and Further Studies	92
Chapter 5. Conclusions	95
References	98
Appendix	119
A. 1. van der Waals Interaction	119
A. 2. Electrostatic Interaction	125
초 록	131

List of Figures

- Figure 1.1** Tendency of nanotechnology-assisted research in the petroleum industry. The number of journal papers was obtained from OnePetro..... 3
- Figure 3.1** Synthetic process of the superparamagnetic iron oxide nanoparticles: (a) iron oxide steelworks byproduct samples; (b) Fe³⁺ solution leached from (a); (c) Fe²⁺ solution reduced from (b); and (d) final synthesized superparamagnetic iron oxide nanoparticles separated from the solution by magnetic separation. 42
- Figure 3.2** The molecular structure of polyethylene glycol (PEG), polyvinyl alcohol (PVA), and polyacrylic acid (PAA)..... 44
- Figure 3.3** Synthesis procedure of sulfonated phenolic resin by condensation polymerization between 4-hydroxy benzene sulfonic acid and formaldehyde..... 48
- Figure 3.4.** Acid–base reaction between sulfonated phenolic resin and an iron oxide nanoparticle surface..... 48
- Figure 4.1** XRD spectra of the steelworks byproducts sample used for the experiments. 55
- Figure 4.2** Zeta potential vs. pH curve of bare superparamagnetic

iron oxide synthesized from steelworks byproducts.....	57
Figure 4.3 (a) TEM image of superparamagnetic iron oxide nanoparticles synthesized from steelworks byproducts. (b) The same particles at higher magnitude. Diameters of some primary particles were measured.....	58
Figure 4.4 Primary particle distribution of the SPIONPs synthesized from steelworks byproducts.....	59
Figure 4.5 XRD spectra of the magnetite nanoparticles synthesized from steelworks byproducts.....	61
Figure 4.6 Magnetization curve of the SPIONPs synthesized from steelworks byproducts, and the same curve near the origin (inset). As shown in the inset, the hysteresis is very small that is a key property of superparamagnetism.	62
Figure 4.7 Dispersions of superparamagnetic iron oxide nanoparticles treated with polyethylene glycol (left), polyvinyl alcohol (middle), and polyacrylic acid (right), seven days after the synthesis of each dispersion.	64
Figure 4.8 Dispersion stability test of PEG-, PVA-, and PAA-treated superparamagnetic iron oxide nanoparticles in 5 wt% NaCl brine. After 1 day, all the dispersions became lightened and visual confirmation of sedimentation was made.....	64
Figure 4.9 Size distribution of the SPR-SPIONPs analyzed by	

dynamic laser scattering.....	67
Figure 4.10 Zeta potential vs. pH curve of superparamagnetic nanoparticles without any further treatment (bare SPIONP, ×), and sulfonated phenolic resin-treated samples (SPR-SPIONP, •).....	68
Figure 4.11 (a) TEM image of SPR-SPIONPs on a holey carbon grid at a low magnification; (b) the same sample at a higher magnification.....	71
Figure 4.12 Primary particle size distribution of the SPR-SPIONP.....	71
Figure 4.13 STEM-EDS analysis of the SPR-SPIONP sample for mapping the distribution of Fe and S elements: (a) squared area in this picture indicates where the analysis was conducted; (b) distribution of Fe elements in the squared area in (a); (c) distribution of S elements.....	72
Figure 4.14 Thermogravimetric analysis of SPR-SPIONPs.	74
Figure 4.15 Magnetization curve (Langevin) of SPR-SPIONPs, and the same curve near the origin (inset).....	76
Figure 4.16 Calculation of magnetic susceptibility of SPR-SPIONP.....	76
Figure 4.17 Dispersion stability of SPR-SPIONP dispersion in 5 wt% NaCl solutions at several pH values over one week. From pH	

7 to 10, the dispersion stayed stable, while in acidic conditions the dispersion formed aggregate and settled.....	78
Figure 4.18 Stable dispersion of SPR-SPIONPs achieved in 10 wt% NaCl solutions at pH 10.....	78
Figure 4.19 STEM-EDS analysis of freshly prepared SPR-SPIONP (a, b), and the same sample put in a 5 wt% NaCl solution at pH 4 (c, d).	80
Figure 4.20 Size distribution of SPR-SPIONP and crosslinked SPR-SPIONP.	83
Figure 4.21 pH–zeta potential curve of superparamagnetic iron oxide nanoparticles with SPR.	84
Figure 4.22 Dispersions of SPR-SPIONPs with PVA crosslink after one week in sodium chloride solutions. Compared to the dispersion without salt addition, no change in color or formation of sedimentation was observed.	85
Figure 4.23 Dispersions of SPR-SPIONP with PVA crosslink in API brine (8 wt% NaCl + 2 wt% CaCl₂ solution).....	85
Figure 4.24 Crosslinking process of sulfonated phenolic resin and polyvinyl alcohol.	87
Figure 4.25 (a) TEM image of crosslinked SPR-SPIONP and (b) an image of the same sample at a higher magnitude.	89
Figure 4.26 STEM-EDS analysis of crosslinked SPR-SPIONP (a, b),	

and the same sample put in a 5 wt% NaCl solution at pH 4 (c,
d)..... 90

**Figure A.1 Visual aid for calculation of the London–van der Waals
force. A sphere with radius R is cut out by a sphere around P
at a *distance* of $OP = R$ 121**

**Figure A.2 Visual aid for calculation of the London–van der Waals
force. A similar method to that formerly described is applied
for a second sphere of radius R_2 123**

Figure A.3 A typical potential graph for DLVO interaction. 130

List of Tables

Table 2.1 Estimated Dc <i>value</i> of some magnetic materials (Lu et al., 2007).	20
Table 2.2 Sizes of anions forming the iron precursor salts (Yazdani and Seddigh, 2016).	23
Table 4.1 A composition of the steelworks byproducts analyzed from XRF spectra.	54
Table 4.2 Atomic ratio between Fe and S at the spots indicated in Figure 4.19a and c, determined by STEM-EDS analysis....	79
Table 4.3 Atomic ratio between Fe and S at the areas indicated (orange square) in Figure 4.26a and c determined by STEM-EDS analysis	91

Chapter 1. Introduction

1.1. Nanotechnology and the Petroleum Industry

Nanotechnology deals with materials that exhibit sizes smaller than 100 nm. There are significant differences in the physical properties of materials at nanoscale; this is because of the influence of surface and quantum phenomena. Further, nanotechnology has been receiving remarkable interest from researchers in electronics, biology, chemistry, pharmacology, and energy (Bruchez et al., 1998; Dobson, 2006; Michalet et al., 2005; Narayanan and El-Sayed, 2005).

In the petroleum industry, advancements in applications of nanomaterials and nanotechnology in areas such as exploration, drilling, refining, and enhanced oil recovery (EOR) (Figure 1) are steadily investigated. Regardless of the numerous engineering challenges in the petroleum industry, new problems are emerging from the development of unconventional oil reservoirs such as shale gas, and numerous researchers have addressed such problems by incorporating nanotechnology (Agista et al., 2018). Previous research on petroleum has primarily focused on the extremely small sizes and easily changeable behavior of nanomaterials (Kapusta et al., 2011). Majority of the studies consider methods for enhancing the recovery rates in oil production by using nanoparticles, which are functionalized to have specific properties

(Krishnamoorti, 2006).

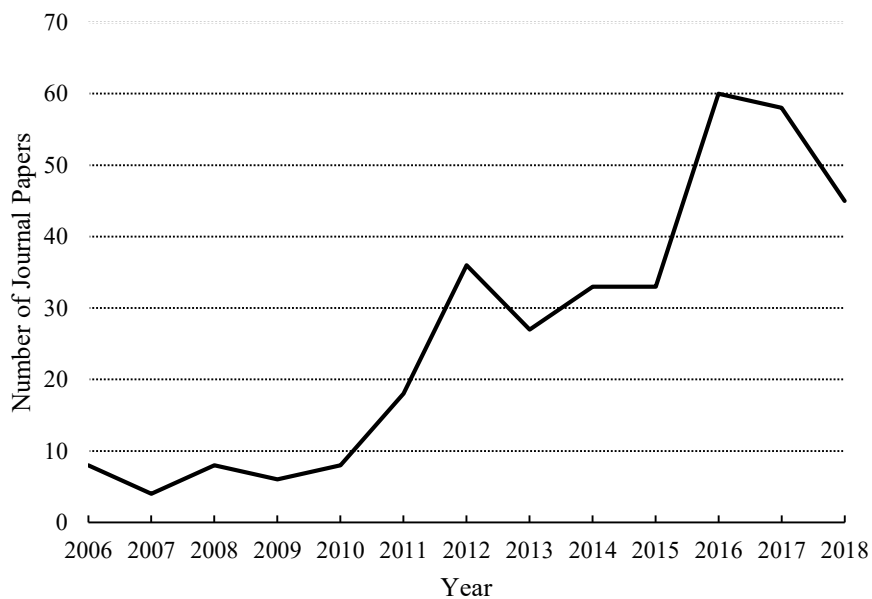


Figure 1.1 Tendency of nanotechnology-assisted research in the petroleum industry. The number of journal papers was obtained from OnePetro.

1.1.1. Oil Field Exploration and Development

In oil field exploration, the use of nanomaterials is a possible feasible solution to numerous problems arising from exploration and development processes in oil wells. A typical application is the use of nanomaterials as nanosensors for use in underground oil reservoirs. Nanoparticles injected into an underground reservoir can act as sensitive sensors for parameters such as temperature, pressure, and stress (Krishnamoorti, 2006). Although the average diameter of pores in conventional oil reservoir rocks is often larger than 2 μm and 30 μm in high-quality reservoirs, it is smaller than 1 μm in unconventional oil reservoirs such as shale gas reservoirs (Liu et al., 2016). Consequently, the interest for incorporating nanosensors in oil reservoirs is steadily increasing. Nanoparticles pass through small underground pores without plugging them; this is achieved because of their extremely small size. Agenet et al. (2012) studied a method for monitoring physicochemical conditions such as pH, temperature, and oil ratio of reservoirs by injecting fluorescent silica nanobeads into an oil reservoir.

Additionally, injecting nanoparticles can change the physicochemical properties of a reservoir. Researchers from the University of Texas at Austin studied a method to enhance the quality of electromagnetic exploration in oil reservoirs by injecting superparamagnetic iron oxide nanoparticles (SPIONPs) (Rahmani et al., 2015). SPIONPs if injected into an oil reservoir cause a magnetic gradient with respect to the reservoir against the background. The

magnetic gradient enables the underground structure to be identified through electromagnetic exploration.

In the drilling process, nanoparticles are used to enhance the quality of the drilling fluid. Nanoparticle-based drilling fluids improve the rheology and thermal stability of the drilling fluid. A drilling fluid containing SnO₂ nanoparticles shows an improved performance in the presence of KCl salt, particularly at high-temperature and high-pressure conditions (Parizad and Shahbazi, 2016). Drilling fluids containing nanoparticles are used to stabilize underground reservoirs. In shale gas drilling, oil-based mud is preferred over water-based mud because water can invade the shale structure causing swelling, delaminating, fracturing, and partial dissolution of the structure (Guo et al., 2012). However, adding silica nanoparticles to the water-based mud reduces the invasion of water into the shale by 10 to 100 times. Base on this reduction, a shale gas reservoir can be stably maintained particularly during water-based drilling (Sharma et al., 2012).

In the completion procedure of a well, nanomaterials can be used to enhance the mechanical properties of the cement used. It is noted that the addition of modified nanoclay synthesized from montmorillonite leads to a reduction in the permeability and porosity, and enhances the compressive strength of the cement at high-pressure and high-temperature conditions. This occurs because smaller nanoclay particles fill the capillaries of the cement paste, densifying the matrix (Murtaza et al., 2016). Nanomaterials that are sourced from carbon materials, such as carbon nanotubes (CNT) and graphene nanoplatelets, can be used to enhance the properties of cement. Addition of such

materials to cement slurry enhances the yield strength and rheological behavior of the cement. This is attributed to the increased degree of hydration and reduced pores (X. Sun et al., 2017).

1.1.2. Oil Well Stimulation and Production

Recently, researchers have developed methods to improve the efficiency of oil well stimulation and production process using nanomaterials.

Hydraulic fracturing process introduces artificial fractures into underground rocks that contain oil and gas; this is aimed at achieving a higher production of oil and gas by increasing their flow conductivity. Polymers, viscoelastic surfactant (VES) fluid, and slick water are often used in typical hydraulic fracturing processes. However, there are some limitations to overcome if using these hydraulic fluids. At high-temperature and high-pressure underground conditions, these fluids do not retain enough viscosity for the hydraulic fracturing process (Al-Muntasheri et al., 2017). Additionally, in reservoirs with moderate (200 md) permeability, high leak off rates occur for the VES fluid (Crews et al., 2008b; Sullivan et al., 2006). Adding nanomaterials to such fluids improves the efficiency of the fracturing process. Researchers at the University of Oklahoma demonstrated an improvement in the viscosity of guar-based fracturing fluid by adding 20 nm SiO₂ nanoparticles. They changed the concentration of nanoparticles from 0.058 wt% to 0.4 wt%, and selected a fracturing fluid that contained 0.058 wt% of nanoparticles as optimal with regard to the performance evaluation and economic analysis (Fakoya and Shah,

2014). Researchers at the Aramco Research Center reported that adding nanoparticles from metal oxide to a polymer fluid causes the fluid viscosity to exceed 500 cP at high temperatures beyond 300 °F (about 150 °C). By adding selected nanoparticles to the polymer fluid, the nanoparticles and polymer molecules undergo attractive interactions. The attractive force between particles and polymer chains enhance the viscosity of hydraulic fracture fluids particularly at high-temperature (Li et al., 2016). VES fluid can be improved by the addition of nanoparticles. VES fluids comprise smaller surfactant molecules than those in polymers. If the concentration of the surfactant is higher than the critical micelle concentration, the apparent viscosity of the fluid increases as the surfactant molecules form micelles and entangle together (Hull et al., 2016). However, VES fluids tend to have higher leak off rates because of their low molecular weights and the inability to form crosslinks between molecules (Crews et al., 2008b; Sullivan et al., 2006). Addition of nanoparticles is a potential solution to this problem. Some pyroelectric nanoparticles behave as pseudo-crosslinkers in VES fluid systems that can pseudo-crosslink micelles by electrostatic and van der Waals interactions. This improves viscosity by 50% (Crews et al., 2008a).

Attempts have been made to use nanoparticles as proppants for fracturing processes. Although a tight shale gas reservoir has low permeability and high brittleness properties, injection of nano-sized proppants into the reservoir prevents the collapse of nano-sized fractures and improves the total fracture conductivity. Bose et al. (2015) demonstrated the availability of fly ash nanoparticles as nano-proppants. They measured the elastic moduli of fly ash

at nanoscale to determine whether nanoparticles withstand stress from underground reservoirs. Fluid loss tests and an American Petroleum Institute (API) fracture conductivity test were performed. During the use of nanopropants, a fluid loss reduction of crosslinked guar solutions was observed, and 27–33 mD of fracture permeability was generated.

1.1.3. Enhanced Oil Recovery

After primary and secondary recovery processes of an oil well, it is observed that there is still 70% OOIP (original oil in place) remaining in the oil reservoir. The EOR process recovers the residual oil from the reservoir by the injection of other fluids or agents. The mechanisms of the EOR process primarily increases the mobility of the displacement medium by augmenting the water viscosity, decreasing the oil viscosity, or both; further, the solvent extraction of oil and a reduction in the oil–water interfacial tension with respect to the surfactant is also employed (Lake et al., 1992).

Polymer flooding is often employed in the EOR process. With water-soluble polymers such as polyacrylamide, xanthan gum, and associated polymers, non-Newtonian rheological behaviors may occur leading to an improvement in viscosity. However, the viscosity effect of the polymer is reduced if it is adsorbed onto the underground rocks (Ali et al., 2018). Adding nano-silica or nanoclay to the polymer solution reduces the adsorption of polymer onto sandstone and carbonate rocks (Cheraghian et al., 2014). Based on the experimental data on polymer solution with nanoparticles, Khalilinezhad

and Cheraghian (2016) showed a reduction in polymer adsorption with chemical modeling. Moreover, the viscosity of the polymer liquid is improved because nanoparticles and polymer chains can interact by hydrogen bonding, which leads to a crosslinking of the polymers (Khalilinezhad et al., 2017).

Surfactant flooding is applied in the EOR process to reduce interfacial tension between the oil and water, and to decrease the capillary pressure in porous media (Ali et al., 2018; Jamaloei et al., 2009). Additionally, injection of surfactant alters the wettability of the reservoir rocks from oil-wet to strong water-wet, which dissociates the oil from the reservoir rocks (Negin et al., 2017). For surfactant flooding, anionic surfactants are frequently used owing to their lower adsorption onto sandstone rocks. Cationic surfactants are often used to change the wettability of carbonate rocks from oil-wet to water-wet (Sheng, 2011). The efficiency of surfactant flooding is observed to affect factors such as temperature and salinity. It is noted that beyond the cloud point temperature and Krafft temperature, the efficiency of anionic surfactants decreases; this is because if the surfactant begins to form micelles, the addition of the surfactant does not reduce the interfacial tension (Karnanda et al., 2013; Manshad et al., 2017). Moreover, the performance of surfactants reduces in the presence of salinity because its solubility decreases. Additionally, a surfactant loss occurs if it gets adsorbed onto the reservoir rocks (Ahmadi and Shadizadeh, 2012, 2013; Paria and Khilar, 2004). These factors are significant problems that need to be addressed for achieving optimal surfactant flooding. To address these problems, researchers have sort to the synergetic effect that is produced by using nanoparticles and surfactants together. Further, the effect of adding SiO₂

nanoparticles to surfactants has been examined. Mixtures of SiO₂ nanoparticles showed a better interfacial tension reduction between oil and brine, and a lower adsorption of surfactant onto the rock surfaces. Moreover, surfactant flooding with SiO₂ nanoparticles exhibit a better stability at high temperature, i.e., approximately 95 °C (Le et al., 2011; Zargartalebi et al., 2014).

Because CO₂ injection is a cost-effective method for EOR and reduces greenhouse gas, several studies have been conducted on CO₂-EOR recently (Chu and Majumdar, 2012; Jarrell, 2002; Lambert et al., 1996). However, the low viscosity and density of CO₂ causes flow instabilities including viscous fingers, gravitational segregation, and thief zones, resulting in a reduction in the efficiency of CO₂-EOR (Rognmo et al., 2018). However, the use of CO₂-foam injection can address such problems. By the generation of foam, the gas mobility of CO₂ is reduced and the sweep efficiency is improved (Heller et al., 1985). However, the foam is in a thermodynamically unstable state, which requires stabilizers like surfactants to achieve long-term stability. Although surfactant-stabilized CO₂-foam injection is technically successful for foam formation and an improved sweep efficiency (Henry et al., 1996; Jarrell, 2002; Jonas et al., 1990), it has some limitations. The majority of these limitations are found in similar areas to the surfactant flooding EOR method. At high-temperature and high-salinity, the surfactants become unstable, and the surfactant molecules adsorb onto the underground reservoir rock surfaces. Utilizing the solid nanoparticles can be a solution to these limitations. Dickson et al. stated that silica nanoparticles behave as stabilizers for the CO₂ in water emulsion without using surfactant. Based on this study, the emulsion stability

improved with the increasing particle concentration. The particle hydrophilicity decreased from 100% SiOH to 76% SiOH (Dickson et al., 2004). Fu et al. (2018) found that silica nanoparticles stabilizes supercritical CO₂ foam particularly during the process of oil displacement. The pressure gradient was three to five times higher than that obtained without the foaming agent, which is demonstrated during the co-injection of nanoparticles and CO₂. The nanoparticle-stabilized CO₂ foam increased the oil recovery. Lee et al. (2015) studied a method of stabilizing CO₂ foam using inexpensive fly-ash nanoparticles. Fly ash is mechanically ground in two stages, with bigger grinding media in the first stage, and smaller grinding media in the second stage. The resulting nano-sized fly ash particles formed stable CO₂ water emulsion without any treatment. Fly ash, which contained unburned carbonaceous materials and minerals, behaved as surfactants; this led to the stabilization of the CO₂ emulsion. The emulsion stability increased with the increasing carbon content in the fly ash.

1.1.4. Produced Fields Processing

After crude oil production, the refining process is required to crack long hydrocarbon chains into smaller ones, and to remove impurities like sulfur. To make the process more cost-effective and energy-efficient research on the application of nanocatalysts to the refining field because nanocatalysts have higher surface-area-to-volume ratio than conventional catalysts to increase efficiency have been carried out (Ying and Sun, 1997). Mohammed et al. (2017)

produced a nanocatalyst for hydrodesulfurization by implanting CoMo within a multiwall CNT structure, 2017). Lam-Maldonado et al. (2018) synthesized NiFe nanocatalysts with several molar ratios of nickel and iron (1:0.33, 1:1, and 1:3) for the hydrocracking process for heavy crude oil. With the synthesized nanocatalyst, the API gravity increased from 13.1 to 18.3, and 37.2–43.7% of asphaltene conversion was achieved. Also, studies on refining water produced during the oil production process with nanoparticles have been conducted. Researchers from the University of Texas at Austin studied a method of removing oil droplets from produced water using SPIONPs (Ko et al., 2016). Using the nature of oil droplets having negative surface charge in water, they removed oil droplets by attaching them electrostatically onto SPIONPs functionalized to have positive surface charge. After attachment, the SPIONPs with oil droplets were removed by magnetic separation. Using this method, 96.4–99.5% of the oil droplets in water were removed.

1.2. Thesis Research Objectives

As described in the Section 1.1, several studies have been conducted on utilizing nanotechnology in the petroleum industry. The application of nanotechnology can be a breakthrough for many challenges in the petroleum industry.

Underground flow monitoring is a typical challenge. Monitoring the water flow during the drilling, water flooding, and EOR processes can give guidelines for drilling and managing an oil well, enabling cost reductions. Rahmani et al.

(2015) proposed a method to monitor the underground water flow by combining the injection of magnetic nanoparticles to the reservoir and cross-well electromagnetic tomography.

The cross-well electromagnetic tomography method was previously proposed as one of the methods to develop an underground model (Wilt et al., 1995). With a low-frequency cross-well electromagnetic field, subsurface conductivity information can be identified. From this information, the porosity, water saturation, and temperature of the reservoir can be determined (Patzek et al., 2000). If SPIONPs are injected into an underground oil reservoir, the nanoparticles behave as a contrast agent to visualize the water flow underground with electromagnetic tomography.

There are many limitations to overcome in injecting SPIONPs underground. The high temperature, salinity, and pressure conditions underground reduce the dispersion stability of nanoparticles, disabling their physical properties like small size and large surface-area-to-volume ratio. Particularly, if the sizes of the nanoparticles are increased, they can get trapped in underground pores. The underground pores of conventional sandstone is averagely 0.2 μm at tubular opening (Hu, 2017), and smaller in unconventional oil reservoirs such as tight sandstone, and shale gas. Therefore, a proper treatment for SPIONPs is required to prevent aggregation in harsh conditions in the underground oil reservoir. To address these, the following studies are conducted. The main objective of this thesis is to explore how to synthesize and functionalize SPIONPs that are stably dispersed under high-salinity conditions of an underground oil reservoir. To achieve this, a method of synthesizing and

functionalizing SPIONPs from low-cost precursors through a simple synthesis process will be discussed. As a precursor to synthesizing SPIONPs, iron-rich steelwork byproducts and for functionalization, sulfonated phenolic resin were selected. Sulfonated phenolic resin is synthesized from inexpensive monomers by a simple mixing and heating method, and impart strong negative charge onto the SPIONPs with their rich sulfonate group. Subsequent chapters will describe a method to synthesize and functionalize SPIONPs using these materials. Additionally, the synthesized SPIONPs will be analyzed to determine whether their dispersion stability is improved compared to SPIONPs functionalized using widely used polymers.

1.3. Synopsis of Thesis

This thesis proposes a cost-competitive method of synthesizing and functionalizing SPIONPs that are stably dispersed under high-salinity conditions. Before presenting the details, the scientific background of this research is presented in Chapter 2. Then, the detailed procedure of the synthesis and functionalization of SPIONPs and analysis method of the synthesized particles is discussed in Chapter 3. From the results of the analysis, scientific discussion will be presented in Chapter 4. Finally, the conclusion and summing-up of the thesis will be presented in Chapter 5.

Chapter 2. Research Background

2.1. Recycling of Pickling Solution from Steelworks Process

In steelwork processes, surfaces of iron is oxidized because of its high temperature. To wash the oxidized layer, acid solution is used, and this process is called 'pickling step'. Afterwards, the metal-rich pickling solution is produced as a by-product. The metal content of the solution may be up to 250g/L (Regel-Rosocka, 2010). For the process, acids such as hydrochloric acid, nitric acid, sulfuric acid, hydrofluoric acid and their mixtures are used. Also, the pickling solution can contain some additives such as surfactants, inhibitors, and stabilizers to enhance its performance. Because of such chemicals in the pickling solution, it must be hazardous for environment if such solutions are just released. Therefore, it is recommended that recycling the pickling solution (Regel-Rosocka, 2010).

The main two process of recycling pickling solution is acid recovery and metal recovery. For acid recovery, membrane techniques (Negro et al., 2001; Tomaszewska et al., 1995). pyrometallurgical process (Dutrizac and Monhemius, 1986) and evaporation method are usually employed (Kerney et al., 1994). Membrane techniques use a permeable membrane, and recovers acid by diffusion. Pyrometallurgical and evaporation method both are heating the

pickling solution and recover the acid by evaporating them. The metal ions inside the solution are precipitated down in forms of oxides or ionic salts. Pyrometallurgical method is operated at high temperature such as 450 °C, and is effective for treating large amount of pickling solution (Dutrizac and Monhemius, 1986). Also, the metal ions can be recovered in forms of oxide too. However, the energy consumption of the method is high resulting in an increase in operation costs, and emission of exhaust gases that are unfriendly to the environment. Evaporation method is operated at lower temperature than pyrometallurgical method such as 80 °C, that reduces operation costs. However, the precipitated ionic materials containing high chloride and sulfate is hazardous.

For the metal recovery from pickling solutions, ion exchange resins, crystallization method, and solvent extraction methods are employed. Using strong basic ion-exchange resins, metal chlorocomplexes are extracted from pickling solutions. By employing this method, Fe ions can be separated from Zn ions and hydrochloric acid (Marañón et al., 1999). Crystallization method separates metal ions by difference in the solubility between acids and metal ions in water. By simply cooling the solution, the pure salt of iron could be produced (Özdemir et al., 2006). In pilot plant studies, the method showed results of reducing waste processing and chemical consumptions. However, there is a risk of scale formation in the crystallizer. Solvent extraction method is conventionally used to extract specific ions from solutions. The technique applying the method to recover metal ions from pickling solution has already been developed in the 1980s (Dutrizac and Monhemius, 1986). However,

facilities using this technique are not currently in operation because this approach is suitable for large-scale operations, and is not economically attractive for extracting metal ions from pickling solutions (Kentish and Stevens, 2001).

Based on the above discussion, it is common to recover only acid and metal ions if recycling steel mill byproducts. However, beyond that, the ability to synthesize SPIONPs from the steelworks byproducts will lead to higher economic values.

2.2. Superparamagnetic Iron Oxide Nanoparticles

SPIONPs has garnered the interest of numerous researchers for decades because of their unique properties that distinguish them from bulk materials, like low coercivity, high magnetic susceptibility, and superparamagnetism. Many investigations on the application of SPIONPs to drug delivery, magnetic resonance imaging, hyperthermia, sensing, etc. have been conducted using these physicochemical properties (Dobson, 2006; Feng et al., 2008; Kim et al., 2006; Yu and Chow, 2004).

2.2.1. Magnetism and Superparamagnetic Iron Oxide Nanoparticles

An important property of superparamagnetic iron oxide nanoparticles is

their unique magnetic property known as “superparamagnetism”. Bulk magnetic iron oxide contains multiple “magnetic domains” where magnetic moments are arranged in parallel. This alignment of the magnetic moments makes bulk magnetite stay magnetized after an external magnetic field is removed, and this magnetic property is called ferromagnetism. However, if a magnetic iron oxide particle becomes sufficiently small to have only a single magnetic domain, thermal energy continuously changes the orientation of the magnetic moment of the particle if no external magnetic field is applied. Because this behavior is similar to that of paramagnetic particles, it is called “superparamagnetism” (Brown, 1963).

If a magnetic field is applied to a single-domain ferromagnetic particle, the particle is magnetized by the magnetic field. After the removal of the magnetic field, the residual magnetization M_t of the particle over time is expressed as below (Bean and Livingston, 1959):

$$M_t = M_s \exp\left(-\frac{t}{\tau}\right) \quad (1),$$

where M_s is saturation magnetization, t is time after the removal of the external magnetic field, and τ is the relaxation time of the particle. If a single-domain particle has anisotropic magnetic properties, there are two possible stable orientations of the magnetic moment. The relaxation time is the mean time required for the magnetic moment to flip from one stable orientation to another. According to the Néel–Arrhenius equation, the relaxation time τ_N of the particle

is described as below (Neel, 1949):

$$\tau_N = \tau_0 \exp\left(\frac{K_{\text{eff}}V}{k_B T}\right) \quad (2),$$

where K_{eff} is the magnetic anisotropy energy density of the particles, and V is the volume of the particles. Typically, τ_0 has a value between 10^{-10} s and 10^{-9} s. If the relaxation time of the particle becomes sufficiently short compared to the observation time, the residual magnetization will be removed instantly, while showing similar behavior to paramagnetic materials. While τ_N has exponential dependence on the volume of the particles, it can be seen that particles with sufficiently small size will show superparamagnetic properties (Bean and Livingston, 1959).

The critical diameter D_c of a spherical particle, below that the particle can only have a single domain, is expressed as below:

$$D_c \approx 18 \frac{\sqrt{AK_{\text{eff}}}}{\mu_0 M_s^2} \quad (3).$$

This value is important for synthesizing magnetic nanoparticles because the primary size of the particles must be less than this value for them to have superparamagnetism. From the formula, estimated D_c values of some magnetic materials are listed in Table 2.1 (Lu et al., 2007).

Table 2.1 Estimated D_c value of some magnetic materials (Lu et al., 2007).

Material	D_c [nm]
fcc Co	15
fcc Co	7
Fe	15
Ni	55
SmCo ₅	750
Fe ₃ O ₄	128

2.2.2. Synthesis of Superparamagnetic Iron Oxide Nanoparticles

As the critical diameter of magnetite is 128 nm (Table 2. 1), it is necessary to synthesize magnetic iron oxide particles smaller than 128 nm to make use of their superparamagnetic properties. To achieve this, many synthesis methods have been proposed by researchers. Among them, methods such as co-precipitation and thermal decomposition are the most widely used, and each method has its advantages and disadvantages.

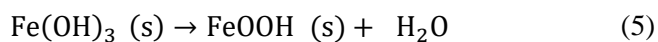
The mechanism of nanoparticle nucleation and growth can be explained by the LaMer mechanism. If the concentration of monomers of nanoparticles in solution increases rapidly, “burst nucleation” occurs. After burst nucleation, no more nucleation occurs because of the low concentration of monomers. The particles then grow by diffusion of monomers in solution or Ostwald ripening

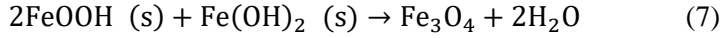
(Lamer and Dinegar, 1950; Thanh et al., 2014). Because almost all monomers is consumed during the nucleation phase, the growth of the particles is limited. Therefore, the particle size is reduced. Moreover, the particle size distribution is narrowed because most particles are formed during the nucleation phase and grow for a similar growth time.

After the synthesis, the magnetite nanoparticles can easily change to maghemite ($\gamma\text{-Fe}_2\text{O}_3$) because of their unstable nature. However, these two materials have almost the same physical properties, except that the maghemite has slightly smaller magnetic susceptibility than magnetite. Therefore, it is difficult and not necessary to distinguish the two materials from each other. Consequently, these two materials are often collectively called superparamagnetic iron oxide nanoparticles (SPIONPs).

2.2.2.1. Co-precipitation Method

The co-precipitation method is one of the most popular methods for the synthesis of SPIONPs from aqueous solution because of its convenience and reproducibility (Lu et al., 2007). By addition of base to an Fe^{2+} and Fe^{3+} ion mixture solution, the SPIONPs are precipitated out by the following reactions.





The overall reaction can be described as follows (Mascolo et al., 2013).



There can be several sources of iron ions, such as chlorides, nitrates, and sulfates, and several bases can be used like sodium hydroxide, potassium hydroxide, and ammonium hydroxide. By varying the reaction conditions, such as the type of salts used, kind of base used, reaction temperature, and pH value, the size, shape, and composition of SPIONPs can change. Yazdani et al. (2016) studied the effect of iron precursors to synthesized SPIONPs. For the study, $\text{FeCl}_2 \cdot 4\text{H}_2\text{O}$ and $\text{FeSO}_4 \cdot 7\text{H}_2\text{O}$ were selected as ferric ion precursors, and $\text{FeCl}_3 \cdot 6\text{H}_2\text{O}$, $\text{Fe}_2(\text{SO}_4)_3$, $\text{Fe}(\text{NO}_3)_3 \cdot 9\text{H}_2\text{O}$ was selected as a ferrous ion precursor. Six combinations of these compounds were examined for SPIONP synthesis with regard to the particle mean size, morphology, and magnetic properties. It was found that the mean size and magnetic susceptibility of the SPIONPs were increased in the order of sulfates, nitrates, and chlorides. This tendency was explained by the differences in ionic strength and ionic diameter of each salt. If the ionic strength changes, the electrostatic surface charge density of the particles changes in relation to the particle-solution interfacial tension, resulting in changes to the particle size (Jolivet et al., 2004). Moreover, if the anion size of the precursor increased, the diffusion layer of the electric double layer around the particle thickened, which hindered the monomer from diffusing to the as-

synthesized nuclei. The sizes of anions are listed in Table 2. 2. From the table it can be seen that the anion size of the sulfate is the biggest, and that of the chloride is smallest, together with the explanation (Yazdani and Seddigh, 2016).

Table 2.2 Sizes of anions forming the iron precursor salts (Yazdani and Seddigh, 2016).

Anion	Size [pm]
Cl ⁻	167
SO ₄ ²⁻	258
NO ₃ ⁻	179

Mascolo et al. (2013) studied the effect of the base concentration, base species, and addition rate of the base on the synthesized SPIONPs. NaOH, KOH, and (C₂H₅)₄NOH were chosen as bases, and the temperature was set to room temperature. It was found that the sizes of the SPIONPs decreased in the order of NaOH, KOH, and (C₂H₅)₄NOH depending on the bases used. As the size of the cation is in the sequence of Na⁺ < K⁺ < (C₂H₅)₄NOH⁺, this tendency can be explained by the electric double layer thickness. Additionally, the sizes of the SPIONPs decreased most if the addition of the base is fast. If the base is added rapidly, nucleation can consume the particle monomers rapidly, and prevent the particles from growing.

2.2.2.2. Thermal Decomposition Method

One of the popular methods to synthesize SPIONPs is the thermal decomposition method. This method was used for synthesizing II–VI semiconductor clusters. Extending this strategy to oxides, researchers have developed methods to synthesize high-quality metal oxide nanocrystals using the thermal decomposition method (Trentler et al., 1999). With this method, magnetite or maghemite nanoparticles can be easily synthesized through decomposition of organometallic materials in high-boiling solvents containing several surfactants. Several organometallic materials can be utilized, such as iron cupferron, iron acetylacetonate, iron oleate, and iron pentacarbonyl (Park et al., 2004; Rockenberger et al., 1999; S. Sun and Zeng, 2002).

If the iron in the precursor is zerovalent such as in iron pentacarbonyl, the precursor is decomposed to form metal. However, with the addition of a mild oxidant such as trimethylamine oxide at high temperature, maghemite nanoparticles can be synthesized. For precursors with cationic iron centers such as iron cupferron, iron acetylacetonate, or iron oleate, the decomposition leads directly to iron oxides (Lu et al., 2007).

Rockenberger et al. (1999) proposed a method of synthesizing transition metal oxide nanoparticles such as iron oxide, copper oxide, and manganese oxide by thermal decomposition of metal cupferronates $M^x\text{Cup}_x$ (Cup: N-nitrosophenylhydroxylamine $\text{C}_6\text{H}_5\text{N}(\text{NO})\text{O}^-$). For the thermal decomposition, iron cupferronates were heated for 30 min at 225 °C in a solvent of trioctylamine. After cooling to room temperature, the nanoparticles were

extracted from the trioctylamine by adding organic solvents such as toluene, CHCl_3 , etc. They repeated the procedure with copper cupferronates and manganese cupferronates. Consequently, they obtained $\gamma\text{-Fe}_2\text{O}_3$, Mn_3O_4 , and Cu_2O nanoparticles with an average diameter of 6.7 nm and a standard deviation of 1.4 nm. They reduced the sizes of the nanoparticles by lowering the temperature or concentrations of metal cupferronates, and increase the size of the nanoparticles with additional injection of precursor solutions. With their method, each additional injection increased the average size of the nanoparticles by 1 nm. They injected the iron cupferronate solutions up to five times during the decomposition procedure, which led to the production of maghemite nanoparticles with an average size of 10.0 ± 1.5 nm.

Park et al. (2004) synthesized monodispersed iron oxide nanoparticles on an ultra-large scale, namely, 40 g of nanoparticles by thermal decomposition of the nontoxic and inexpensive precursor iron oleates. The iron-oleate complex was synthesized by a reaction between $\text{FeCl}_3 \cdot 6\text{H}_2\text{O}$ and sodium oleate. Then, the iron-oleate complex was heated in 1-octadecene to 320 °C, and was aged for 30 min to grow iron oxide nanoparticles. The synthesized nanoparticles can be easily separated by re-dispersion in organic solvents such as hexane and toluene, with the final yield of the products higher than 95%. Consequently, monodispersed and uniform-sized 12 nm iron oxide nanoparticles were synthesized. Further, the particle size can be controlled using several solvents with different boiling points. The iron oxide nanoparticles with sizes of 5 nm, 9 nm, 12 nm, 16 nm, and 22 nm could be synthesized using 1-hexadecene (b.p. 274 °C), octyl ether (b.p. 287 °C), 1-octadecene (b.p. 317 °C), 1-eicosene (b.p.

330 °C), and trioctylamine (b.p. 365 °C), respectively. The synthesized particle size increased if the boiling point of the solvent increased. This was explained by the fact that the reactivity of a metal-oleate complex is higher in a solvent with a higher boiling point.

Compared with the co-precipitation method, the thermal decomposition method has the advantages of shape and size control, and narrower size distribution. However, the process is more complicated than the co-precipitation method as it requires higher reaction temperature, longer reaction time, and gas injection. Moreover, the product of the thermal decomposition method is usually organic-solvent-soluble, while that of the co-precipitation method is water-soluble.

2.3. Particle Dispersion Theory

To achieve stable dispersion of synthesized nanoparticles, it is important to know the interactions between particles. There is always an attractive interaction between particles because of the van der Waals force. This attractive interaction makes the particle dispersion unstable and causes formation of aggregates. Therefore, to achieve stable dispersion of nanoparticles, there must be a kind of repulsive interaction between the particles that can prevent them from agglomerating. One of the major sources of repulsion is electrostatic attraction. Particle surfaces can be charged in aqueous conditions via ionization of surface groups, ion adsorption onto the surface, ion dissolutions from the particles, and adsorption and orientation of dipoles (Shaw, 1992). If the surfaces

of particles in water are charged, ions of opposite charge are attracted to the surfaces, and form electric double layers around them. If the diffuse parts of electric double layers between two particles overlap, a repulsive interaction arises. This repulsive interaction is electrostatic repulsion between the particles. A quantitative theory that combines these two interactions to simulate the particle dispersion stability is the Deryagin–Landau and Verwey–Overbeek (DLVO) theory, which is one of the most important theories with regard to the colloidal stability. With the theory, the behavior of particles is predicted according to the distance between them.

Polymeric coating of particles is often used to enhance the stability of particle dispersion. Coating the particles with several polymers enhances the surface charge of the particles and prevent agglomeration of the particles by inducing steric hindrance.

If the steric interaction occurs between two particles with polymer coating, two additional factors should be considered besides the van der Waals and electrostatic interactions. First, If the two polymer-coated particles approach each other, overlapping of the polymer brush results in a local increase of monomer concentration in the overlapped region. The increase in concentration causes an increase in local osmotic pressure, allowing the solvent to flow between the particles. Moreover, if the particles approach closer than the length of the polymeric brush, compression of the brushes causes a reduction in entropy, resulting in a rise of entropic elastic repulsion (Fritz et al., 2002).

Developing a fully predictive model for steric repulsion is difficult because the polymeric brush can swell or compress according to the pH or ionic

strength of the solution; however, there have been some attempts to quantify the effect of steric repulsion. Napper et al. (1977) first attempted to treat the steric interaction in quantified form. From their study, the repulsive interaction caused by local osmotic pressure was given as follows:

$$\begin{aligned}
 \frac{E_{OSM}}{k_B T} &= 0 & 2L \leq H \\
 \frac{E_{OSM}}{k_B T} &= \frac{4\pi a}{v_1} \phi_p^2 \left(\frac{1}{2} - \chi\right) \left(L - \frac{H}{2}\right)^2 & L \leq H \leq 2L \quad (9), \\
 \frac{E_{OSM}}{k_B T} &= \frac{4\pi a}{v_1} \phi_p^2 \left(\frac{1}{2} - \chi\right) L^2 \left(\frac{H}{2L} - \frac{1}{4} - \ln\left(\frac{H}{L}\right)\right) & H < L
 \end{aligned}$$

where χ is the Flory–Huggins solvency parameter, ϕ_p is the volume fraction of polymer within the brush layer, L is the thickness of the polymer brush, and v_1 is the volume of a solvent molecule.

The entropic elastic repulsion caused by compression of the polymer brushes in the region of $H < L$ can be expressed as follows:

$$\begin{aligned}
 \frac{E_{VR}}{k_B T} &= 0 & L \leq H \\
 \frac{E_{VR}}{k_B T} &= \left(\frac{2\pi a}{M_W} \phi_p L^2 \rho_p\right) \left(\frac{H}{L} \ln\left(\frac{H}{L} \left(\frac{3(3 - H/L)}{2}\right)^2\right)\right) & (10), \\
 & - 6 \ln\left(\frac{3 - H/L}{2}\right) + 3\left(1 + \frac{H}{L}\right) & H < L
 \end{aligned}$$

where M_W is the molecular weight of the polymer and ρ_p is its density. By

simply adding these terms to the DLVO theory, the steric repulsion can be approximately considered for particle dispersion theory.

Fritz et al. (2002) considered the effects of pH and ionic strength on the steric interaction. In the study, they demonstrated that the pH and ionic strength only affects the polymeric brush length L . They excluded the situation wherein two particles approach closer than the brush length L ; this is because for moderate conditions, such significant brush deformation hardly occurs. As the high-frequency modulus G_{∞}' is linked to interaction potential (Zwanzig and Mountain, 1965), they measured the modulus using torsional resonators to deduce the interparticle potential in several conditions. From the measurements, it was shown that the steric interaction is usually dominated by local osmotic pressure caused by overlapping of brushes, and G_{∞}' can be predicted quantitatively based on a model for osmotic repulsion formed by Vincent et al. (1986).

2.4. Functionalization of Superparamagnetic Iron Oxide Nanoparticles

Functionalization is a procedure for attaching specific functional groups such as carboxyl (-COOH), hydroxyl (-OH), and amine (-NH₂) groups onto the surfaces of nanoparticles. This procedure is widely used to enhance properties of the nanoparticles such as dispersion stability, drug-carrying ability, adsorption capacity, and biocompatibility. In particular, improving the

dispersion stability is important because aggregation renders the nanoparticles to form larger clusters, disabling their useful properties such as small size and large specific surface area.

A wide variety of nanoparticle functionalization methods have been developed and published. These methods are largely divided into functionalization using organic materials such as surfactants, silanes, and polymers; and functionalization using inorganic materials. In this section, some nanoparticle functionalization methods are briefly introduced.

2.4.1. Functionalization by Small Organic Molecules

Small organic molecules have been widely used for the functionalization of SPIONPs. Small surfactant molecules can adsorb onto the SPIONP surfaces by several interactions including the van der Waals interaction, electrostatic interaction, and chemical bonding. Most simply, small organic molecules have been applied to increase the solubility of nanoparticles in several solvents.

Oleic acid ($\text{CH}_3(\text{CH}_2)_7\text{CH}=\text{CH}(\text{CH}_2)_7\text{COOH}$) is commonly used to enhance the solubility of SPIONPs in organic solvents. If oleic acid is introduced to the SPIONP surface, the carboxylic groups in the oleic acid can bind to the nanoparticle surfaces by acid–base reaction with Fe–OH groups on the surface (Harris et al., 2003; Yu and Chow, 2004). Subsequently, the hydrocarbon chain of the oleic acid stabilizes the SPIONPs in organic solvents. However, stearic acid ($\text{CH}_3(\text{CH}_2)_{17}\text{COOH}$) does not have a kink structure that is caused by a double bond existing in oleic acid; therefore, it may not improve

the dispersion stability of SPIONPs in organic solvents. To explain this, Tadmor et al. measured the force between layers of oleic-like surfactants and layers of stearic-like surfactants using a surface force balance. Based on these measurements, they observed that the layers of oleic-like surfactants are solvated and fully wetted in a hexadecane medium, while layers of stearic-like surfactants are not (Tadmor et al., 2000). Numerous other surfactant molecules, including lauric acid, dodecyl phosphate, hexadecyl phosphonate, and dihexadecyl phosphate were found to be effective for stabilizing SPIONP dispersion in organic solvents (Wu et al., 2008).

In addition, there have been many attempts to enhance the solubility of SPIONPs in aqueous solvents. For this purpose, citric acid is widely used. Citric acid contains three carboxylic acid groups in its molecules that can bind strongly onto metal oxide surfaces by acid–base reaction; further, these can induce a strong negative charge onto the surfaces by ionizing in water. The strong negative charge induced by citric acid can stabilize the dispersion of SPIONPs in water by improving the electrostatic repulsion between the particles. The use of citric acid is favorable because citric acid is non-toxic and biocompatible (Răcuciu et al., 2006).

Use of silane coupling agents is other options for functionalizing the SPIONPs. The general formula of a silane coupling agent is $Y-(CH_2)_m-Si-(OR)_3$. Y represents the organic functional groups that are needed for the functionalization of nanoparticles. By hydrolysis, the $-Si-(OR)_3$ group in the molecule is activated to a $Si-(OH)_3$ group, releasing alcohol (ROH). Then, the hydrolyzed silane groups can bind to metallic oxides or silicon oxides (Lung

and Matinlinna, 2012). After the silane treatment, the SPIONPs maintain their physical properties, only losing the saturation magnetization of less than 10 emu/g. Next, 3-aminopropyltriethoxysilane (APTES), 3-aminopropyltrimethoxysilane (APTMS), and p-aminophenyltrimethoxysilane (APMS) are employed to functionalize particle surfaces with amine groups; (3-mercaptopropyl) triethoxysilane (MPTES) is employed to add sulfhydryl groups onto the surfaces (Ko et al., 2016; Wu et al., 2008); and recently (3-glycidyloxypropyl) trimethoxysilane (GPTMS) has often been employed (del Hierro et al., 2018). In general, silane agents that contain ethoxysilane or methoxysilane are used for silanization. However, ethoxysilane is favorable because methoxysilane releases toxic methanol during the hydrolysis process, whereas ethoxysilane releases ethanol that is less toxic.

Often, silanization of nanoparticles is followed by functionalization with other molecules or surfactants. If a particle is functionalized with aminosilanes like APTES and APTMS, the amine groups on the particle surfaces can react with carboxylic acid groups in the other molecules, forming amide bonds. Therefore, it is possible to anchor organic molecules to the nanoparticle surfaces by strong chemical bonds. Therefore, studies on silanization using GPTMS have been increasing in number recently. Epoxide rings in GPTMS can form bonds with several functional groups in other molecules or polymers by ring-opening reactions, allowing several molecules to anchor to the nanoparticle surfaces via covalent bonding.

2.4.2. Functionalization by Polymers

Research on polymer functionalization of nanoparticles has been increasing rapidly in recent years. Polymer functionalization can increase the stability of nanoparticle dispersion by electrostatic repulsion induced by functional groups added in polymers, and by steric repulsion induced by an increased monomer concentration in polymers. In addition, polymer functionalization can impart unique physical and chemical properties to the nanoparticles. Many researchers have studied the effects of polymer functionalization of SPIONPs using polyethylene glycol (PEG), polyacrylic acid (PAA), poly(D,L-lactide) (PLA), polystyrene (PS), polymethylmethacrylate (PMAA), etc. (Chatterjee et al., 2001; Flesch et al., 2005; Gass et al., 2006; Gómez-Lopera et al., 2001; Viota et al., 2008).

As mentioned previously, polymeric functionalization significantly enhances the stability of nanoparticle dispersion. If treated with polymers with anionic functional groups such as PAA, a strong negative charge induced by the polymers enhances the electrostatic repulsion between the particles, increasing the dispersion stability (Piñeiro-Redondo et al., 2011; Viota et al., 2008). Polymers with cationic functional groups, such as polyethylene imine, enhance the dispersion stability (Solodov et al., 2018).

Researchers from the University of Texas at Austin (Bagaria, Xue, et al., 2013) achieved stable dispersion of SPIONPs in the presence of NaCl and CaCl₂ salts. They synthesized copolymers of acrylic acid and 2-acrylamido-2-methyl-1-propanesulfonic acid (poly(AA-co-AMPS)), and treated SPIONPs

with the polymers. If the poly(AA-co-AMPS) is introduced into the SPIONP dispersion, the carboxylic acid groups in acrylic acid monomers anchor to the SPIONPs, while the sulfonate groups in AMPS monomers induce significant negative charging of the particle surface. Therefore, a stable dispersion of SPIONPs under high salinity could be achieved.

As mentioned previously, a silanization process often precedes polymer functionalization to enhance the bonds between polymer and nanoparticle surfaces. The silanization can be conducted at the nanoparticle surface to functionalize nanoparticle surface groups that can form chemical bonds with polymers, and sometimes the polymer is silanized to generate silane groups that can strongly bind to the nanoparticle surfaces. Aminosilanes such as APTES and APTMS were employed to enhance the bonds between carboxylic groups containing polymers such as PAA and its copolymers by amide bonding (Feng et al., 2008; Mahdavian and Mirrahimi, 2010). GPTMS, which contains highly reactive epoxide rings, was employed to form a link between the several polymers and the SPIONPs (Tsai et al., 2013).

In the general polymer functionalization process, a readily synthesized polymer is attached to the SPIONP surfaces. However, Dresco et al. (1999) developed a method of synthesizing polymer-functionalized SPIONPs by synthesizing polymers in the presence of SPIONPs. They achieved the process by synthesizing SPIONPs and polymers in single inverse microemulsion. In the study, SPIONPs were first synthesized in AOT–toluene inverse microemulsion. Then, the monomers (9:1 ratio of methacrylic acid and hydroxyethyl methacrylate), crosslinker (N,N'-methylenebis(acrylamide)), and an initiator

(2,2'-azobis(isobutyronitrile) or potassium persulfate) was added to the SPIONPs in microemulsion. After a polymerization process at 55 °C, they could achieve polymer-coated SPIONPs with narrow size distribution at a size of about 80 nm.

Other methods of synthesizing polymer-functionalized SPIONPs is by grafting SPIONPs with polymer chains. If initiators for atom transfer radical polymerization (ATRP) are anchored to SPIONPs, polymer chains can be grafted from the SPIONP surfaces. Babu and Dhamodharan (2008, 2009) synthesized 2-bromo-2-methyl-propionic acid 2-phosphonooxy-ethyl ester as an initiator for an ATRP process, then attached the initiator to the SPIONPs. The initiator could attach to the SPIONPs by acid–base reaction between the particle surface groups and phosphonate group in the initiator. Then, the polymerization process was conducted by mixing CuBr, initiator-attached SPIONPs, methyl methacrylate monomers, and pentamethyldiethyltriamine. Consequently, stable dispersion of polymer-functionalized SPIONPs in tetrahydrofuran solvent was obtained.

2.4.3. Functionalization by Inorganic Materials

Inorganic materials are often employed to functionalize SPIONPs because they have some advantages over organic materials. One of the advantages is that they can enhance the antioxidation properties of SPIONPs that are highly oxidizing under ambient conditions. In addition, they can maintain relative stability at high temperatures that organic materials decompose, and their

unique physical and chemical properties is applicable to fields such as catalysts and biolabeling.

A common inorganic material used to functionalize SPIONPs is silica. Silica coating provides stability to the SPIONP core, and enhances hydrophilicity, biocompatibility, and dispersion stability (Wu et al., 2008). It prevents unwanted interactions that can be caused by direct contact between other materials and the iron oxide cores. Additionally, most research on the surface treatment of nanoparticles is conducted based on silica nanoparticles, and thus, the results of these studies can be applied to SPIONPs by coating the SPIONPs with silica.

Generally, the Stöber method and sol–gel process are chosen for the silica coating of SPIONPs. By hydrolyzing tetraethoxysilane (TEOS) in the SPIONP dispersion, silica-coated SPIONPs can be synthesized. For more controlled synthesis, the synthesis procedure is often conducted in microemulsions that can be a microreactor for the process to improve the uniformity of the silica coating thickness (Philipse et al., 1994; Stöber et al., 1968; Tago et al., 2002). The silica layer thickness can be controlled between 5 and 200 nm by changing the concentration of ammonia and the ratio of TEOS to water.

Metal functionalization with gold, silver, platinum, palladium, etc. can provide a protective layer to the SPIONPs. Gold is the most common noble metal for surface coating because the gold layer is chemically inert and can provide good antioxidizing properties to the SPIONPs. The gold coating of SPIONPs can be achieved by direct and indirect methods (Moraes Silva et al., 2016). In the direct method, a gold shell is formed by reduction of Au^{3+} ions by

reducing agents. The most popular method employs gold chloride (HAuCl_4) as a gold ion source and sodium citrate as a reducing agent. In this method, SPIONPs are introduced to the hot gold chloride solution, and then sodium citrate solution is added to the mixture with vigorous stirring. Consequently, a thin gold layer is coated on the SPIONPs. Sodium citrate can provide the citrate coating to the nanoparticles that can enhance their dispersion stability (Lo et al., 2007). This method has the advantage of being able to coat the SPIONPs with gold relatively simply. However, SPIONP/gold ratio and concentration should be carefully selected to achieve proper gold coating of iron oxide nanoparticle without forming separated gold nanoparticles.

The main characteristic of indirect gold coating is the existence “glue layer” between the SPIONP surface and the gold coating (Moraes Silva et al., 2016). The design and preparation of the glue layer should be given consideration because the glue layer should coat SPIONPs sufficiently to provide them with chemical and physical stability, and contain lots of metal binding groups that can chelate gold ions and facilitate the gold coating (Hu et al., 2013). For the glue layer, polymer materials like poly-L-histidine, poly(cyclotriphos-phazene-co-4,40-sulfonyldi-phenol) (PZS), polyethylene imine, etc. are employed (Chuah et al., 2012; Hu et al., 2013; Jin et al., 2010; Lai et al., 2011). The gold-coated SPIONPs can be applied in fields such as biosensors, hyperthermia, nanoelectrodes, etc. (Chauhan, Narang et al., 2012; Kim et al., 2006; Lai et al., 2011).

Metallic-material-coated SPIONPs can be used as catalysts. With the catalytic behavior that the metallic shell provides and the magnetic behavior

that the iron oxide core imparts, the catalysts can be easily recovered from a reactor by magnetic separation. In addition, the efficiency of the catalysts increases due to their increased specific surface area. Metallic catalysts, such as Au for CO oxidation, Pd for the decarboxylate coupling reaction, and Ag for styrene epoxidation, have been studied by many researchers as functionalizing materials for SPIONPs (Al-Sayari et al., 2007; Yeo et al., 2007; Zhang et al., 2008).

Chapter 3. Materials and Methods

To employ SPIONPs in the oil field industry, there are some criteria required for the nanoparticles. One of the biggest criterion is that, the SPIONPs should be stable enough to endure the high salinity of the underground water that can cause the particles to aggregate by decreasing the electric double-layer forces between them (Adamson and Gast, 1997; Shaw, 1992). It is reported that the rock pores in conventional sandstones in oil reservoirs are in the range of 0.2 μm to 0.5 mm in diameter for tubular openings (Hu, 2017). If the nanoparticles are agglomerated and become larger than the pore size, they cannot pass through the small pores. Therefore, it is necessary to maintain the dispersion of nanoparticles in the harsh conditions of underground reservoirs. In this study, steelworks by-products were chosen as an ingredient for SPIONP synthesis, and sulfonated phenolic resins were chosen as a surface modifier of the particles.

Steelworks byproducts are cheap and iron-rich ingredients that can be used for SPIONP synthesis. From the ingredients, the SPIONPs will be synthesized by co-precipitation method. For petroleum reservoir imaging, the purity and polydispersity of the SPIONPs are not important factors. Therefore, the choice of ingredients and synthetic method is feasible.

Sulfonated phenolic resins can be simply synthesized by mixing two cheap chemicals and heating them, and can impart a strong negative charge onto the surface of SPIONPs; this causes them to stay dispersed under high-salinity

conditions. With the ingredients for the SPIONP synthesis and functionalization, the cost of synthesis can be reduced.

In this chapter, a detailed method of synthesis of SPIONPs from steelworks byproducts is presented. Then, the SPIONPs are functionalized with widely used polymers like PEG, polyvinyl alcohol (PVA), and PAA as a comparison. After this, a functionalization method of SPIONPs based on sulfonated phenolic resin will be studied. Additionally, an analysis method for the synthesized SPIONPs will be presented.

3.1. Synthesis of Superparamagnetic Iron Oxide Nanoparticles from Steelworks Byproducts

In the steel-making process, the surface of the steel is oxidized due to its initial high temperature. To remove the iron oxide from the steel surface, an acid solution is usually employed. This process is called the pickling process. As a byproduct of the pickling process, a highly pure iron ion solution is produced.

This can be used as a cheap ingredient for synthesizing SPIONPs. In this section, the process of making SPIONPs from steelworks by-products by co-precipitation is presented. Using a conventional and simple co-precipitation method, inexpensive mass production of SPIONPs is possible.

Steelworks byproducts samples with high purity of Iron(III) oxide (Fe_2O_3) were taken from POSCO (South Korea) (Figure 3.1 (a)). Hydrochloric acid

(HCl; 35 wt%), sodium hydroxide (NaOH; 97 wt%), and sodium borohydride (NaBH₄; 97 wt%) were obtained from Daejung Chemicals and Metals Co., Ltd. (South Korea). All the chemicals were used as received without further purification.

First, 10 g sample of steelworks byproducts was added to 200 ml 1M HCl solution, and then the mixture was heated to 80 °C and maintained for 1 h. The mixture was then cooled to room temperature and centrifuged at 3000 rpm for 30 min to remove undissolved particles. Consequently, highly pure iron(III) ion solution could be obtained (Figure 3.1b).

One-third of the iron(III) ion solution was reduced with 3M sodium borohydride solution to produce iron(II) solution. Under constant stirring, the sodium borohydride solution was added to the iron(III) ion solution. The addition was stopped if iron started to precipitate and then the solution was kept stirred until the iron precipitant dissolved again. Consequently, a green-colored iron(II) ion solution was formed (Figure 3.1c).

The initial iron(III) ion solution and the iron(II) ion solution were mixed and heated to 80 °C. Then, 200 ml of 2M NaOH solution was added to the solution. Consequently, a black precipitant was formed, and the solution was continuously stirred for another 1 h for further reaction. The precipitant was magnetically settled using a neodymium magnet, and then washed three times with deionized water (Figure 3.1d).

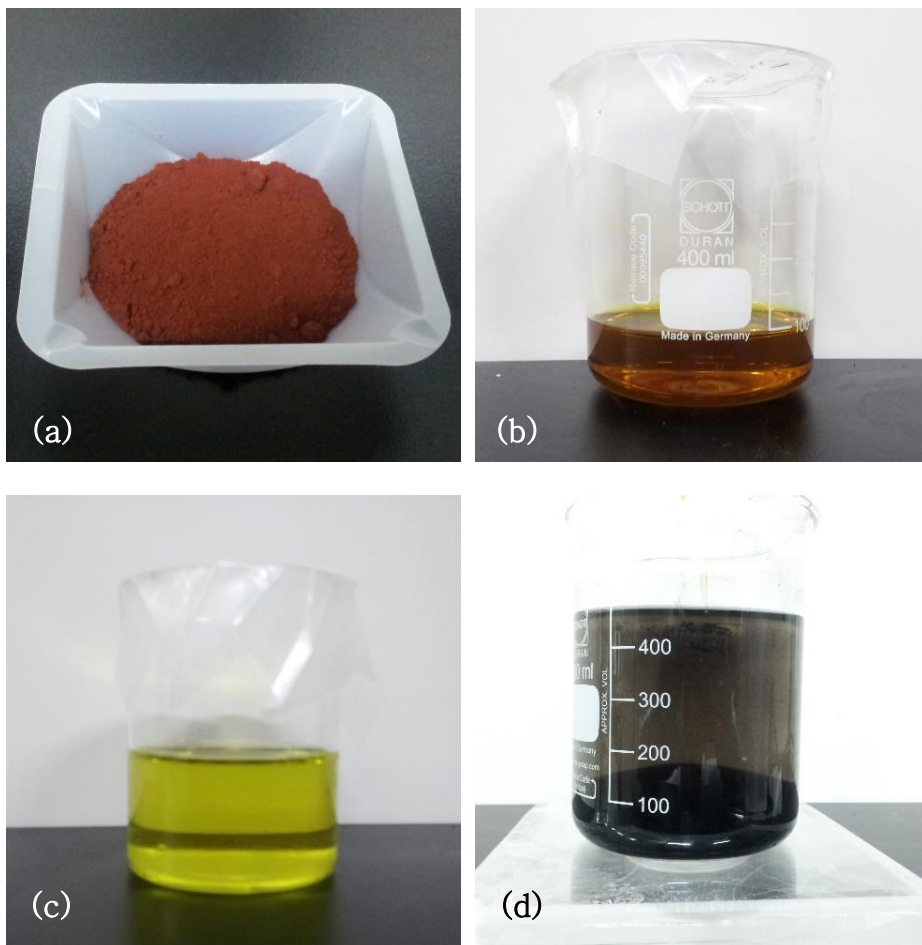
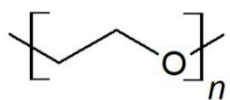


Figure 3.1 Synthetic process of the superparamagnetic iron oxide nanoparticles: (a) iron oxide steelworks byproduct samples; (b) Fe^{3+} solution leached from (a); (c) Fe^{2+} solution reduced from (b); and (d) final synthesized superparamagnetic iron oxide nanoparticles separated from the solution by magnetic separation.

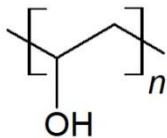
3.2. Functionalization of Superparamagnetic Iron Oxide Nanoparticles with Several Polymers

For the functionalization of nanoparticles, several polymers such as PEG, PVA, and PAA have been widely used (Lu et al., 2007; Wu et al., 2008). In Figure 3.2, the molecular structures of the polymers are shown. These polymers can be attached to the SPIONPs by electrostatic interactions, van der Waals interactions, and covalent bonding between a functional group in a polymer and a surface group of SPIONPs. By functionalizing the SPIONPs with these polymers, the dispersion stability of the SPIONPs in water is enhanced owing to the electrostatic and steric repulsion induced by the polymer molecules. In this section, SPIONPs are functionalized with these polymers, and the dispersion stability of the functionalized nanoparticles in brine is examined.

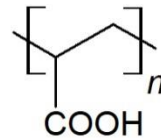
Iron(II) chloride tetrahydrate ($\text{FeCl}_2 \cdot 4\text{H}_2\text{O}$; 99 wt%), iron(III) chloride hexahydrate ($\text{FeCl}_3 \cdot 6\text{H}_2\text{O}$; 99 wt%), sodium hydroxide (NaOH; 97 wt%), and hydrochloric acid (HCl; 35 wt% solution) were obtained from Daejung Chemicals & Metals Co., Ltd. (South Korea). All the polymers used for the experiments were purchased from Daejung Chemicals & Metals Co., Ltd.



PEG



PVA



PAA

Figure 3.2 The molecular structure of polyethylene glycol (PEG), polyvinyl alcohol (PVA), and polyacrylic acid (PAA).

First, bare SPIONPs were synthesized by a conventional co-precipitation method from iron chloride salts (Yoon et al., 2016). The steelworks byproduct from the pickling process is highly pure iron(III) oxide and the solution that is produced by reaction between the steelworks byproduct and hydrogen chloride is almost same with the iron(III) chloride solution. Therefore, the SPIONPs were synthesized using iron chloride salts from this section to speed up the process.

Initially, 1.0 g of iron(II) chloride tetrahydrate and 2.7 g of iron(III) chloride hexahydrate were dissolved in 100mL of deionized water. The solution was heated to 80 °C, and then 100 mL of 1M NaOH solution was added to the solution. The resulting black precipitant was settled using a neodymium magnet, washed with 100 mL deionized water three times, and dispersed in 100 mL deionized water.

The synthesized SPIONPs were functionalized with several polymers via the following procedure. First, 0.12 g of SPIONPs (5 ml of SPIONP dispersion) was dispersed in 100 mL deionized water. Then, 1 g of each polymer, PEG (MW 9,000 g/mol), PVA (MW 22,000 g/mol), and PAA (MW 8,000~12,000 g/mol), was added to the dispersion. The dispersion was sonicated by a probe-type ultrasonic generator (VCX 500 from Sonics & Materials Inc.) for 1 h. To remove any unreacted polymer, the dispersion was centrifuged at 28,000 rpm for 1 h. The precipitation was then re-dispersed in 50 mL of deionized water by sonication and centrifuged for another 1 h. This procedure was repeated three times, before the final products were dispersed in 100 mL deionized water.

3.3. Functionalization of Superparamagnetic Iron Oxide Nanoparticles with Sulfonated Phenolic Resin

To enhance the stability of the iron oxide nanoparticles dispersion in harsh underground conditions of high salinity and temperature, functionalization of the SPIONPs with specific polymers is necessary. For example, researchers at the University of Texas at Austin produced a stable dispersion of SPIONPs in API brine (NaCl 8 wt% + CaCl₂ 2 wt% solution) by functionalizing them with poly(AMPS-co-AA), a copolymer of 2-acrylamido-2-methyl-1-propanesulfonic acid and acrylic acid. If SPIONPs are functionalized with poly(AMPS-co-AA), the rich sulfonate groups in the polymer induce a strong negative charge onto the nanoparticles that can stabilize the nanoparticle dispersions (Bagaria, Neilson, et al., 2013; Bagaria, Xue, et al., 2013; Bagaria, Yoon, et al., 2013).

However, such a polymer may not be economically viable owing to the cost of the chemical species and the difficulty of the synthesis process. Because a large number of nanoparticles is needed for injection into underground oil reservoirs because of their scale, a cheaper and simpler process of nanoparticle synthesis is mandatory. In this section, sulfonated phenolic resin (SPR) is suggested as an alternative.

SPR can be easily synthesized from the condensation polymerization process between 4-hydroxy benzene sulfonic acid and formaldehyde (Figure 3.3), and contains high density of sulfonate groups (Guthrie and Sada, 1982).

The sulfonate groups in the polymer can make a bond between Fe atoms in SPIONPs by acid–base reactions (Figure 3.4) (Yee et al., 1999), and can induce strong negative charge onto the SPIONP surfaces in aqueous conditions. Moreover, its aromatic-ring-based structure remains stable in high-temperature conditions because of the high strength of its primary bonds (O dian, 2004). In this section, SPIONPs are functionalized with SPR by co-precipitation of the particles in the presence of the polymer.

Iron(II) chloride tetrahydrate ($\text{FeCl}_2 \cdot 4\text{H}_2\text{O}$; 99 wt%), iron(III) chloride hexahydrate ($\text{FeCl}_3 \cdot 6\text{H}_2\text{O}$; 99 wt%), sodium hydroxide (NaOH; 97 wt%), formaldehyde (HCHO; 98 wt%), calcium oxide ($\text{Ca}(\text{OH})_2$; 99 wt%), and hydrochloric acid (HCl; 35 wt% solution) were obtained from Daejung Chemicals & Metals Co., Ltd. (Korea). The 4-hydroxy benzene sulfonic acid ($\text{C}_6\text{H}_5\text{SO}_3\text{H}$; 65 wt% solution) was purchased from Sigma-Aldrich. All the chemicals were used as received without further purification.

SPR was synthesized by condensation polymerization between 4-hydroxy benzene sulfonic acid and formaldehyde. Further, 30 mL of a 65 wt% 4-hydroxy benzene sulfonic acid solution and 12 mL of a 35 wt% formaldehyde solution were mixed, and the volume of the total solution was set to 100 mL by adding deionized water. After setting the pH of the solution to 2 by adding 3M $\text{Ca}(\text{OH})_2$, the solution was reacted at 100 °C for 18 h. The solution was cooled to room temperature, and then by adding 3M $\text{Ca}(\text{OH})_2$, the pH of the solution was adjusted to 7. The solution was centrifuged at 3000 rpm for 30 min and filtered with a 0.45 μm filter to remove the precipitate. The final solution volume was adjusted to 100 mL by adding deionized water.

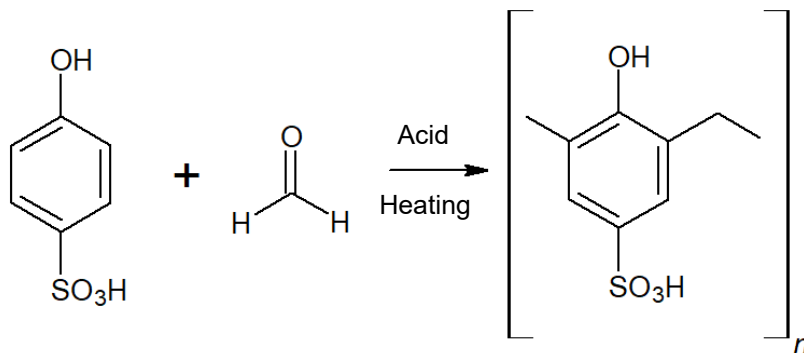


Figure 3.3 Synthesis procedure of sulfonated phenolic resin by condensation polymerization between 4-hydroxy benzenesulfonic acid and formaldehyde.

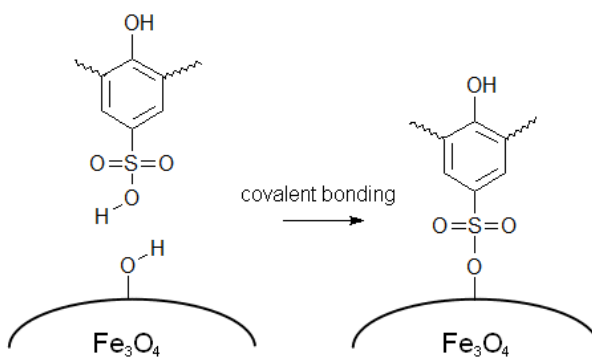


Figure 3.4. Acid–base reaction between sulfonated phenolic resin and an iron oxide nanoparticle surface.

Functionalization of SPIONPs with SPR was conducted by in-situ co-precipitation of SPIONPs in SPR solution. Quantities of 1.0 g of iron(II) chloride tetrahydrate, 2.7 g of Iron(III) chloride hexahydrate, and 40 mL of SPR solution were added to deionized water to obtain a final volume of 100 mL. The solution was heated to 80 °C, before 10 mL of 5M NaOH solution was added to the solution. After 10 min of nucleation, the temperature of the solution was increased to 90 °C and maintained for 1 h for further reaction between the SPR and the nanoparticles. After cooling to room temperature, the colloid was centrifuged at 28,000 rpm for 1 h to remove unreacted chemical species. The precipitation was re-dispersed in 50 mL of deionized water by tip sonication and centrifuged for another 1 h. This purification procedure was repeated three times, before the final product volume was set to 100 mL by adding deionized water. The final product was a well-dispersed black dispersion (Park et al., 2019).

3.4. Functionalization of Superparamagnetic Iron Oxide Nanoparticles with Crosslinked Shell of SPR and PVA

The results of the SPR-treated SPIONPs (SPR-SPIONP) showed that the bond between SPR and an SPIONP became unstable under acidic conditions. As the pH of oil field reservoirs varies in a range of 4 to 9 (Wan, 2011), it is important to ensure a stable core-shell structure of SPR-SPIONPs in acidic conditions, neutral and basic conditions.

A method to enhance the stability of the shell structure of nanoparticles or micelles is the crosslinking method (Neamtu et al., 2017; Thurmond et al., 1999). By crosslinking more than two kinds of polymers or surfactants with their functional groups, the stability of core-shell structures can be improved. Yoon et al. (2011) reported that in an iron-oxide-core-polymer-shell nanostructure, the stability of polymer shell was improved by crosslinking the polymers with other crosslinking agents. This idea can be applied to an SPR shell because sulfonate groups in polymers can react with several types of functional groups in other polymers to form crosslinking structures (Mantione et al., 2017; Wu et al., 2006). In this section, a crosslinking method using PVA to enhance the stability of SPR shells is presented.

PVA (22,000 g/mol) was purchased from Daejung Chemicals & Metals Co., Ltd. SPR-SPIONPs were synthesized as described in Section 3.3. After this, 5 ml of synthesized SPR-SPIONP dispersion was diluted to 100 ml with deionized water. Before the mixture was heated for 1 h at 100 °C, 1 g of PVA was added. After cooling to room temperature, the mixture was then centrifuged at 20,000 rpm for 1 h. The precipitation was re-dispersed in 50 mL of deionized water by tip sonication and centrifuged for another 1 h. This procedure was repeated three times, but in the final step, the precipitation was dispersed in 100 mL of deionized water.

3.5. Analysis of Physical and Chemical Properties of Synthesized Nanoparticles

To analyse and evaluate the physical and chemical properties of synthesized nanoparticles, several analysis were conducted.

A colloidal stability test for each nanoparticle dispersion was conducted under the presence of salinity. Each dispersion was set to contain around 0.5 wt% of particle concentration by adding deionized water. The pH was then adjusted using 1M NaOH and 1M HCl solutions. Several amounts of NaCl were added to the colloid, and the stability was then evaluated by visual confirmation of particle sedimentation and change of dispersion color over one week.

The hydrodynamic size of the particles and their zeta potential were measured by a dynamic laser scattering (DLS) method with a Zetasizer NANO-ZS90 (from Malvern Instruments). For the size measurements, each dispersion was set to contain a similar solid concentration by adding deionized water. The colloids were then sonicated with a tip-type ultrasonic generator for 10 min before conducting the size measurements. Then, the sample was loaded into a disposable polystyrene cuvette cell (DTS0012 from Malvern Instruments). The measurement angle was set to 90°, and five measurements for each sample were conducted at room temperature to calculate the average size of the sample.

The zeta potential of each synthesized particle was measured with the same apparatus as the size measurements. Before each measurement, the pH of the sample was adjusted with HCl (1M) and NaOH (1M) solutions. The sample

at each pH was loaded into a disposable folded capillary zeta cell (DTS1070 from Malvern Instruments) by syringe, before the five measurements were performed at room temperature.

To examine the morphology of the particles, transmission electron microscopy (TEM) and scanning TEM energy-dispersive X-ray spectroscopy (STEM-EDS) analyses were conducted.

For sample preparation, a carbon-coated 200 mesh copper grid was used. Some samples were prepared using a holey carbon grid for a better observation of organic materials and a better performance of the EDS analysis. The carbon copper grids were placed on filter paper, and a few droplets of the sample dispersion were dropped onto the grids. The grids were then dried in a 65 °C vacuum oven to prevent the oxidation of the samples.

Each sample was then analyzed with analytical TEM equipment (Tecnai F20 from FEI) to observe its morphology at an operation voltage of 200 kV. Additionally, the distribution of the elements in the sample was studied by EDS analysis using apparatus from EDAX.

Thermogravimetric analysis was conducted to measure the organic content in the synthesized nanoparticles and to evaluate its thermal stability indirectly.

A particle sample of about 1 g was loaded into a TGA 701 instrument from LECO Corp., and was heated from room temperature at a heating rate of 10 °C/min under a nitrogen atmosphere. During heating, the weight loss of the sample was measured. At 107 °C, the temperature of the sample was maintained until mass reduction of the sample no longer occurred, and the mass reduction up to this step was considered as the moisture content of the sample. After this,

the sample was covered with the lid, then heated to 800 °C at the same heating rate. The temperature of the sample was maintained at 800 °C until the mass of the sample stabilized for at least 30 min.

Assuming there is no weight change in the iron oxide core, the weight loss can be considered as loss of organic materials, except for the amount lost due to moisture content.

The magnetization property of each sample was analyzed by a vibrating sample magnetometer (VSM). The nanoparticle colloid was dried in a vacuum oven at 80 °C for more than two days. After drying, approximately 30 mg of the dried particle was loaded into a VSM (PPMS from Quantum Design). A magnetic field was applied to the sample from -30,000 Oe to +30,000 Oe, and the magnetic moment of the sample was measured at 300 K. The mass magnetization of the sample could then be calculated by dividing the magnetic moment by the mass of the sample. From the applied magnetic field and mass magnetization, the M–H hysteresis curve (Langevine curve) of the sample could be obtained (Guimarães, 2009). From the curve, magnetic characteristics of the sample such as saturation magnetization and superparamagnetism were analyzed.

Chapter 4. Results and Discussion

4.1. Synthesis of Superparamagnetic Iron Oxide Nanoparticles from Steelworks Byproducts

Before the synthesis of superparamagnetic iron oxide nanoparticles, the XRD analysis of the steelworks byproducts sample was conducted to identify the composition of the samples. The XRD spectra and the composition analyzed from the spectra is shown in Figure 4.1 and Table 4.1. Figure 4.1 shows the comparison of two spectra, steelworks byproducts and hematite (Fe_2O_3), and it can be seen that the both spectra are almost identical. In Table 4.1, it can be seen that the steelworks byproducts samples are highly pure hematite whose purity is approximately 99%. Although other impurities have concentrations below than 0.5%, it can be assumed that there is no effect that is caused by impurities in the steelworks byproducts sample.

Table 4.1 A composition of the steelworks byproducts analyzed from XRF spectra.

Formula	Fe_2O_3	Cl	P_2O_5	MnO	CaO	CuO	Cr_2O_3
Concentration	98.9	0.422	0.309	0.217	0.0776	0.0359	0.0343

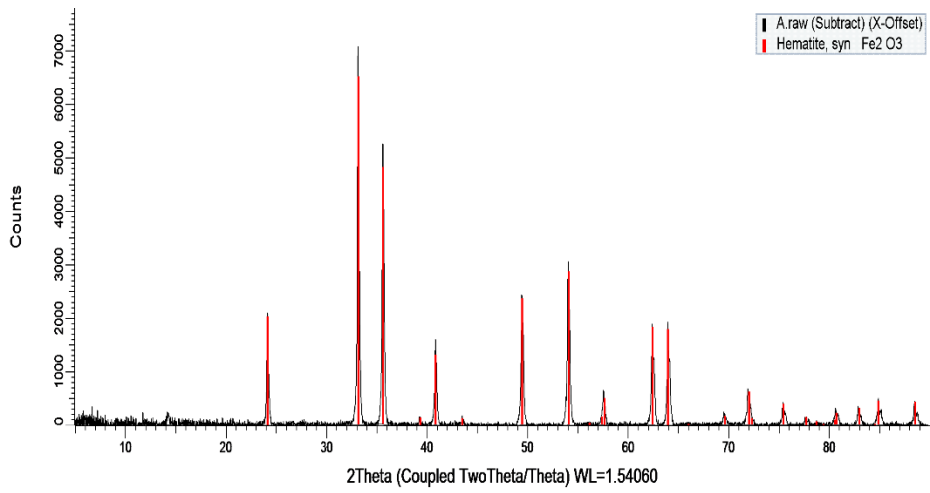


Figure 4.1 XRD spectra of the steelworks byproducts sample used for the experiments.

The physical properties of SPIONPs synthesized from steelworks byproducts were characterized to evaluate the quality of the SPIONPs. First, the pH–zeta curve of the SPIONPs was measured (Figure 4.2). The point of zero charge of the synthesized SPIONPs was found to be around 6 that is similar to the reported value of typical magnetite nanoparticles (Ucbas et al., 2014).

To check the morphology of the particles (e.g., primary particle size), TEM analysis was conducted. Figure 4.3 shows the TEM image of the samples, and Figure 4.4 shows the primary particle size distribution of the sample that is counted from the TEM images. To obtain the size distribution, diameters of at least 150 particles were measured by analysis of TEM images. As can be shown in Figure 4.3 and Figure 4.4, the primary particles, are less than 12 nm in diameter, form larger clusters. Also, the average primary particle size was calculated to 8.6 nm, and the standard deviation of the distribution is calculated to 3.1. It is significant that the sizes of the primary particles are less than 25 nm, because only SPIONPs this small can have superparamagnetic character (Guimarães, 2009).

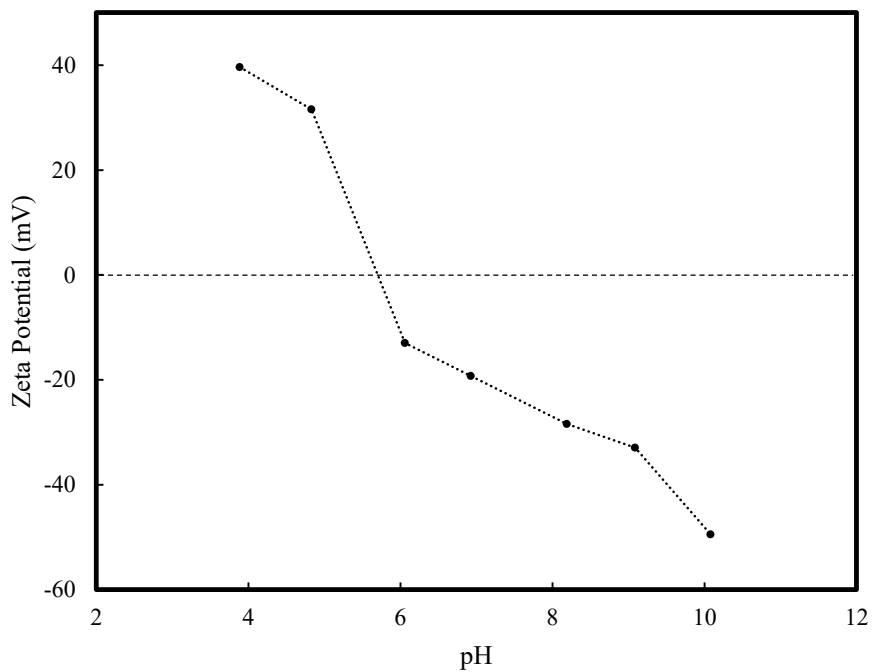


Figure 4.2 Zeta potential vs. pH curve of bare superparamagnetic iron oxide synthesized from steelworks byproducts.

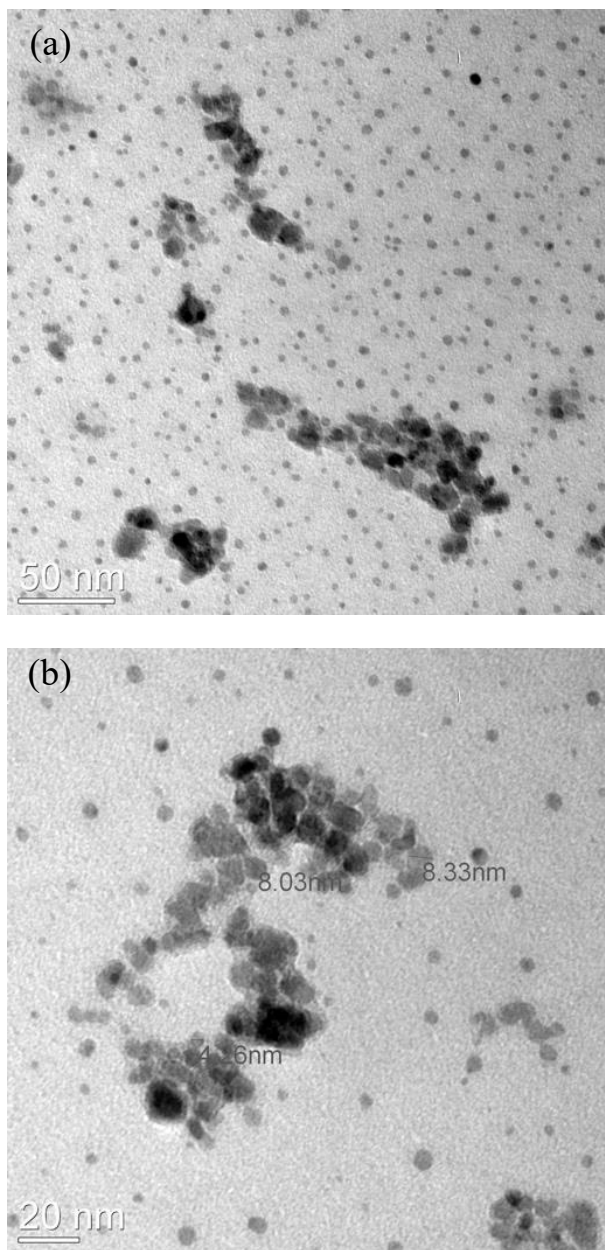


Figure 4.3 (a) TEM image of superparamagnetic iron oxide nanoparticles synthesized from steelworks byproducts. (b) The same particles at higher magnitude. Diameters of some primary particles were measured.

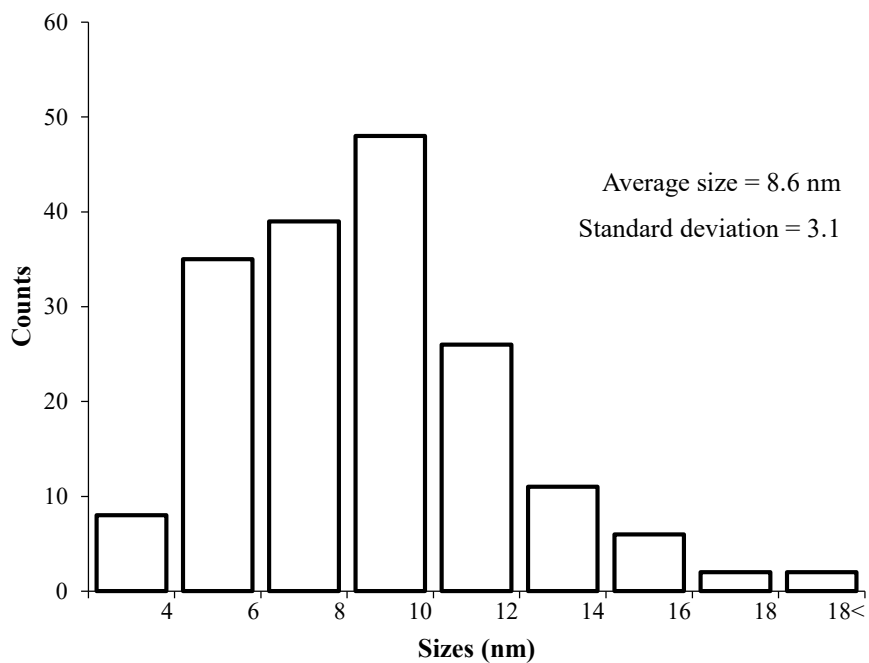


Figure 4.4 Primary particle distribution of the SPIONs synthesized from steelworks byproducts.

The XRD spectra of the magnetite nanoparticles were obtained with Smart Lab from Rigaku, using Mo as a X-ray source (Figure 4.5). From the XRD pattern, typical peaks for the magnetite could be observed as indicated with red lines. However, the peaks of magnetite nanoparticles were broader than bulk magnetite because nanoparticles usually have smaller and poor crystalline structures than bulk materials (Klekotka et al., 2020; Ruíz-Baltazar et al., 2015; Songvorawit et al., 2011).

The Langevine curve of the sample was obtained by VSM analysis (Figure 4.6). It can be seen that the SPIONPs have extremely small magnetization hysteresis and coercivity. It can be said that the SPIONPs have superparamagnetism. It can be seen that the saturation magnetization of the sample is around 50–55 emu/g. This value is very close to that of typical magnetite nanoparticles, with similar primary particle sizes (Mascolo et al., 2013).

From the physical properties analyzed as discussed above, it is clear that good-quality SPIONPs can be synthesized from the low-cost steelworks byproducts.

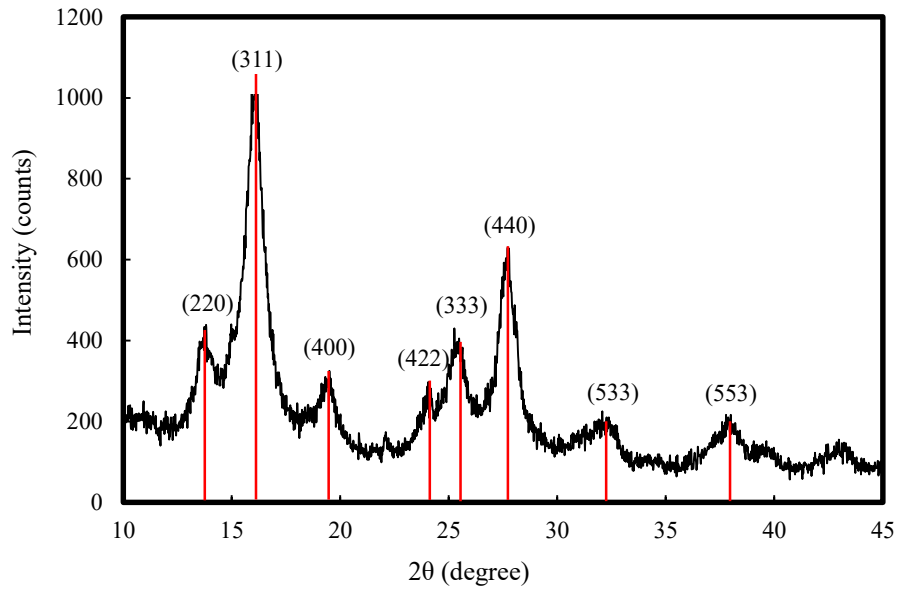


Figure 4.5 XRD spectra of the magnetite nanoparticles synthesized from steelworks byproducts.

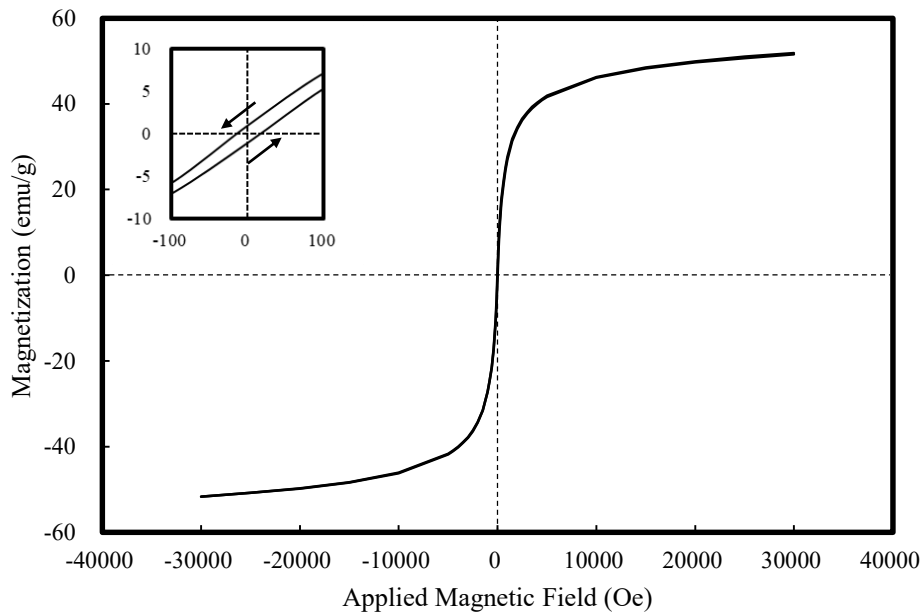


Figure 4.6 Magnetization curve of the SPIONPs synthesized from steelworks byproducts, and the same curve near the origin (inset). As shown in the inset, the hysteresis is very small that is a key property of superparamagnetism.

4.2. Functionalization of Superparamagnetic Iron Oxide Nanoparticles with Several Polymers

By functionalizing with PEG, PVA, and PAA, SPIONPs achieved stable dispersion in aqueous solution. If these polymers are attached onto the surface of the nanoparticles, they can induce electrostatic and steric repulsion between particles that prevents them from aggregating. The electrostatic repulsion comes from the functional groups in polymers. Functional groups such as hydroxyl, carboxyl, and amine in the polymers can be ionized and charged in aqueous conditions. Therefore, by functionalizing the nanoparticle surfaces with these polymers, charge can be given to the surfaces that can induce electrostatic repulsion between the particles.

Additionally, if particles with a polymer coating approach each other, the monomer concentration between the particles becomes higher than on the outside of the particles. Then, water molecules flow in between the particles due to the partial osmotic pressure caused by the monomer concentration difference (Fritz et al., 2002).



Figure 4.7 Dispersions of superparamagnetic iron oxide nanoparticles treated with polyethylene glycol (left), polyvinyl alcohol (middle), and polyacrylic acid (right), seven days after the synthesis of each dispersion.

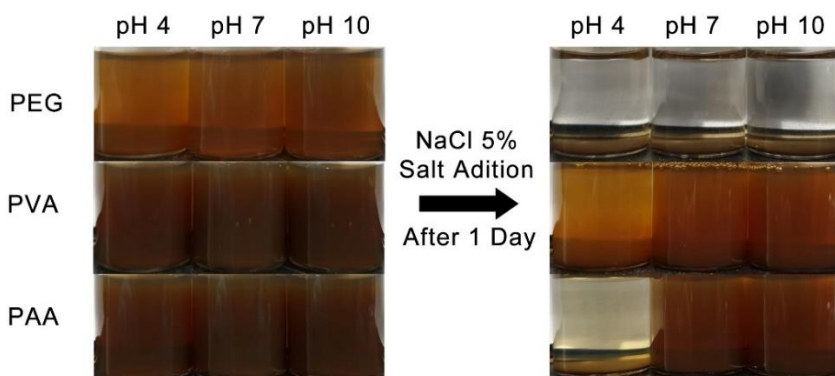


Figure 4.8 Dispersion stability test of PEG-, PVA-, and PAA-treated superparamagnetic iron oxide nanoparticles in 5 wt% NaCl brine. After 1 day, all the dispersions became lightened and visual confirmation of sedimentation was made.

From Figure 4.7, it can be seen that the polymer-treated SPIONPs remained stably dispersed for more than a week. Without any further treatment, no sedimentation nor changes in dispersion color was observed for the dispersions. However, with the addition of salt, all the nanoparticle dispersions made agglomerations (Figure 4.8). If the nanoparticle dispersion is unstable in the presence of salt, there are limitations to using them in the EOR field because they cannot pass through the small pores underground as mentioned previously (Hu, 2017).

In the presence of strong ionic strength, the surface potentials of the particles are shielded by counter-ions that are attracted to the charge. Therefore, the electric double-layer interaction, that can induce a repulsive force between particles, decreases (Adamson and Gast, 1997; Shaw, 1992). In addition, the length of the polymer brush tends to decrease if the ionic strength increases because the ions attach to the monomers and reduce the electrostatic repulsion between them (Willott et al., 2018; Zhulina and Rubinstein, 2012). As the length of the polymer brush decreases, the extent that the steric repulsion works decreases (Fritz et al., 2002).

For these reasons, the addition of salt destabilizes the nanoparticle dispersions that are functionalized with conventional polymers such as PEG, PVA, and PAA. Therefore, it is necessary to find other materials to functionalize SPIONPs for application in subsurface reservoir imaging, because of the higher salinity than that in general conditions.

4.3. Functionalization of Superparamagnetic Iron Oxide Nanoparticles with Sulfonated Phenolic Resin

As sulfonate groups can render a strong negative charge onto the SPIONPs by ionizing in aqueous solution, it is expected that the SPR-SPIONPs can form a more stable dispersion than other typical polymers. Prior to the dispersion stability test, the physical properties of the SPR-SPIONP were analyzed by several analysis.

To determine the distribution of hydrodynamic diameters of the synthesized particles, DLS analysis was conducted for a 40-times diluted sample of the SPR-SPIONP dispersion (Figure 4.9). The largest peak of the size distribution was observed at ~80 nm, and the z-average size of the particles was measured to be 73 nm. Both values are small enough to pass through underground pores (Hu, 2017). Although a secondary peak in the micron size range is observed, that is a result of irreversible aggregation of the nanoparticles during the synthesis process, it can be removed by filtration or selective centrifuge at low rpm. Therefore, SPR-SPIONPs can be applied to oil reservoirs.

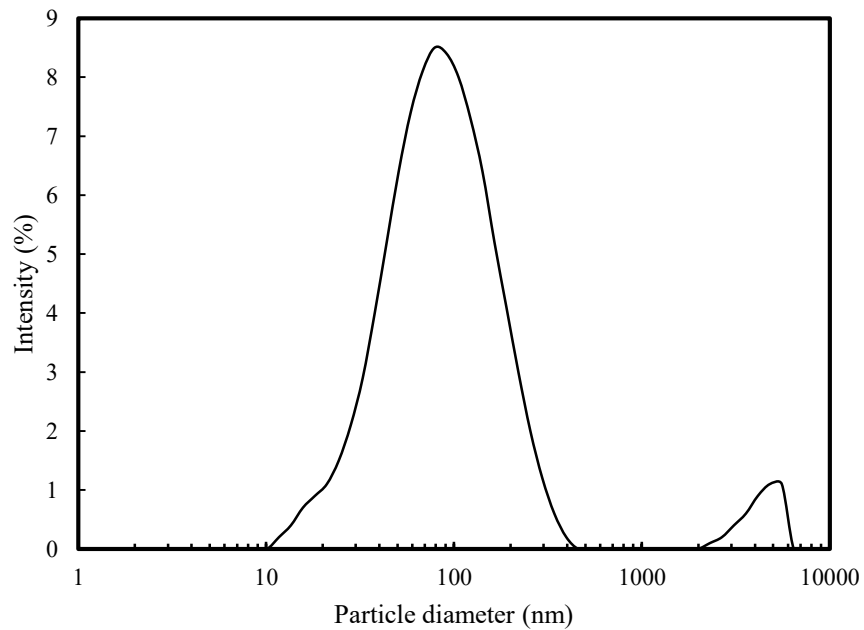


Figure 4.9 Size distribution of the SPR-SPIONPs analyzed by dynamic laser scattering.

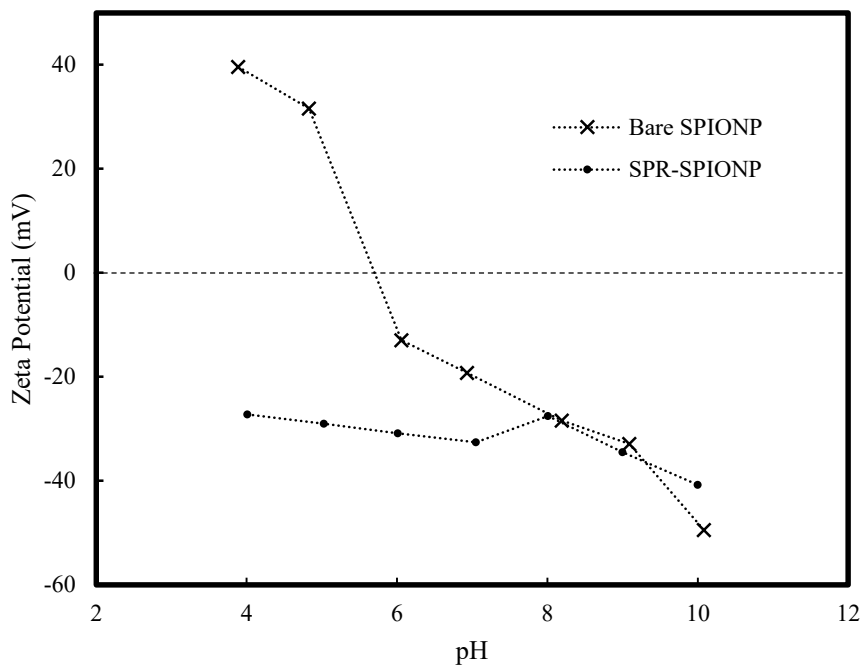


Figure 4.10 Zeta potential vs. pH curve of superparamagnetic nanoparticles without any further treatment (bare SPIONP, ×), and sulfonated phenolic resin-treated samples (SPR-SPIONP, •)

The zeta potential data of SPR-SPIONPs at several pHs were measured (Figure 4.10). If treated with SPR, the zeta potential of the SPIONPs become more negative in the range of pH 4 to 10. In this pH range, the zeta potential of the SPR-SPIONPs is between -25 and -45 mV. By ionizing in water, sulfonate groups in the SPR render a strong negative charge onto the surface of the nanoparticles. If the pH increases, the number of hydroxide ions in the water increases, and these can react with the hydrogen ions in the sulfonate group in the SPR. Therefore, ionization of the polymer tends to increase as the pH increases, that results in the lowering of the zeta potential.

To observe the morphology of the nanoparticles, TEM analysis was conducted. Figure 4.11a shows a low-magnification TEM image of the synthesized SPR-SPIONP sample, and Figure 4.11b shows the same sample laid on the edge of the holey carbon film at a higher magnification. From Figure 4.11a, aggregates sized in a range of 10 nm to 200 nm are observed, and from Figure 4.11b the aggregates consist of smaller particles in the range of a few nanometers and some amorphous materials surrounding the particles. The primary particle size distribution of the SPR-SPIONP is shown in Figure 4.12. Diameters of at least 150 particles were measured by analysis of TEM imaging, and the average primary particle size was calculated to 7.3 nm. Also, standard deviation of the size distribution was calculated to 5.6. Comparing with Figure 4.4, the primary particles were smaller than SPIONPs synthesized without the presence of SPR. The primary particles have crystalline structure with interplanar spacing of 0.249 nm (Figure 4.11b). The value is close to the reported value of the MNPs in a previous study (El Ghandoor et al., 2012).

Figure 4.13 shows the distribution of the Fe and S elements in the sample that are analyzed by STEM-EDS mapping. Figure 4.13a shows a STEM image of the sample and an area that is analyzed by EDS mapping (orange square); Figure 4.13b and c show the distributions of the Fe and S elements in the sample.

From Figure 4.13b and c, it can be shown that the Fe and S elements are almost identically distributed. In the sample, Fe comes from the SPIONPs and S comes from the SPR used for nanoparticle treatment. Therefore, the identical distribution of two elements means that the functionalization of the SPIONPs with SPR was done appropriately.

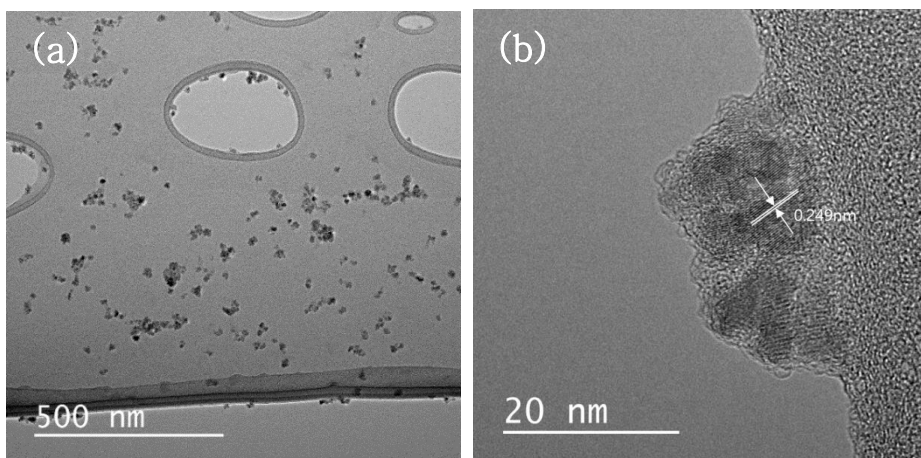


Figure 4.11 (a) TEM image of SPR-SPIONPs on a holey carbon grid at a low magnification; (b) the same sample at a higher magnification.

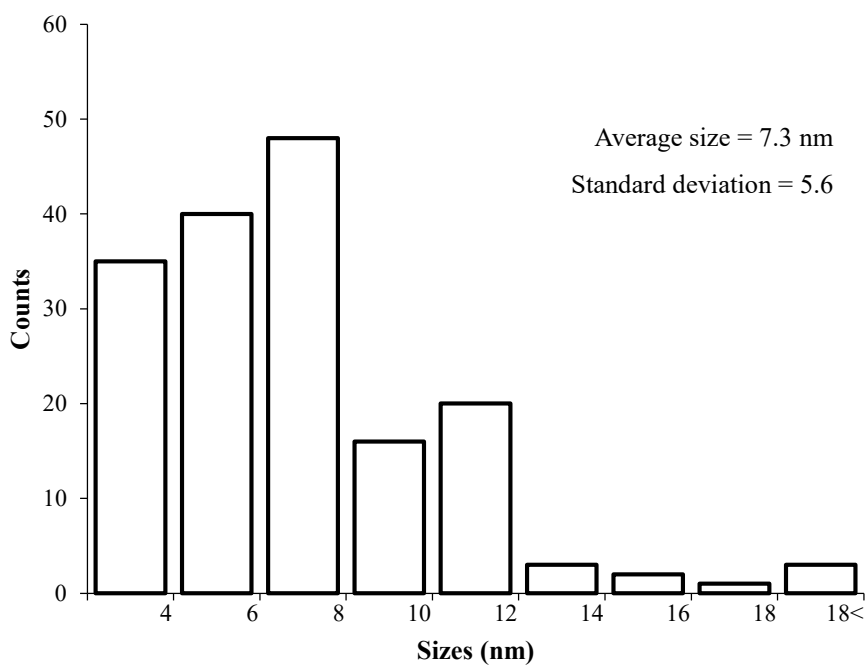


Figure 4.12 Primary particle size distribution of the SPR-SPIONP

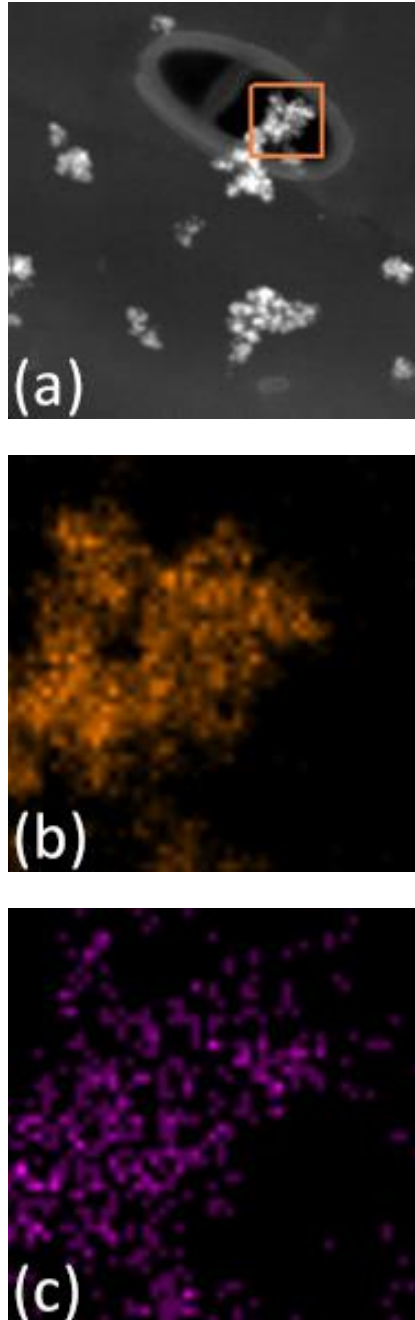


Figure 4.13 STEM-EDS analysis of the SPR-SPIONP sample for mapping the distribution of Fe and S elements: (a) squared area in this picture indicates where the analysis was conducted; (b) distribution of Fe elements in the squared area in (a); (c) distribution of S elements.

Thermogravimetric analysis was conducted to measure the organic content of the particles and their thermal stability (Figure 4.14). After the analysis, the total mass reduction was measured to be 51.99% of the initial mass. As 0.13% of the weight loss occurred at 107 °C, that portion of the weight loss can be considered moisture loss. Assuming there is no mass change owing to the oxidation of the iron oxide core because the analysis was conducted under a nitrogen atmosphere, the organic content of the SPR-SPIONPs can be estimated to be ~51.86 wt%. This content must be attributed to the SPR used to functionalize the SPIONPs. Also from Figure 4.14, a rapid reduction in mass of the SPR-SPIONPs at 700 °C can be seen that indicates that the most of the organic content decomposes at this temperature.

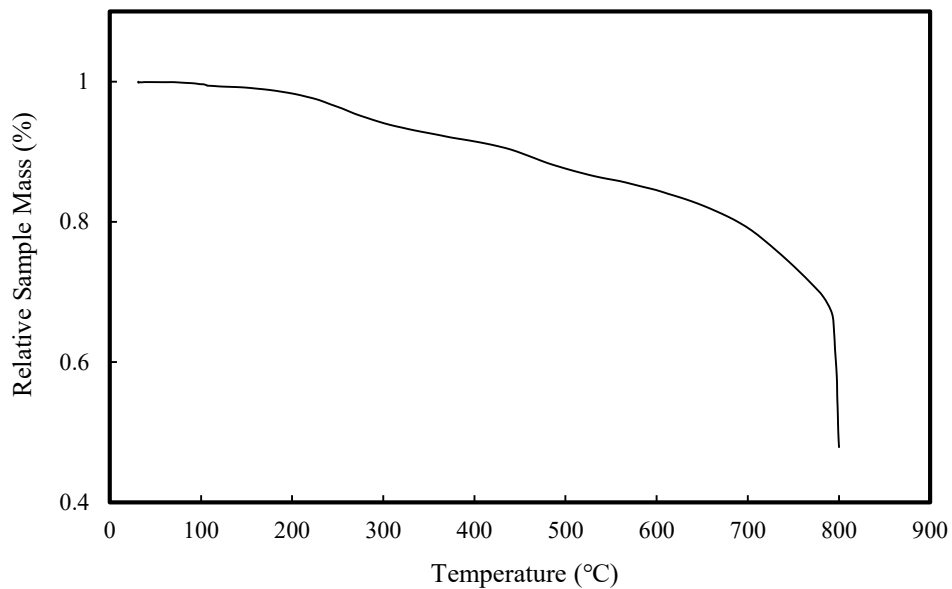


Figure 4.14 Thermogravimetric analysis of SPR-SPIONPs.

The magnetization property of the SPR-SPIONPs was measured with VSM, and the results are displayed in Figure 4.15 and Figure 4.16. In the inset of Figure 4.15, virtually no magnetization hysteresis was observed near the origin, implying that the sample is superparamagnetic (Guimarães, 2009). The magnetic susceptibility of the SPR-SPIONP was calculated by using the data where the magnetization of sample is 85 % of saturation magnetization (Figure 4.16). Consequently, the mass magnetic susceptibility of the SPR-SPIONP was calculated to 8.97×10^{-3} emu/g·Oe. The value becomes $0.713 \text{ m}^3/\text{kg}$ if converted to SI unit, and by dividing this value with the density of SPR-SPIONP, the magnetic susceptibility of the SPIONPs can be obtained as 2.10×10^3 . The saturation magnetization of the SPR-SPIONPs was measured to be ~ 16.5 emu/g. As the organic content of the particle was measured to be ~ 47.88 wt% from thermogravimetric analysis, the saturation magnetization of the iron oxide alone can be calculated as 34.5 emu/g. This value is smaller than that of typical MNPs (Sato et al., 1987). This reduction in saturation could be attributed to the reduction in the size of the primary particles. If the primary particle size of SPIONPs decreases, the saturation magnetization tends to decrease (Mascolo et al., 2013). In addition, if the surface atoms of SPIONPs interact with the surfactants or polymer molecules by functionalization, the magnetic phase of the nanoparticles is reduced (Yuan et al., 2012). These could be the reasons for the reduction in saturation magnetization when SPIONPs are functionalized with SPR.

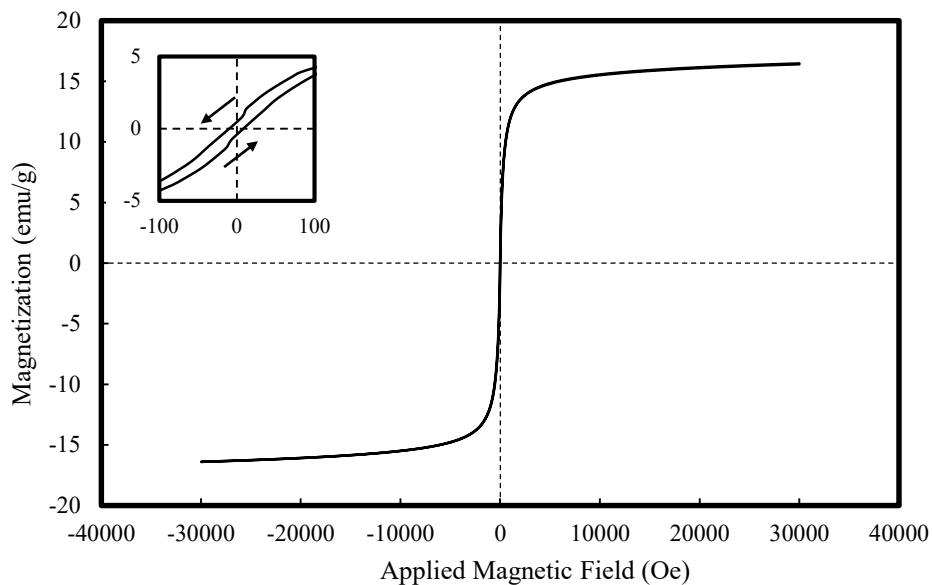


Figure 4.15 Magnetization curve (Langevin) of SPR-SPIONPs, and the same curve near the origin (inset).

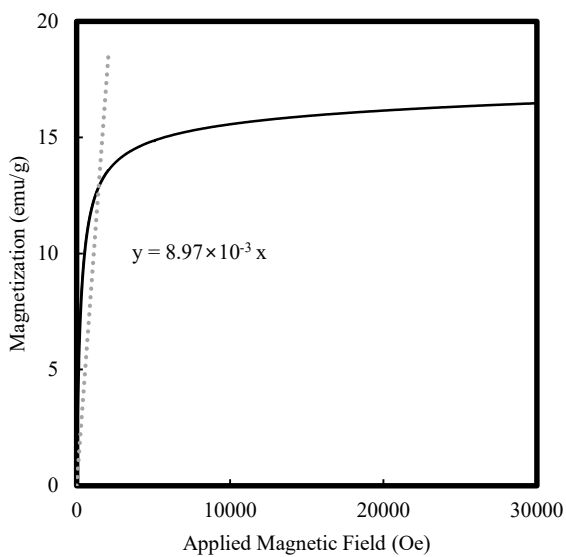


Figure 4.16 Calculation of magnetic susceptibility of SPR-SPIONP

The dispersion stability of SPR-SPIONPs against salinity was evaluated in different pHs and salinities. For the test, the pH of 0.5 wt% of SPR-SPIONP dispersion was adjusted with 1M NaOH and 1M HCl solutions. Different amounts of NaCl were added to the dispersion, and the stability was then evaluated by visual confirmation of particle aggregates or sedimentation over one week.

Figure 4.17 shows the results of the dispersion stability test. It can be seen that the SPR-SPIONP stayed dispersed for a week between pH 7 and 10, otherwise forming aggregate in the range from pH 4 to 10. At pH 10, the dispersion stayed stable even in NaCl 10 wt% solution (Figure 4.18). In contrast, the stability of the SPR-SPIONPs decreased when the pH decreased. Consequently, the SPR-SPIONPs showed an improved dispersion stability compared to other polymer-treated SPIONPs in Chapter 4.2. As sulfonate groups are known not to form insoluble salts in the presence of electrolytes (Rosen, 1989), the sodium salts in the solution bind less to SPR than to the other polymers. Therefore, the SPR-SPIONPs can stay dispersed in the NaCl 5 wt% solution. However, the bond between SPRs and SPIONPs becomes unstable in acidic conditions where hydrogen ions can attack the bond (Yee et al., 1999). Therefore, the SPRs may dissociate from the SPIONPs in acidic conditions with the presence of electrolyte, resulting in a reduction of stability of the SPR-SPIONP dispersions.

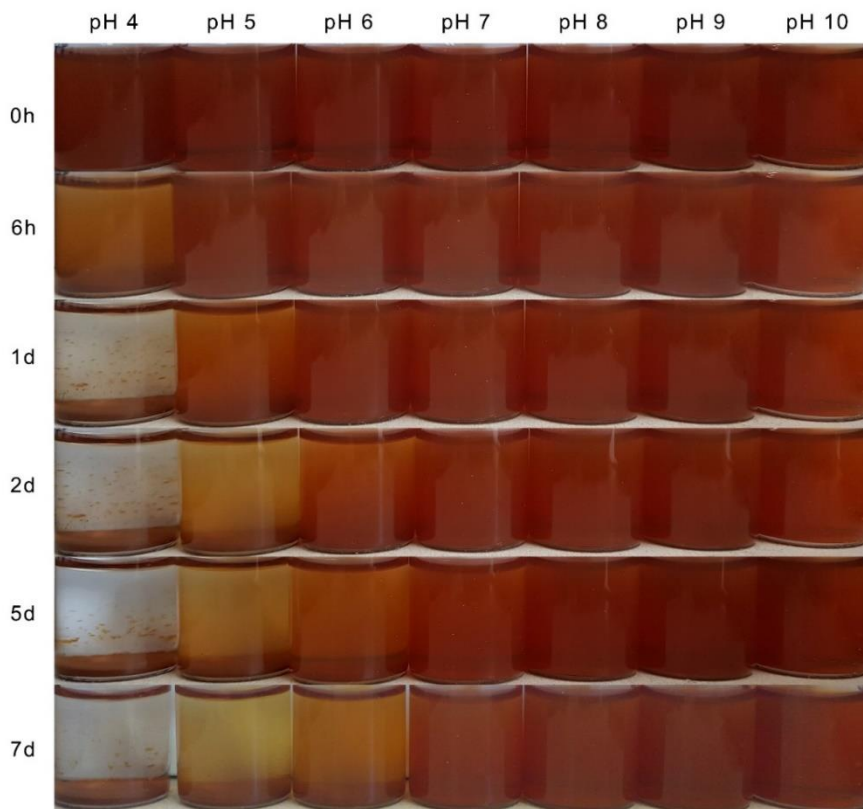


Figure 4.17 Dispersion stability of SPR-SPIONP dispersion in 5 wt% NaCl solutions at several pH values over one week. From pH 7 to 10, the dispersion stayed stable, while in acidic conditions the dispersion formed aggregate and settled.



Figure 4.18 Stable dispersion of SPR-SPIONPs achieved in 10 wt% NaCl solutions at pH 10.

Supporting analysis was conducted to confirm the dissociation of the SPR-SPIONPs. Two samples of freshly prepared SPR-SPIONPs and samples that were put in 5 wt% NaCl solution at pH 4 for one day were analyzed with STEM-EDS; the results are shown in Figure 4.19 and Table 4.2.

Figure 4.19a and c show the spots where the EDS analysis was conducted in the sample, and Figure 4.19b and d show the X-ray spectra collected from these spots. The peaks representing each element are indicated in the figures. Figure 4.19a and b are the results of the freshly prepared SPR-SPIONP sample, and Figure 4.19c and d are the results of the samples that were put in NaCl 5 wt% solution at pH 4. Table 4.2 shows the atomic ratios of Fe and S in each spot that were calculated from quantitative analysis of the EDS spectra. It is found that the Fe/S ratio, indicating how highly the SPIONPs are functionalized with SPR, is reduced in the sample under the conditions of NaCl 5 wt% and pH 4. From this analysis, it can be seen that the SPR is dissociated from the SPIONP surface in acidic and saline conditions (Park et al., 2019).

Table 4.2 Atomic ratio between Fe and S at the spots indicated in Figure 4.19a and c, determined by STEM-EDS analysis.

Atom	Atomic ratio (%)	
	Freshly prepared	In 5 wt% NaCl at pH 4
Fe	86.5	99.9
S	13.5	0.1

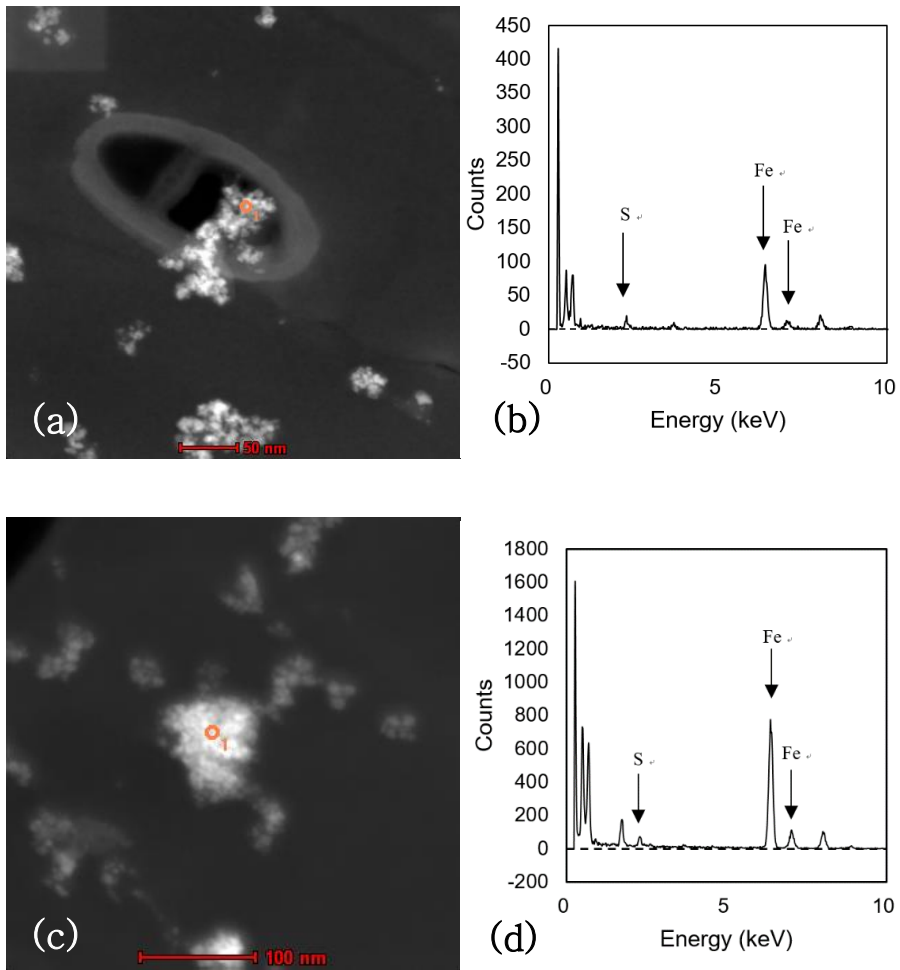


Figure 4.19 STEM-EDS analysis of freshly prepared SPR-SPIONP (a, b), and the same sample put in a 5 wt% NaCl solution at pH 4 (c, d).

4.4. Functionalization of Superparamagnetic Iron Oxide Nanoparticles with Crosslinked Shells of SPR and PVA

In Chapter 4.3, the dissociation of SPR coating in 5 wt% NaCl solution under acidic conditions was observed, and this causes unstable dispersion and aggregate. Therefore, it is required to use a crosslinking agent such as PVA to improve the stability of the SPR coating.

Superparamagnetic iron oxide nanoparticles with crosslinked polymer shells were characterized via several methods. Figure 4.20 shows the hydraulic size distribution of SPIONPs with crosslinked polymer shells. The z-average size of the crosslinked SPR-SPIONP was measured to be 115.1 nm that is bigger than that of SPR-SPIONP without crosslink. This could be caused by the increase of polymeric shell thickness and crosslink between more than two of particles. However, this value is small enough to pass through underground pores. Therefore, crosslinked SPR-SPIONP can be applied to oil field. The pH-zeta graph of the nanoparticle complex was measured (Figure 4.21). From the zeta potential measurements, it can be seen that SPIONPs with crosslinked shells have stronger negative surface potentials than those without crosslinking. This can be caused by ionization of hydroxyl functional groups in PVA.

Next, a colloidal stability test of the nanoparticles was conducted. The pH of the dispersion was set to 4, 7, and 10, and sodium chloride was added to the dispersion. Without crosslinking, the nanoparticle dispersion became unstable with the addition of salt under acidic conditions (Figure 4.17); however, by

crosslinking, an improvement in the nanoparticle dispersion stability under salinity and acidic conditions was observed.

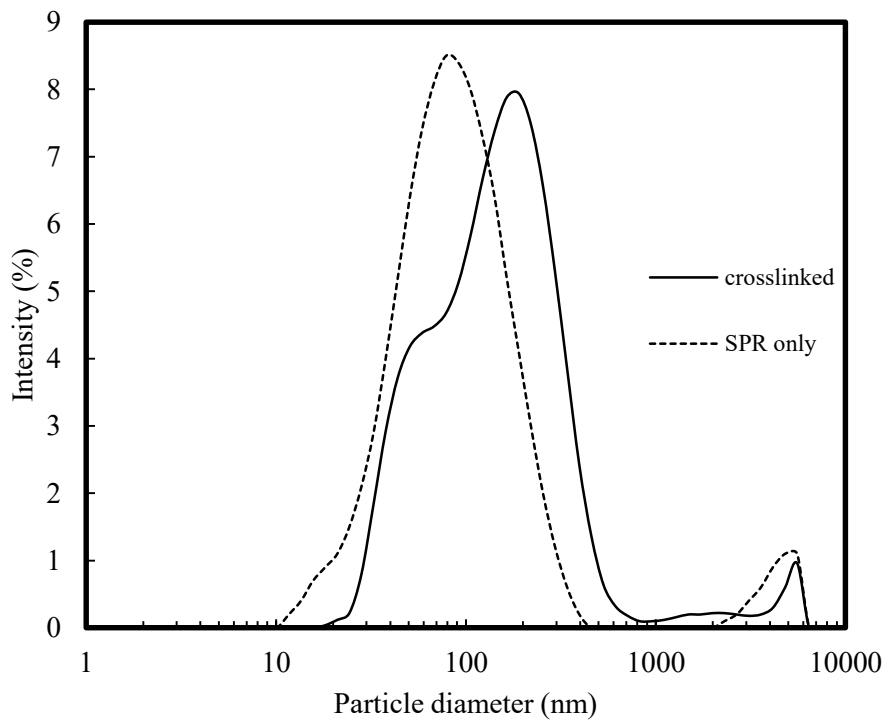


Figure 4.20 Size distribution of SPR-SPIONP and crosslinked SPR-SPIONP.

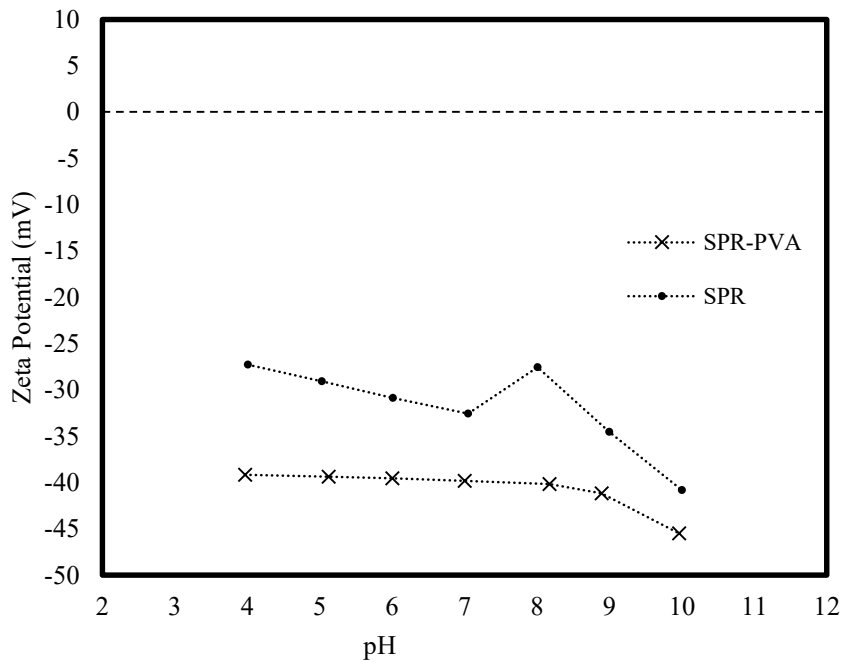


Figure 4.21 pH–zeta potential curve of superparamagnetic iron oxide nanoparticles with SPR.

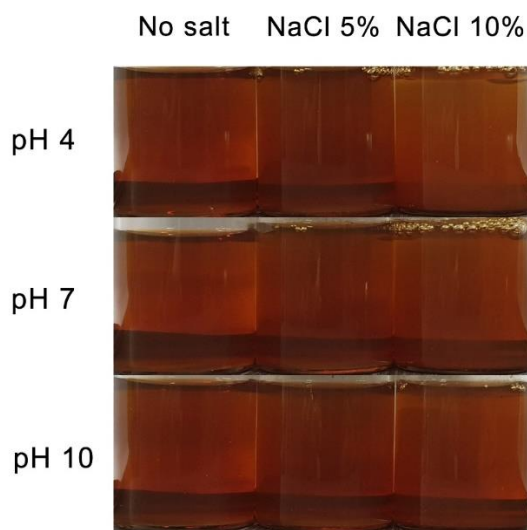


Figure 4.22 Dispersions of SPR-SPIONPs with PVA crosslink after one week in sodium chloride solutions. Compared to the dispersion without salt addition, no change in color or formation of sedimentation was observed.



Figure 4.23 Dispersions of SPR-SPIONP with PVA crosslink in API brine (8 wt% NaCl + 2 wt% CaCl₂ solution).

Figure 4.22 shows the dispersion of crosslinked SPR-SPIONP dispersions after one week. It can be seen that stable dispersion is maintained at pH 4 for one week. Enhanced dispersion stability in 10 wt% NaCl was observed. Without crosslinking, the dispersions were unstable in 10 wt% NaCl at pH 10, and even at pH 10, the dispersion was only stable for a few days. However, with crosslinking, the nanoparticle dispersion remained stable at pH 7 and pH 10 for a week. At pH 4, the dispersion was less stable in 10 wt% NaCl solution, and particle sedimentation was observed.

In an underground reservoir, there are divalent cations such as Ca^{2+} and Mg^{2+} as well as monovalent cations such as Na^+ . As the valence of an ion increases, ionic strength increases in proportion to its square. Therefore, even with a small number of divalent cations, the electrostatic repulsion between particles can be significantly weakened. Moreover, API brine that is used as a standard for testing brine in petroleum engineering, is composed of 8 wt% NaCl and 2 wt% CaCl_2 . Therefore, the dispersion stability of crosslinked SPR-SPIONPs was studied in API brine. Without crosslinking, the SPR-SPIONP dispersion was not stable in API brine and formed aggregate almost immediately. However, with crosslinking with PVA, the SPR-SPIONPs can stay dispersed for longer without forming sedimentation (Figure 4.23).

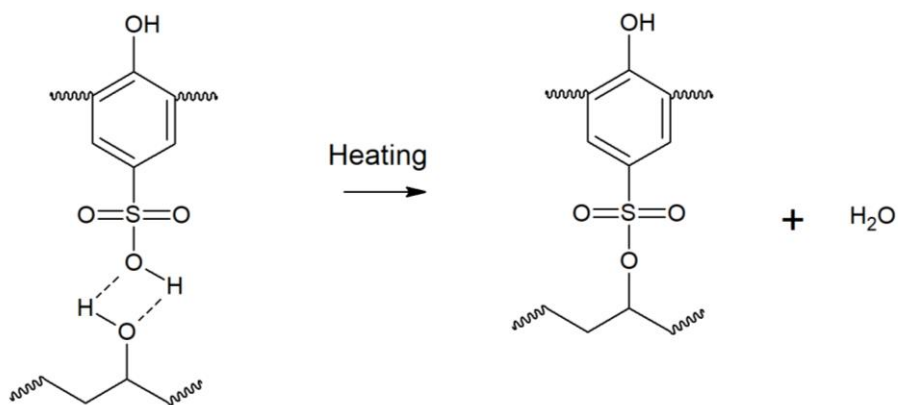
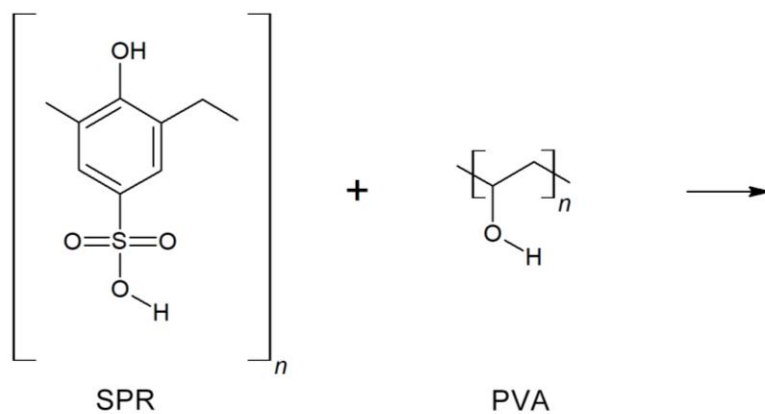


Figure 4.24 Crosslinking process of sulfonated phenolic resin and polyvinyl alcohol.

Figure 4.24 shows the detailed crosslinking mechanism of SPR and PVA. When PVA is added to the SPR-SPIONP solution, the hydroxyl groups in PVA can make hydrogen bonds with the sulfonate groups in SPR. Then, under heating, the two functional groups can form a bond by water-removing acid–base reaction. Therefore, with a strong hydrogen bond and covalent bond after the acid–base reaction, the two polymers can make a crosslinked structure (Wu et al., 2006). Because of the net-like structure that is formed by crosslinking of the polymers, the stability of the SPR shell can be enhanced, resulting in reduced dissociation from the iron oxide core.

To support this hypothesis, TEM analysis was conducted on the crosslinked SPR-SPIONPs before and after salt addition. To compare this with the result in Chapter 4.3, the crosslinked SPR-SPIONPs were put in 5 wt% NaCl solution at pH 4 for a week. The dispersion was then centrifuged at 20,000 rpm to separate the particles from the solution. From the particles, a TEM sample of crosslinked SPR-SPIONP after salt addition was made.

Figure 4.25 shows the TEM image of crosslinked SPR-SPIONP. The morphology of the particle was almost similar with SPR-SPIONP particles without crosslink. Aggregates in a size range of 10 to 200 nm were seen from the image. Each aggregate consists of smaller crystalline particles and some amorphous materials surrounding them.

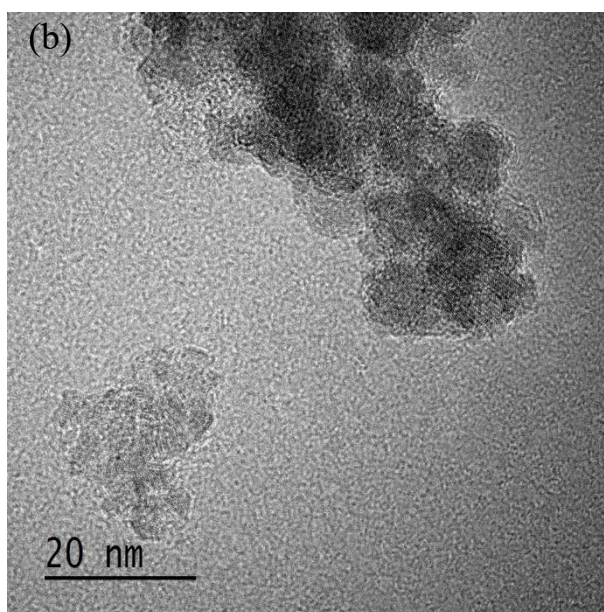
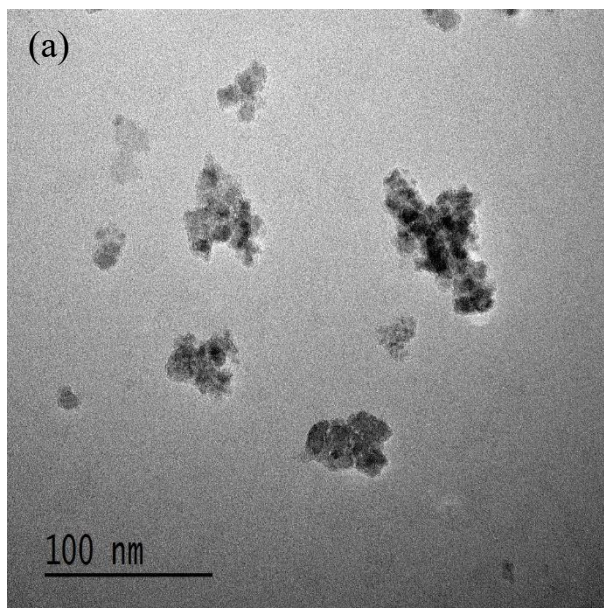


Figure 4.25 (a) TEM image of crosslinked SPR-SPIONP and (b) an image of the same sample at a higher magnitude.

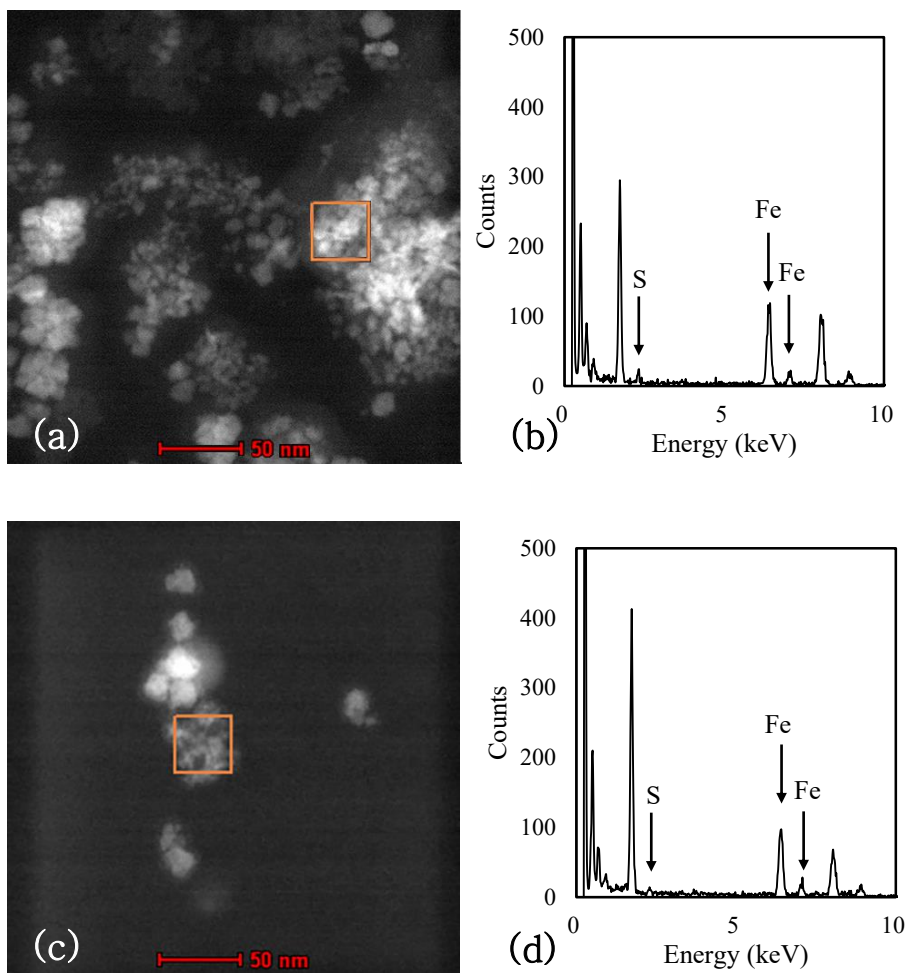


Figure 4.26 STEM-EDS analysis of crosslinked SPR-SPIONP (a, b), and the same sample put in a 5 wt% NaCl solution at pH 4 (c, d).

Table 4.3 Atomic ratio between Fe and S at the areas indicated (orange square) in Figure 4.26a and c determined by STEM-EDS analysis

Atom	Atomic ratio (%)	
	Freshly prepared	In 5 wt% NaCl at pH 4
Fe	93.99	93.38
S	6.00	6.61

Figure 4.26 and Table 4.3 show the result of STEM-EDS analysis of crosslinked SPR-SPIONP. Figure 4.26 (a) and (b) show the EDS result of freshly prepared sample and (c) and (d) show the result of the sample in 5 wt% NaCl solution at pH 4 for a week. The areas where the STEM-EDS analysis was conducted are indicated with orange squares in Figure 4.26 (a) and (c). Table 4.3 shows the atomic ratio calculated from the quantitative analysis of EDS spectra. It can be seen that the Fe/S ratio is not changed significantly even after the addition of salt under an acidic condition; this implies that the polymer coating of the iron oxide nanoparticle is stable under high salinity.

Compared to the value of Table 4.2, the S ratio of crosslinked SPR-SPIONP is lower than that of SPR-SPIONP without crosslinking. This is because PVA that was employed as a crosslinking agent, reacted with SPR shell and with the surface of the SPIONPs, thus being competitively adsorbed to the surface against SPR. However, this reduction of atomic ratio of S did not facilitate the reduction of the dispersion stability of SPR-SPIONP, and

particularly improved the dispersion stability by stabilizing the SPR shell by crosslinking.

4.5. Discussions and Further Studies

The superparamagnetic iron oxide nanoparticles that can stay dispersed under high salinity is synthesized. First, SPIONPs with small size and good magnetic performance were synthesized by the co-precipitation method from steelworks byproducts. There are some limitations to this synthesis process. Particularly, it is difficult to precisely quantify the Fe^{2+} ion concentration during the partial reduction of the solution, and the polydispersity of primary particle size of the SPIONP can be excessively high with the co-precipitation method. However, the stoichiometric ratio between Fe^{2+} and Fe^{3+} and polydispersity of the SPIONPs are less important than other properties of the SPIONPs for the cross-well electromagnetic tomography. For the cross-well electromagnetic tomography, it is sufficient to ensure that the nanoparticle can form a magnetic gradient with respect to the target area against the background area and have sufficiently small size to pass through underground pores. Thus, the most important factor is the magnetic behavior and the cluster size distribution of the nanoparticles. Therefore, the process is feasible. In conclusion, high-quality, and high-valued SPIONPs can be synthesized by recycling steelworks byproducts. Moreover, the cost of the synthesis of magnetite nanoparticles can be reduced because waste materials and inexpensive polymers are used for the

synthesis and functionalization process.

For the stability test, each dispersion is set to have approximately 0.5 wt% of nanoparticle concentration. The magnetic susceptibility of SPR-SPIONP is $2.11 \times 10^3 \text{ m}^3$ and the effective magnetic permeability of 0.5 wt % of the SPR-SPIONP dispersion is computed with the conventional Maxwell-Garnett formula (Sihvola A., 1999):

$$\mu_{eff} = \mu_e + \frac{2\mu_e(\mu_i - \mu_e)}{\mu_i + \mu_e - f(\mu_i - \mu_e)} \quad (11),$$

where μ_{eff} is the effective permeability of dispersion, μ_i is the permeability of inclusion that is randomly located with the volume fraction f , and μ_e is the permeability of the media. Assuming the dispersion media is pure water, the effective permeability of 0.5 wt% SPR-SPIONP dispersion can be calculated as 3.50. A magnetic susceptibility value of general sandstone ranges from 0 to 2.16×10^{-2} (Hunt et al., 1995), with resulting magnetic permeability from 1 to 1.02. In Rahmani's model, the permeability of magnetic anomaly was set to twice of the background. Therefore, it is feasible to set the concentration of magnetic dispersion to 0.5 wt%.

By functionalizing SPIONPs with sulfonated phenolic resin, the dispersion with the 0.5 wt% of nanoparticles did not form agglomerations or make a change in color in NaCl 5 wt% solutions at pH 7 to 10 for more than a week. Also, the dispersion stability in acidic conditions can be enhanced by crosslinking the SPR shell with poly vinyl alcohol. Typical salinities for

sandstone based oil reservoirs is about 30g/L (Oruwori and Ikiensikimam, 2010). The SPR functionalized SPIONP can stay dispersed in a typical sandstone oil reservoir. However, in carbonates based oil reservoirs, the salinity can increase to 90g/L. Therefore, the dispersion stability test at higher salinities such as NaCl 10 wt% solution and API brine (NaCl 8 wt% + CaCl₂ 2 wt% solution) is conducted for crosslinked SPR-SPIONPs. From the test, the enhancement of short-term dispersion stability was observed, however the visual confirmation of aggregation and color change of dispersion was made after three days. Therefore, the SPR-SPIONPs should be carefully used with the consideration of the rocks that form the oil reservoir and the retention time of the nanoparticles underground.

However, this research requires further studies. This study focused on achieving stable dispersion of SPIONPs under the high salinity condition, but the dispersion stability of SPIONPs was not examined under high temperature or high pressure, and other extreme conditions in underground reservoir. Also, core flooding tests and field injection tests were not be conducted. The behavior of the nanoparticles in these tests must be confirmed to utilize them in real petroleum industry. Therefore, relevant experiments is required in future studies.

Chapter 5. Conclusions

In this thesis, a process of synthesis and functionalization of SPIONPs applicable to crosswell electromagnetic tomography in oil field exploration and production was designed. To achieve this, two critical challenges namely high synthesis cost of SPIONPs, and their low dispersibility in underground high-salinity conditions is addressed.

A process of synthesizing SPIONPs from steelworks byproducts is developed. Superparamagnetic iron oxide nanoparticles is obtained as a byproduct of a pickling process. The synthesis procedure is as following: (i) the steelworks byproducts are leached in an acid solution; (ii) one-third of the iron ion solution is reduced by sodium borohydride; (iii) the reduced solution is mixed with the other solution; (iv) the SPIONPs are co-precipitated by adding the alkali. The high quality of the synthesized nanoparticles was ascertained via TEM analysis and magnetization measurement with a VSM. By this process, superparamagnetic iron oxide nanoparticles, a high-value product, can be synthesized from the steelworks byproduct. Also, the cost of synthesis of SPIONPs can be reduced.

The stability of SPIONP dispersion under high-salinity is improved by functionalization of the particles with polymer molecules. Frequently used polymers such as PEG, PVA, and PAA were applied to functionalize SPIONPs. From functionalizing these particles, general dispersion of SPIONPs was

achieved. However after adding salt, the dispersion was unstable and formed aggregates.

Consequently, SPR is suggested as an alternative. The rich sulfonate groups in the polymer binds with SPIONPs by acid–base reactions with the surface hydroxyl group of the iron oxide, while the unbound sulfonate groups induce highly negative charge onto the particles by highly ionizing in water particularly in saline conditions. Additionally, the SPR can be synthesized by simply mixing and heating 4-hydroxy benzenesulfonic acid and formaldehyde. This simplified process of polymer synthesis reduces the overall cost of SPIONP synthesis. The functionalization of the SPIONPs can be achieved in a one-pot manner by adding the polymer during the co-precipitation step. The synthesized SPIONPs stay dispersed in 5 wt% solution of sodium chloride for one week in both neutral and basic conditions. Particle size analysis, zeta potential measurement, thermogravimetric analysis, TEM studies, EDS mapping, and VSM magnetization measurements were conducted to characterize the SPR-SPIONPs. From the analysis, the in-situ functionalization of SPIONPs with SPR in the co-precipitation process is successfully conducted.

The dispersion stability of the SPR-SPIONPs is further improved by crosslinking with PVA. The PVA treatment of SPR-SPIONPs increases the SPR shell stability because the polymers makes a crosslinked structure with the SPR shells. Consequently, the dissociation of SPR from the SPIONPs in acidic conditions is prevented. Additionally, the PVA contributes to enhancing steric or electrostatic repulsion between nanoparticles. Therefore, the SPR-SPIONPs stays dispersed in neutral, basic conditions and acidic conditions. The PVA

treatment enhances the dispersion stability of the particles particularly in the presence of calcium ions.

In conclusion, a novel method of synthesis and functionalization of SPIONPs applicable in EOR field is developed by: (i) synthesizing the SPIONPs from low-cost ingredients such as byproducts from steelworks processes; (ii) utilizing low-cost polymers for functionalization of nanoparticles; and (iii) simply mixing and heating reagents, without using complicated processes. The high-salinity stable dispersion of SPIONPs can be utilized in several fields that deals highly saline condition other than petroleum industry, such as sewage treatment and marine industry. Functionalization with SPR can expand the use of SPIONPs.

References

- Adamson, A. W. and Gast, A. P. (1997). *Physical chemistry of surfaces* (6th ed.). New York: Wiley.
- Agenet, N., Perriat, P., Brichart, T., Crowther, N., Martini, M. and Tillement, O. (2012). *Fluorescent Nanobeads: a First Step Toward Intelligent Water Tracers*. Paper presented at the SPE International Oilfield Nanotechnology Conference and Exhibition, Noordwijk, The Netherlands.
- Agista, M., Yu, Z. and Guō, K. (2018). A State-of-the-Art Review of Nanoparticles Application in Petroleum with a Focus on Enhanced Oil Recovery. *Applied Sciences*, 8.
- Ahmadi, M. A. and Shadizadeh, S. R. (2012). Adsorption of Novel Nonionic Surfactant and Particles Mixture in Carbonates: Enhanced Oil Recovery Implication. *Energy & Fuels*, 26(8), 4655-4663.
- Ahmadi, M. A. and Shadizadeh, S. R. (2013). Experimental investigation of adsorption of a new nonionic surfactant on carbonate minerals. *Fuel*, 104, 462-467.
- Al-Muntasheri, G. A., Liang, F. and Hull, K. L. (2017). Nanoparticle-Enhanced Hydraulic-Fracturing Fluids: A Review. *SPE Production & Operations*, 32(02), 186-195.
- Al-Sayari, S., Carley, A. F., Taylor, S. H. and Hutchings, G. J. (2007). Au/ZnO and Au/Fe₂O₃ catalysts for CO oxidation at ambient temperature:

comments on the effect of synthesis conditions on the preparation of high activity catalysts prepared by coprecipitation. *Topics in Catalysis*, 44(1), 123-128.

Ali, J. A., Kolo, K., Manshad, A. K. and Mohammadi, A. H. (2018). Recent advances in application of nanotechnology in chemical enhanced oil recovery: Effects of nanoparticles on wettability alteration, interfacial tension reduction, and flooding. *Egyptian Journal of Petroleum*, 27(4), 1371-1383.

Babu, K. and Dhamodharan, R. (2008). Grafting of Poly(methyl methacrylate) Brushes from Magnetite Nanoparticles Using a Phosphonic Acid Based Initiator by Ambient Temperature Atom Transfer Radical Polymerization (ATATRP). *Nanoscale Research Letters*, 3(3), 109.

Babu, K. and Dhamodharan, R. (2009). Synthesis of Polymer Grafted Magnetite Nanoparticle with the Highest Grafting Density via Controlled Radical Polymerization. *Nanoscale Research Letters*, 4(9), 1090-1102.

Bagaria, H. G., Neilson, B. M., Worthen, A. J., Xue, Z., Yoon, K., Cheng, V., Lee, J., Velaga, S., Huh, C., Bryant, S. L., Bielawski, C. W., Johnston, K. P., and Johnston, K. P. (2013). Adsorption of iron oxide nanoclusters stabilized with sulfonated copolymers on silica in concentrated NaCl and CaCl₂ brine. *Journal of Colloid and Interface Science*, 398, 217-226.

Bagaria, H. G., Xue, Z., Neilson, B. M., Worthen, A. J., Yoon, K., Nayak, S., Cheng, V., Lee, J., Bielawski, C. W., and Johnston, K. P. (2013). Iron

Oxide Nanoparticles Grafted with Sulfonated Copolymers are Stable in Concentrated Brine at Elevated Temperatures and Weakly Adsorb on Silica. *Acs Applied Materials & Interfaces*, 5(8), 3329-3339.

Bagaria, H. G., Yoon, K., Neilson, B. M., Cheng, V., Lee, J., Worthen, A. J., Xue, Z., Huh, C., Bryant, S. L., Bielawski, S. L., Bielawski, C. W. and Johnston, K. P. (2013). Stabilization of Iron Oxide Nanoparticles in High Sodium and Calcium Brine at High Temperatures with Adsorbed Sulfonated Copolymers. *Langmuir*, 29(10), 3195-3206.

Bean, C. P. and Livingston, J. D. (1959). Superparamagnetism. *Journal of Applied Physics*, 30(4), S120-S129. doi:10.1063/1.2185850

Bose, C. C., Gul, A., Fairchild, B., Jones, T. and Barati, R. (2015). *Nano-Proppants for Fracture Conductivity Improvement and Fluid Loss Reduction*. Paper presented at the SPE Western Regional Meeting, Garden Grove, California, USA.

Brown, W. F. (1963). Thermal Fluctuations of a Single-Domain Particle. *Physical Review*, 130(5), 1677-1686.

Bruchez, M., Moronne, M., Gin, P., Weiss, S. and Alivisatos, A. P. (1998). Semiconductor nanocrystals as fluorescent biological labels. *Science*, 281(5385), 2013-2016.

Chapman, D. L. (1913). LI. A contribution to the theory of electrocapillarity. *The London, Edinburgh, and Dublin Philosophical Magazine and Journal of Science*, 25(148), 475-481. doi:10.1080/14786440408634187

Chatterjee, J., Haik, Y. and Chen, C.-J. (2001). Modification and

characterization of polystyrene-based magnetic microspheres and comparison with albumin-based magnetic microspheres. *Journal of Magnetism and Magnetic Materials*, 225(1), 21-29.

Chauhan, N., Narang, J., Meena and Pundir, C. S. (2012). An amperometric glutathione biosensor based on chitosan–iron coated gold nanoparticles modified Pt electrode. *International Journal of Biological Macromolecules*, 51(5), 879-886.

Cheraghian, G., Khalilinezhad, S. S., Kamari, M., Hemmati, M., Masihi, M. and Bazgir, S. (2014). Adsorption polymer on reservoir rock and role of the nanoparticles, clay and SiO₂. *International Nano Letters*, 4(3), 114.

Chu, S. and Majumdar, A. (2012). Opportunities and challenges for a sustainable energy future. *Nature*, 488, 294.

Chuah, K., Lai, L. M. H., Goon, I. Y., Parker, S. G., Amal, R. and Justin Gooding, J. (2012). Ultrasensitive electrochemical detection of prostate-specific antigen (PSA) using gold-coated magnetic nanoparticles as ‘dispersible electrodes’. *Chemical Communications*, 48(29), 3503-3505.

Crews, J. B., Huang, T. and Wood, W. R. (2008a). *The Future of Fracturing-Fluid Technology and Rates of Hydrocarbon Recovery*. Paper presented at the SPE Annual Technical Conference and Exhibition, Denver, Colorado, USA.

Crews, J. B., Huang, T. and Wood, W. R. (2008b). New Technology Improves Performance of Viscoelastic Surfactant Fluids. *SPE Drilling &*

Completion, 23(01), 41-47.

del Hierro, I., Pérez, Y. and Fajardo, M. (2018). Silanization of Iron Oxide Magnetic Nanoparticles with ionic liquids based on amino acids and its application as heterogeneous catalysts for Knoevenagel condensation reactions. *Molecular Catalysis*, 450, 112-120.

Dickson, J. L., Binks, B. P. and Johnston, K. P. (2004). Stabilization of Carbon Dioxide-in-Water Emulsions with Silica Nanoparticles. *Langmuir*, 20(19), 7976-7983.

Dobson, J. (2006). Magnetic nanoparticles for drug delivery. *Drug Development Research*, 67(1), 55-60.

Dresco, P. A., Zaitsev, V. S., Gambino, R. J. and Chu, B. (1999). Preparation and Properties of Magnetite and Polymer Magnetite Nanoparticles. *Langmuir*, 15(6), 1945-1951.

Dutrizac, J. E., and Monhemius, A. J. (1986). *Iron control in hydrometallurgy*. Chichester; New York: E. Horwood; Halsted Press.

El Ghandoor, H., Zidan, H. M., Khalil, M. M. H. and Ismail, M. I. M. (2012). Synthesis and Some Physical Properties of Magnetite (Fe₃O₄) Nanoparticles. *International Journal of Electrochemical Science*, 7(6), 5734-5745.

Fakoya, M. F. and Shah, S. N. (2014). *Enhancement of Filtration Properties in Surfactant-Based and Polymeric Fluids by Nanoparticles*. Paper presented at the SPE Eastern Regional Meeting, Charleston, WV, USA.

Feng, B., Hong, R. Y., Wang, L. S., Guo, L., Li, H. Z., Ding, J., Zheng, Y. and Wei, D. G. (2008). Synthesis of Fe₃O₄/APTES/PEG diacid

- functionalized magnetic nanoparticles for MR imaging. *Colloids and Surfaces A: Physicochemical and Engineering Aspects*, 328(1), 52-59.
- Flesch, C., Unterfinger, Y., Bourgeat-Lami, E., Duguet, E., Delaite, C. and Dumas, P. (2005). Poly(ethylene glycol) Surface Coated Magnetic Particles. *Macromolecular Rapid Communications*, 26(18), 1494-1498.
- Fritz, G., Schadler, V., Willenbacher, N. and Wagner, N. J. (2002). Electrosteric stabilization of colloidal dispersions. *Langmuir*, 18(16), 6381-6390.
- Fu, C., Yu, J. and Liu, N. (2018). Nanoparticle-stabilized CO₂ foam for waterflooded residual oil recovery. *Fuel*, 234, 809-813.
- Gass, J., Poddar, P., Almand, J., Srinath, S. and Srikanth, H. (2006). Superparamagnetic Polymer Nanocomposites with Uniform Fe₃O₄ Nanoparticle Dispersions. *Advanced Functional Materials*, 16(1), 71-75.
- Gómez-Lopera, S. A., Plaza, R. C. and Delgado, A. V. (2001). Synthesis and Characterization of Spherical Magnetite/Biodegradable Polymer Composite Particles. *Journal of Colloid and Interface Science*, 240(1), 40-47.
- Gouy, G., (1909). Sur la constitution de la charge électrique ala surface d'un électrolyte. *Comptes rendus de l'Académie des sciences*, 149, 654-657.
- Guimarães, A. P. (2009). *Principles of nanomagnetism*. Heidelberg Germany ; New York: Springer.
- Guo, Q., Ji, L., Rajabov, V., Friedheim, J. E., Portella, C. and Wu, R. (2012). *Shale Gas Drilling Experience and Lessons Learned From Eagle Ford*. Paper presented at the SPE Americas Unconventional Resources

Conference, Pittsburgh, Pennsylvania USA.

- Guthrie, J., Sada, I. I. (1982). The acid catalysed condensation of phenol-4-sulphonic acid with formaldehyde. *Polymer*, 23(8), 1229-1232
- Hamaker, H. C. (1937). The London—van der Waals attraction between spherical particles. *Physica*, 4(10), 1058-1072.
- Harris, L. A., Goff, J. D., Carmichael, A. Y., Riffle, J. S., Harburn, J. J., St. Pierre, T. G. and Saunders, M. (2003). Magnetite Nanoparticle Dispersions Stabilized with Triblock Copolymers. *Chemistry of Materials*, 15(6), 1367-1377.
- Heller, J. P., Lien, C. L. and Kuntamukkula, M. S. (1985). Foamlike Dispersions for Mobility Control in CO₂ Floods. *Society of Petroleum Engineers Journal*, 25(04), 603-613.
- Henry, R. L., Fisher, D. R., Pennell, S. P. and Honnert, M. A. (1996). *Field test of foam to reduce CO₂ cycling*. Paper presented at the SPE/DOE Improved Oil Recovery Symposium.
- Hu, X., Hu, S., Jin, F. and Huang, S. (2017). *Physics of petroleum reservoirs*. New York, NY: Springer Berlin Heidelberg.
- Hu, Y., Meng, L., Niu, L. and Lu, Q. (2013). Facile Synthesis of Superparamagnetic Fe₃O₄@polyphosphazene@Au Shells for Magnetic Resonance Imaging and Photothermal Therapy. *Acs Applied Materials & Interfaces*, 5(11), 4586-4591.
- Hull, K. L., Sayed, M. and Al-Muntasheri, G. A. (2016). Recent Advances in Viscoelastic Surfactants for Improved Production From Hydrocarbon Reservoirs. *SPE Journal*, 21(04), 1340-1357

- Hunt, C. P., Moskowitz, B. M., and Banerjee, S. K. (1995). Magnetic Properties of Rocks and Minerals. *Rock Physics & Phase Relations*, 189-204..
- Jamaloei, B. Y., Kharrat, R. and Ahmadloo, F. (2009). *Selection of Proper Criteria in Flow Behavior Characterization of Low Tension Polymer Flooding in Heavy Oil Reservoirs*. Paper presented at the Kuwait International Petroleum Conference and Exhibition, Kuwait City, Kuwait.
- Jarrell, P. M., Fox, C., Stein, M. and Webb, S. (2002). Practical Aspects of CO₂ Flooding. Vol. 22. 2002: Richardson, Tex.: Henry L. Doherty Memorial Fund of AIME.
- Jin, Y., Jia, C., Huang, S. W., O'Donnell, M. and Gao, X. (2010). Multifunctional nanoparticles as coupled contrast agents. *Nature Communications*, 1(1), 41.
- Jolivet, J. P., Froidefond, C., Pottier, A., Chanéac, C., Cassaignon, S., Tronc, E. and Euzen, P. (2004). Size tailoring of oxide nanoparticles by precipitation in aqueous medium. A semi-quantitative modelling. *Journal of Materials Chemistry*, 14(21), 3281-3288.
- Jonas, T., Chou, S. and Vasicek, S. (1990). *Evaluation of a CO₂ Foam Field Trial: Rangely Weber Sand Unit*. Paper presented at the SPE Annual Technical Conference and Exhibition.
- Kapusta, S., Balzano, L. and Te Riele, P. M. (2011). *Nanotechnology Applications in Oil and Gas Exploration and Production*. Paper presented at the International Petroleum Technology Conference, Bangkok, Thailand.

- Karnanda, W., Benzagouta, M. S., AlQuraishi, A. and Amro, M. M. (2013). Effect of temperature, pressure, salinity, and surfactant concentration on IFT for surfactant flooding optimization. *Arabian Journal of Geosciences*, 6(9), 3535-3544.
- Kentish, S. E., & Stevens, and. W. (2001). Innovations in separations technology for the recycling and re-use of liquid waste streams. *Chemical Engineering Journal*, 84(2), 149-159.
- Kerney, U. (1994), *New recycling technologies for Fe/Zn waste acids from hot dip galvanizing*, in: Proceedings of Intergalva, Paris.
- Khalilinezhad, S. S. and Cheraghian, G. (2016). Mechanisms behind injecting the combination of nano-clay particles and polymer solution for enhanced oil recovery. *Applied Nanoscience*, 6(6), 923-931.
- Khalilinezhad, S. S., Cheraghian, G., Roayaei, E., Tabatabaee, H. and Karambeigi, M. S. (2017). Improving heavy oil recovery in the polymer flooding process by utilizing hydrophilic silica nanoparticles. *Energy Sources, Part A: Recovery, Utilization, and Environmental Effects*, 1-10.
- Kim, J., Park, S., Lee, J., Jin, S., Lee, J., Lee, I., Yang, I., Kim, J., Kim, S., Cho, M. and Hyeon, T. (2006). Designed Fabrication of Multifunctional Magnetic Gold Nanoshells and Their Application to Magnetic Resonance Imaging and Photothermal Therapy. *Angewandte Chemie International Edition*, 45(46), 7754-7758.
- Klekotka, U., Satula, D., Nordblad, P., and Kalska-Szostko, B. (2020). Layered magnetite nanoparticles modification – synthesis, structure, and

- magnetic characterization. *Arabian Journal of Chemistry*, 13(1), 1323-1334.
- Ko, S., Kim, E., Park, S., Daigle, H., Milner, T. E., Huh, C., Bennetzen, M. V. and Geremia, G. A. (2016). *Oil Droplet Removal from Produced Water Using Nanoparticles and Their Magnetic Separation*. Paper presented at the SPE Annual Technical Conference and Exhibition, Dubai, UAE.
- Krishnamoorti, R. (2006). Technology Tomorrow: Extracting the Benefits of Nanotechnology for the Oil Industry. *Journal of Petroleum Technology*, 58(11), 24-26.
- Lai, L. M. H., Goon, I. Y., Lim, M., Hibbert, D. B., Amal, R. and Gooding, J. J. (2011). Gold-coated magnetic nanoparticles as “dispersible electrodes” – Understanding their electrochemical performance. *Journal of Electroanalytical Chemistry*, 656(1), 130-135.
- Lake, L. W., Schmidt, R. L. and Venuto, P. B. (1992). A niche for enhanced oil recovery in the 1990s. *Oilfield Review*, 4(1), 55-61.
- Lam-Maldonado, M., Melo-Banda, J. A., Macias-Ferrer, D., Schacht, P., Mata-Padilla, J. M., de la Torre, A. I. R., Meraz Melo, M. A. and Domínguez, J. M. (2018). NiFe nanocatalysts for the hydrocracking heavy crude oil. *Catalysis Today*.
- Lambert, M., Marino, S., Anthony, T., Calvin, M., Gutierrez, S. and Smith, D. (1996). *Implementing CO₂ floods: no more delays!* Paper presented at the Permian Basin Oil and Gas Recovery Conference.
- Lamer, V. K. and Dinegar, R. H. (1950). Theory, Production and Mechanism of

- Formation of Monodispersed Hydrosols. *Journal of the American Chemical Society*, 72(11), 4847-4854
- Le, N. Y. T., Pham, D. K., Le, K. H. and Nguyen, P. T. (2011). Design and screening of synergistic blends of SiO₂nanoparticles and surfactants for enhanced oil recovery in high-temperature reservoirs. *Advances in Natural Sciences: Nanoscience and Nanotechnology*, 2(3), 035013.
- Lee, D., Cho, H., Lee, J., Huh, C. and Mohanty, K. (2015). Fly ash nanoparticles as a CO₂ foam stabilizer. *Powder Technology*, 283, 77-84.
- Li, L., Al-Muntasheri, G. A. and Liang, F. (2016). *Nanomaterials-Enhanced High-Temperature Fracturing Fluids Prepared with Untreated Seawater*. Paper presented at the SPE Annual Technical Conference and Exhibition, Dubai, UAE.
- Liu, H., Jin, X. and Ding, B. (2016). Application of nanotechnology in petroleum exploration and development. *Petroleum Exploration and Development*, 43(6), 1107-1115.
- Lo, C. K., Xiao, D. and Choi, M. M. F. (2007). Homocysteine-protected gold-coated magnetic nanoparticles: synthesis and characterisation. *Journal of Materials Chemistry*, 17(23), 2418-2427.
- Lu, A. H., Salabas, E. L. and Schuth, F. (2007). Magnetic nanoparticles: Synthesis, protection, functionalization, and application. *Angewandte Chemie-International Edition*, 46(8), 1222-1244.
- Lung, C. Y. K. and Matinlinna, J. P. (2012). Aspects of silane coupling agents and surface conditioning in dentistry: An overview. *Dental Materials*, 28(5), 467-477.

- Mahdavian, A. R. and Mirrahimi, M. A.-S. (2010). Efficient separation of heavy metal cations by anchoring polyacrylic acid on superparamagnetic magnetite nanoparticles through surface modification. *Chemical Engineering Journal*, 159(1), 264-271.
- Manshad, A. K., Rezaei, M., Moradi, S., Nowrouzi, I. and Mohammadi, A. H. (2017). Wettability alteration and interfacial tension (IFT) reduction in enhanced oil recovery (EOR) process by ionic liquid flooding. *Journal of Molecular Liquids*, 248, 153-162.
- Mantione, D., del Agua, I., Schaafsma, W., ElMahmoudy, M., Uguz, I., Sanchez-Sanchez, A., Sardon, H., Catro, B., Malliaras, G. G., Mecerreyes, D. (2017). Low-Temperature Cross-Linking of PEDOT:PSS Films Using Divinylsulfone. *Acs Applied Materials & Interfaces*, 9(21), 18254-18262.
- Marañón, E., Suárez, F., Alonso, F., Fernández, Y., and Sastre, H. (1999). Preliminary Study of Iron Removal from Hydrochloric Pickling Liquor by Ion Exchange. *Industrial & Engineering Chemistry Research*, 38(7), 2782-2786.
- Mascolo, M. C., Pei, Y. and Ring, T. (2013). Room Temperature Co-Precipitation Synthesis of Magnetite Nanoparticles in a Large pH Window with Different Bases. *Materials*, 6.
- Michalet, X., Pinaud, F. F., Bentolila, L. A., Tsay, J. M., Doose, S., Li, J. J., Sundaresa, G., Wu, A. M., Gambhir, S. S. and Weiss, S. (2005). Quantum dots for live cells, in vivo imaging, and diagnostics. *Science*, 307(5709), 538-544.

- Mohammed, M. I., Abdul Razak, A. A. and Shehab, M. A. (2017). Synthesis of Nanocatalyst for Hydrodesulfurization of Gasoil Using Laboratory Hydrothermal Rig. *Arabian Journal for Science and Engineering*, 42(4), 1381-1387.
- Moraes Silva, S., Tavallaie, R., Sandiford, L., Tilley, R. D. and Gooding, J. J. (2016). Gold coated magnetic nanoparticles: from preparation to surface modification for analytical and biomedical applications. *Chemical Communications*, 52(48), 7528-7540.
- Murtaza, M., Rahman, M. K. and Al-Majed, A. A. (2016). *Mechanical and Microstructural Studies of Nanoclay Based Oil Well Cement Mix under High Pressure and Temperature Application*. Paper presented at the International Petroleum Technology Conference, Bangkok, Thailand.
- Napper, D. H. (1977). Steric stabilization. *Journal of Colloid and Interface Science*, 58(2), 390-407.
- Narayanan, R. and El-Sayed, M. A. (2005). Catalysis with transition metal nanoparticles in colloidal solution: Nanoparticle shape dependence and stability. *Journal of Physical Chemistry B*, 109(26), 12663-12676.
- Neamtu, I., Rusu, A. G., Diaconu, A., Nita, L. E. and Chiriac, A. P. (2017). Basic concepts and recent advances in nanogels as carriers for medical applications. *Drug Delivery*, 24(1), 539-557.
- Neel, L. (1949). Theorie du trainage magnetique des ferromagnetiques en grains fins avec applications aux terres cuites. *Ann. Geophys.*, 5, 99-136.
- Negin, C., Ali, S. and Xie, Q. (2017). Most common surfactants employed in

- chemical enhanced oil recovery. *Petroleum*, 3(2), 197-211.
- Negro, C., Blanco, M. A., Lopez-Mateos, F., DeJong, A. M. C. P., LaCalle, G., Van Erkel, J., and Schmal, D. (2001). *Free acids and chemicals recovery from stainless steel pickling baths. Separation Science and Technology*, 36(7), 1543-1556.
- Odian, G. G. (2004). *Principles of polymerization* (4th ed.). Hoboken, N.J.: Wiley-Interscience.
- Oruwori, A. E., and Ikiensikimama, S. S. (2010). *Determination of Water Salinities in Hydrocarbon Bearing Reservoirs of Some Niger Delta Fields - Nigeria*. Paper presented at the Nigeria Annual International Conference and Exhibition, Tinapa - Calabar, Nigeria.
- Özdemir, T., Öztin, C., & Kınca, N. S. (2006). Treatment of Waste Pickling Liquors: Process Synthesis and Economic Analysis. *Chemical Engineering Communications*, 193(5), 548-563.
- Paria, S. and Khilar, K. C. (2004). A review on experimental studies of surfactant adsorption at the hydrophilic solid-water interface. *Advances in Colloid and Interface Science*, 110(3), 75-95.
- Parizad, A. and Shahbazi, K. (2016). Experimental investigation of the effects of SnO₂ nanoparticles and KCl salt on a water base drilling fluid properties. *The Canadian Journal of Chemical Engineering*, 94(10), 1924-1938.
- Park, J., An, K., Hwang, Y., Park, J., Noh, H., Kim, J., Park, J., Hwang, N. and Hyeon, T. (2004). Ultra-large-scale syntheses of monodisperse nanocrystals. *Nature Materials*, 3(12), 891-895.

- Park, Y., Huh, C., Ok, J. and Cho, H. (2019). One-Step Synthesis and Functionalization of High-Salinity-Tolerant Magnetite Nanoparticles with Sulfonated Phenolic Resin. *Langmuir*, 35(26), 8769-8775.
- Patzek, T., Wilt, M. and Hoversten, G. M. (2000). *Using Crosshole Electromagnetics (EM) for Reservoir Characterization and Waterflood Monitoring*. Paper presented at the SPE Permian Basin Oil and Gas Recovery Conference, Midland, Texas.
- Philipse, A. P., van Bruggen, M. P. B. and Pathmamanoharan, C. (1994). Magnetic silica dispersions: preparation and stability of surface-modified silica particles with a magnetic core. *Langmuir*, 10(1), 92-99.
- Piñeiro-Redondo, Y., Bañobre-López, M., Pardiñas-Blanco, I., Goya, G., López-Quintela, M. A. and Rivas, J. (2011). The influence of colloidal parameters on the specific power absorption of PAA-coated magnetite nanoparticles. *Nanoscale Research Letters*, 6(1), 383.
- Răcuciu, M., Creangă, D. E. and Airinei, A. (2006). Citric-acid-coated magnetite nanoparticles for biological applications. *The European Physical Journal E*, 21(2), 117-121.
- Rahmani, A. R., Bryant, S., Huh, C., Athey, A., Ahmadian, M., Chen, J. and Wilt, M. (2015). Crosswell Magnetic Sensing of Superparamagnetic Nanoparticles for Subsurface Applications. *SPE Journal*, 20(05), 1067-1082.
- Regel-Rosocka, M. (2010). A review on methods of regeneration of spent pickling solutions from steel processing. *Journal of Hazardous Materials*, 177(1), 57-69.

- Rockenberger, J., Scher, E. C. and Alivisatos, A. P. (1999). A New Nonhydrolytic Single-Precursor Approach to Surfactant-Capped Nanocrystals of Transition Metal Oxides. *Journal of the American Chemical Society*, 121(49), 11595-11596.
- Rognmo, A. U., Heldal, S. and Fernø, M. A. (2018). Silica nanoparticles to stabilize CO₂-foam for improved CO₂ utilization: Enhanced CO₂ storage and oil recovery from mature oil reservoirs. *Fuel*, 216, 621-626.
- Rosen, M. J. (1989). *Surfactants and interfacial phenomena* (2nd ed.). New York: Wiley.
- Ruíz-Baltazar, A., Esparza, R., Rosas, G., and Perez-Campos, R. (2015). Effect of the Surfactant on the Growth and Oxidation of Iron Nanoparticles. *Journal of Nanomaterials*, 2015.
- Sato, T., Iijima, T., Seki, M. and Inagaki, N. (1987). Magnetic-Properties of Ultrafine Ferrite Particles. *Journal of Magnetism and Magnetic Materials*, 65(2-3), 252-256
- Sharma, M. M., Zhang, R., Chenevert, M. E., Ji, L., Guo, Q. and Friedheim, J. (2012). *A New Family of Nanoparticle Based Drilling Fluids*. Paper presented at the SPE Annual Technical Conference and Exhibition, San Antonio, Texas, USA.
- Shaw, D. J. (1992). *Introduction to colloid and surface chemistry* (4th ed.). Oxford ; Boston: Butterworth-Heinemann.
- Sheng, J. J. (2011). *Modern Chemical Enhanced Oil Recovery* (pp. 371-387). Boston: Gulf Professional Publishing.
- Sihvola, A. (1999). *Electromagnetic Mixing Formulas and Applications* (1st

- ed.). London: Institution of Engineering and Technology..
- Solodov, A. N., Shayimova, J. R., Burilova, E. A. and Amirov, R. R. (2018). Polyethyleneimine-modified iron oxide nanoparticles: their synthesis and state in water and in solutions of ligands. *Colloid and Polymer Science*, 296(12), 1983-1993.
- Songvorawit, N., Tuittemwong, K., and Tuittemwong, P. (2011). Single Step Synthesis of Amino-Functionalized Magnetic Nanoparticles with Polyol Technique at Low Temperature. *ISRN Nanotechnology*, 2011.
- Stöber, W., Fink, A. and Bohn, E. (1968). Controlled growth of monodisperse silica spheres in the micron size range. *Journal of Colloid and Interface Science*, 26(1), 62-69.
- Sullivan, P. F., Gadiyar, B. R., Morales, R. H., Holicek, R. A., Sorrells, D. C., Lee, J. and Fischer, D. D. (2006). *Optimization of a Visco-Elastic Surfactant (VES) Fracturing Fluid for Application in High-Permeability Formations*. Paper presented at the SPE International Symposium and Exhibition on Formation Damage Control, Lafayette, Louisiana, USA.
- Sun, S. and Zeng, H. (2002). Size-Controlled Synthesis of Magnetite Nanoparticles. *Journal of the American Chemical Society*, 124(28), 8204-8205.
- Sun, X., Wu, Q., Zhang, J., Qing, Y., Wu, Y. and Lee, S. (2017). Rheology, curing temperature and mechanical performance of oil well cement: Combined effect of cellulose nanofibers and graphene nano-platelets. *Materials & Design*, 114, 92-101.

- Tadmor, R., Rosensweig, R. E., Frey, J. and Klein, J. (2000). Resolving the Puzzle of Ferrofluid Dispersants. *Langmuir*, *16*(24), 9117-9120.
- Tago, T., Hatsuta, T., Miyajima, K., Kishida, M., Tashiro, S. and Wakabayashi, K. (2002). Novel Synthesis of Silica-Coated Ferrite Nanoparticles Prepared Using Water-in-Oil Microemulsion. *Journal of the American Ceramic Society*, *85*(9), 2188-2194.
- Thanh, N. T. K., Maclean, N. and Mahiddine, S. (2014). Mechanisms of Nucleation and Growth of Nanoparticles in Solution. *Chemical Reviews*, *114*(15), 7610-7630.
- Thurmond Li, K. B., Huang, H., Clark Jr, C. G., Kowalewski, T. and Wooley, K. L. (1999). Shell cross-linked polymer micelles: stabilized assemblies with great versatility and potential. *Colloids and Surfaces B: Biointerfaces*, *16*(1), 45-54.
- Tomaszewska, M., Gryta, M., and Morawski, A. W. (1995). Study on the Concentration of Acids by Membrane Distillation. *Journal of Membrane Science*, *102*, 113-122.
- Trentler, T. J., Denler, T. E., Bertone, J. F., Agrawal, A. and Colvin, V. L. (1999). Synthesis of TiO₂ Nanocrystals by Nonhydrolytic Solution-Based Reactions. *Journal of the American Chemical Society*, *121*(7), 1613-1614.
- Tsai, Y. L., Liao, H. C., Cheng, P. I., Lee, C. J., Lee, H. T. and Tsai, Y. C. (2013). Synthesis and characterisation of superparamagnetic Fe₃O₄-SiO₂ nanoparticles and modification by grafting with chitosan. *International Journal of Nanotechnology*, *10*(10-11), 916-929.

- Ucbas, Y., Bozkurt, V., Bilir, K. and Ipek, H. (2014). Separation of Chromite from Serpentine in Fine Sizes using Magnetic Carrier. *Separation Science and Technology*, 49(6), 946-956.
- Verwey, E. J. W., Overbeek, J. T. G. and Nes, K. v. (1948). *Theory of the stability of lyophobic colloids; the interaction of sol particles having an electric double layer*. New York,: Elsevier Pub. Co.
- Vincent, B., Edwards, J., Emmett, S. and Jones, A. (1986). Depletion flocculation in dispersions of sterically-stabilised particles (“soft spheres”). *Colloids and Surfaces*, 18(2), 261-281.
- Viota, J. L., Delgado, A. V., Arias, J. L. and Durán, J. D. G. (2008). Study of the magnetorheological response of aqueous magnetite suspensions stabilized by acrylic acid polymers. *Journal of Colloid and Interface Science*, 324(1), 199-204.
- Wan, R. (2011). *Advanced well completion engineering* (3rd ed.). Waltham, MA: Gulf Professional Pub.
- Willott, J. D., Murdoch, T. J., Leermakers, F. A. M. and de Vos, W. M. (2018). Behavior of Weak Polyelectrolyte Brushes in Mixed Salt Solutions. *Macromolecules*, 51(3), 1198-1206.
- Wilt, M. J., Alumbaugh, D. L., Lee, K. H., Deszcz-Pan, M., Morrison, H. F. and Becker, A. (1995). Crosswell electromagnetic tomography: System design considerations and field results. *Geophysics*, 60, 871-885.
- Wu, C. S., Lin, F. Y., Chen, C. Y. and Chu, P. P. (2006). A polyvinyl alcohol/p-sulfonate phenolic resin composite proton conducting membrane. *Journal of Power Sources*, 160(2), 1204-1210.

- Wu, W., He, Q. G. and Jiang, C. Z. (2008). Magnetic Iron Oxide Nanoparticles: Synthesis and Surface Functionalization Strategies. *Nanoscale Research Letters*, 3(11), 397-415.
- Yazdani, F. and Seddigh, M. (2016). Magnetite nanoparticles synthesized by co-precipitation method: The effects of various iron anions on specifications. *Materials Chemistry and Physics*, 184, 318-323.
- Yee, C., Kataby, G., Ulman, A., Prozorov, T., White, H., King, A., Rafilovich, M., Sokolov, J. and Gedanken, A. (1999). Self-assembled monolayers of alkanesulfonic and -phosphonic acids on amorphous iron oxide nanoparticles. *Langmuir*, 15(21), 7111-7115
- Yeo, K, Lee, S., Lee, Y., Chung, Y. and Lee, I. (2007). Core–Satellite Heterostructure of Fe₃O₄–Pd Nanocomposite: Selective and Magnetically Recyclable Catalyst for Decarboxylative Coupling Reaction in Aqueous Media. *Chemistry Letters*, 37(1), 116-117.
- Ying, J. Y. and Sun, T. (1997). Research Needs Assessment on Nanostructured Catalysts. *Journal of Electroceramics*, 1(3), 219-238.
- Yoon, K., Kotsmar, C., Ingram, D. R., Huh, C., Bryant, S. L., Milner, T. E. and Johnston, K. P. (2011). Stabilization of Superparamagnetic Iron Oxide Nanoclusters in Concentrated Brine with Cross-Linked Polymer Shells. *Langmuir*, 27(17), 10962-10969.
- Yoon, K., Xue, Z., Fei, Y. P., Lee, J., Cheng, V., Bagaria, H. G., Huh, C., Bryant, S. L., Kong, S., Ngo, V. W., Rahmani, A. R., Ahmadian, M., Ellison, C. J. and Johnston, K. P. (2016). Control of magnetite primary particle size in aqueous dispersions of nanoclusters for high magnetic

- susceptibilities. *Journal of Colloid and Interface Science*, 462, 359-367.
- Yu, S. and Chow, G. M. (2004). Carboxyl group (–CO₂H) functionalized ferrimagnetic iron oxide nanoparticles for potential bio-applications. *Journal of Materials Chemistry*, 14(18), 2781-2786.
- Yuan, Y., Rende, D., Altan, C. L., Bucak, S., Ozisik, R. and Borca-Tasciuc, D. A. (2012). Effect of Surface Modification on Magnetization of Iron Oxide Nanoparticle Colloids. *Langmuir*, 28(36), 13051-13059.
- Zargartalebi, M., Barati, N. and Kharrat, R. (2014). Influences of hydrophilic and hydrophobic silica nanoparticles on anionic surfactant properties: Interfacial and adsorption behaviors. *Journal of Petroleum Science and Engineering*, 119, 36-43.
- Zhang, D. H., Li, G. D., Li, J. X. and Chen, J. S. (2008). One-pot synthesis of Ag–Fe₃O₄ nanocomposite: a magnetically recyclable and efficient catalyst for epoxidation of styrene. *Chemical Communications*(29), 3414-3416.
- Zhulina, E. B. and Rubinstein, M. (2012). Ionic strength dependence of polyelectrolyte brush thickness. *Soft Matter*, 8(36), 9376-9383.
- Zwanzig, R. and Mountain, R. D. (1965). High-Frequency Elastic Moduli of Simple Fluids. *The Journal of Chemical Physics*, 43(12), 4464-4471

Appendix

A. 1. van der Waals Interaction

The van der Waals interaction contains all interactions between molecules that originate from electrical interactions between the electron clouds in the molecules. The interaction contains three types of attractions: dipole–dipole interaction, dipole-induced dipole interaction, and London dispersion force. In nonpolar materials, the London dispersion force is the main source of the van der Waals interaction between two molecules. This interaction works only at very short distances, and decreases in inverse proportion to the sixth power of the distance (Shaw, 1992).

The concept of the London dispersion force can be extended to macroscopic bodies by summing all interactions between interparticle molecule pairs. Consequently, Hamaker derived the London dispersion interaction energy acting between two spherical particles.

The interaction energy between two particles containing q atoms per cubic cm is as follows:

$$E = - \int_{V_1} dv_1 \int_{V_2} dv_2 \frac{q^2 \lambda}{r^6} \quad (12),$$

where dv_1 , dv_2 , V_1 , and V_2 are the volume elements and total volumes of the two particles; r is the distance between dv_1 and dv_2 ; and λ is the London–van der Waals constant.

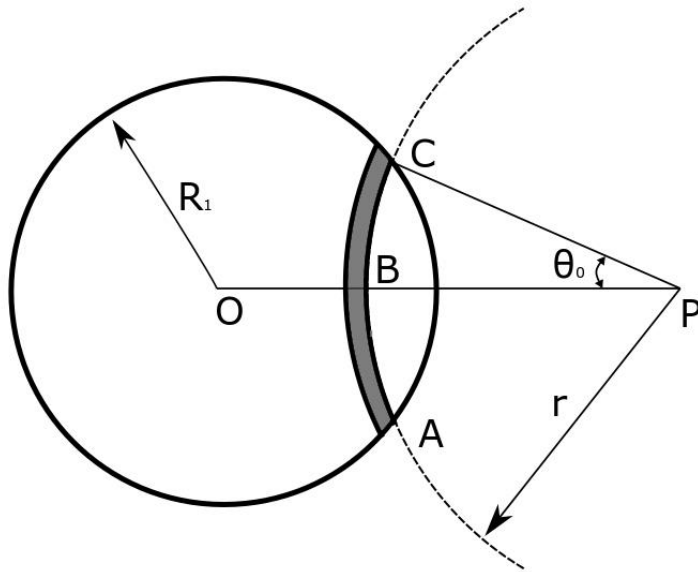


Figure A.1 Visual aid for calculation of the London–van der Waals force.
A sphere with radius R is cut out by a sphere around P at a distance of $OP = R$.

Considering a sphere with radius R , center O , and a point outside P at a distance of $OP = R$, the sphere around O will be cut out by a second sphere of radius r around P (Figure A.1). If the cut surface is ABC , the surface area of ABC can be calculated as follows:

$$\text{Surface } (ABC) = \int_0^{2\pi} d\phi \int_0^{\theta_0} d\theta r^2 \sin \theta \quad (13)$$

$$R_1^2 = R^2 + r^2 - 2rR \cos \theta \quad (14)$$

$$\text{Surface } (ABC) = \pi \frac{r}{R} \{R_1^2 - (R - r)^2\} \quad (15).$$

The volume elements can be calculated by the multiple of surface (ABC) and dr . Therefore, the London dispersion interaction with sphere O and an atom at point P is given by:

$$E_p = - \int_{R-R_1}^{R+R_1} \frac{\lambda q}{r^6} \pi \frac{r}{R} \{R_1^2 - (R - r)^2\} dr \quad (16).$$

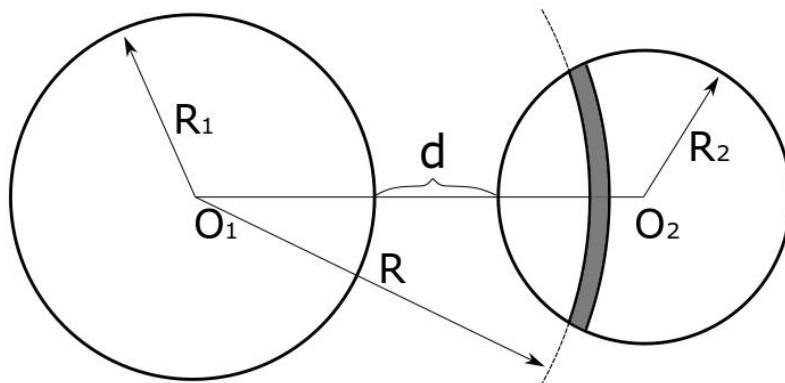


Figure A.2 Visual aid for calculation of the London–van der Waals force. A similar method to that formerly described is applied for a second sphere of radius R_2 .

The same method can be applied for a second sphere of radius R_2 that are distance C apart to obtain the total interaction energy (Figure A. 2)

$$\begin{aligned}
 E &= \int_{C-R_2}^{C+R_2} E_p q \pi \frac{R}{C} \{R_2^2 - (C - R)^2\} dR \\
 &= -\frac{\pi^2 q^2 \lambda}{C} \int_{C-R_2}^{C+R_2} \{R_2^2 \\
 &\quad - (C - R)^2\} dR \int_{R-R_1}^{R-R_2} \frac{\{R_1^2 - (R - r)^2\} dr}{r^5}
 \end{aligned} \tag{17}.$$

From the second integral, the equation becomes:

$$\begin{aligned}
 E &= -\frac{\pi^2 q^2 \lambda}{C} \int_{C-R_2}^{C+R_2} \{R^2 - (C - R)^2\} dR \times \frac{1}{12} \left\{ \frac{2R_1}{(R + R_1)^3} \right. \\
 &\quad \left. + \frac{2R_1}{(R - R_1)^3} + \frac{1}{(R + R_1)^2} - \frac{1}{(R - R_1)^2} \right\}
 \end{aligned} \tag{18},$$

and finally calculated as:

$$\begin{aligned}
 E &= -\frac{\pi^2 q^2 \lambda}{6} \left\{ \frac{2R_1 R_2}{C^2 - (R_1 + R_2)^2} + \frac{2R_1 R_2}{C^2 - (R_1 - R_2)^2} \right. \\
 &\quad \left. + \ln \frac{C^2 - (R_1 + R_2)^2}{C^2 - (R_1 - R_2)^2} \right\}
 \end{aligned} \tag{19}.$$

C is the distance between the two particles, and can be expressed as follows:

$$C = R_1 + R_2 + d \quad (20),$$

where d is the distance between the surfaces. If d is small enough compared to R_1 or R_2 , E can be approximated by:

$$E_{\text{vdW}} = -\frac{AR_1R_2}{(R_1 + R_2)6r} \quad (A = \pi^2 q^2 \lambda) \quad (21),$$

where A is the Hamaker constant (Hamaker, 1937).

A. 2. Electrostatic Interaction

In aqueous solution, ions in the solution gather around a charged surface, forming an electric double layer. The layer includes two regions: an inner region with ions adsorbed onto the charged surface, and a diffuse part where ions are randomly distributed according to the surface charge. Of these two regions, the diffuse region is more important because the overlapping of two diffuse regions causes electrostatic interaction between two charged surfaces.

Quantitative modeling of the diffuse region was carried out by Gouy (1909) and Chapman (1913), under the following assumptions: (i) the surface is flat, infinite, and uniformly charged; (ii) the ions are point charges and distributed according to the Boltzmann distribution; (iii) there is no solvent effect, without a dielectric constant that is uniform throughout the diffuse region; and (iv) there

is only single symmetrical electrolyte of charge number z .

Let the electric potential of a flat surface be ψ_0 , and that at a distance x from the surface ψ . If the surface is positively charged, the respective number of positive and negative ions per unit volume at points where the potential is ψ is as follows:

$$n_+ = n_0 \exp \left[\frac{-ze\psi}{kT} \right], \quad n_- = n_0 \exp \left[\frac{+ze\psi}{kT} \right] \quad (22),$$

where the formula, n_0 is the corresponding bulk concentration of each ionic species. Then, the net volume charge density ρ at points where the potential is ψ is given by:

$$\begin{aligned} \rho &= ze(n_+ - n_-) \\ &= zen_0 \left(\exp \left[\frac{-ze\psi}{kT} \right] - \exp \left[\frac{+ze\psi}{kT} \right] \right) \\ &= -2zen_0 \sinh \frac{ze\psi}{kT} \end{aligned} \quad (23).$$

Using Poisson's equation for a flat double layer, the relationship between ρ and ψ is as follows:

$$\frac{d^2\psi}{dx^2} = -\frac{\rho}{\epsilon} \quad (24),$$

where ϵ is permittivity. Combining these two equations, the following

differential equation is obtained

$$\frac{d^2\psi}{dx^2} = \frac{2ze n_0}{\epsilon} \sinh \frac{ze\psi}{kT} \quad (25).$$

The boundary condition can be set as follows:

$$\begin{aligned} \psi &= \psi_0 \quad (x = 0) \\ \psi &= 0, \frac{d\psi}{dx} = 0 \quad (x = \infty) \end{aligned} \quad (26).$$

With the boundary condition, the differential equation can be solved as follows:

$$\begin{aligned} \psi &= \frac{2kT}{ze} \ln \left(\frac{1 + \gamma \exp[-\kappa x]}{1 - \gamma \exp[-\kappa x]} \right) \\ \gamma &= \frac{\exp \left[\frac{ze\psi_0}{2kT} \right] - 1}{\exp \left[\frac{ze\psi_0}{2kT} \right] + 1} \quad (27), \\ \kappa &= \left(\frac{2e^2 n_0 z^2}{\epsilon kT} \right)^{\frac{1}{2}} = \left(\frac{2e^2 N_A c z^2}{\epsilon kT} \right)^{\frac{1}{2}} = \left(\frac{2F^2 c z^2}{\epsilon RT} \right)^{\frac{1}{2}} \end{aligned}$$

where $1/\kappa$ is called the Debye–Hückel length that means the effective double layer thickness. If $ze\psi_0/2kT \ll 1$, the equation can be simplified by the Debye–Hückel approximation ($\exp[ze\psi_0/2kT] \approx 1 + ze\psi_0/2kT$)

$$\psi = \psi_0 \exp[-\kappa x] \quad (28).$$

In a spherical interface, the Poisson–Boltzmann distribution takes the following form (Adamson and Gast, 1997; Shaw, 1992)

$$\nabla^2 \psi = \frac{1}{r^2} \frac{d}{dr} \left(r^2 \frac{d\psi}{dr} \right) = \frac{2ze n_0}{\epsilon} \sinh \frac{ze\psi}{kT} \quad (29).$$

The calculation of the interaction energy caused by overlapping of the diffuse regions between two particles is very complex. There is no exact analytical solution, but some approximate solutions exist. Verwey and Overbeek (1948) assumed that the interparticle distance is sufficiently large ($\exp[-\kappa H] \ll 1$) for the potential at any point between the particles. With this assumption, the potential between the particles is given by the sum of the potentials at that point for each particle in the absence of the other. Consequently, the electrostatic energy between two unequal particles is calculated as follows:

$$E_E = \frac{64\pi\epsilon a_1 a_2 k^2 T^2 \gamma_1 \gamma_2}{(a_1 + a_2) e^2 z^2} \exp[-\kappa H] \quad (30),$$

where a_1 and a_2 are the radii of two spherical particles, H is the shortest distance between the Stern layers of the particles, and z is the counter-ion charge. If the two particles are identical, the equation can be simplified as follows (Verwey

et al., 1948)

$$E_E = \frac{32\pi\epsilon a k^2 T^2 \gamma_1 \gamma_2}{e^2 z^2} \exp[-\kappa H] \quad (31).$$

If the Debye–Hückel approximation ($ze\psi_0/2kT \ll 1$, $\exp[ze\psi_0/2kT] \approx 1 + ze\psi_0/2kT$) is applied to the solution, the equation can be reduced to the following (Shaw, 1992)

$$E_E = 2\pi\epsilon a \psi_d^2 \exp[-\kappa H] \quad (32).$$

In the DLVO theory, the interaction between the particles is the sum of the van der Waals interaction and the electrostatic interaction. From the results from sections A. 1 and A. 2, the interaction between the particles in terms of the distance between particles is quantified as

$$E_{\text{tot}} = E_{\text{vdW}} + E_E \quad (33).$$

A typical interaction graph is shown in Figure A.3. From the graph the behavior of the particles can be determined from the distance between them. If the particles become closer than the distance where the energy barrier is, they will coagulate.

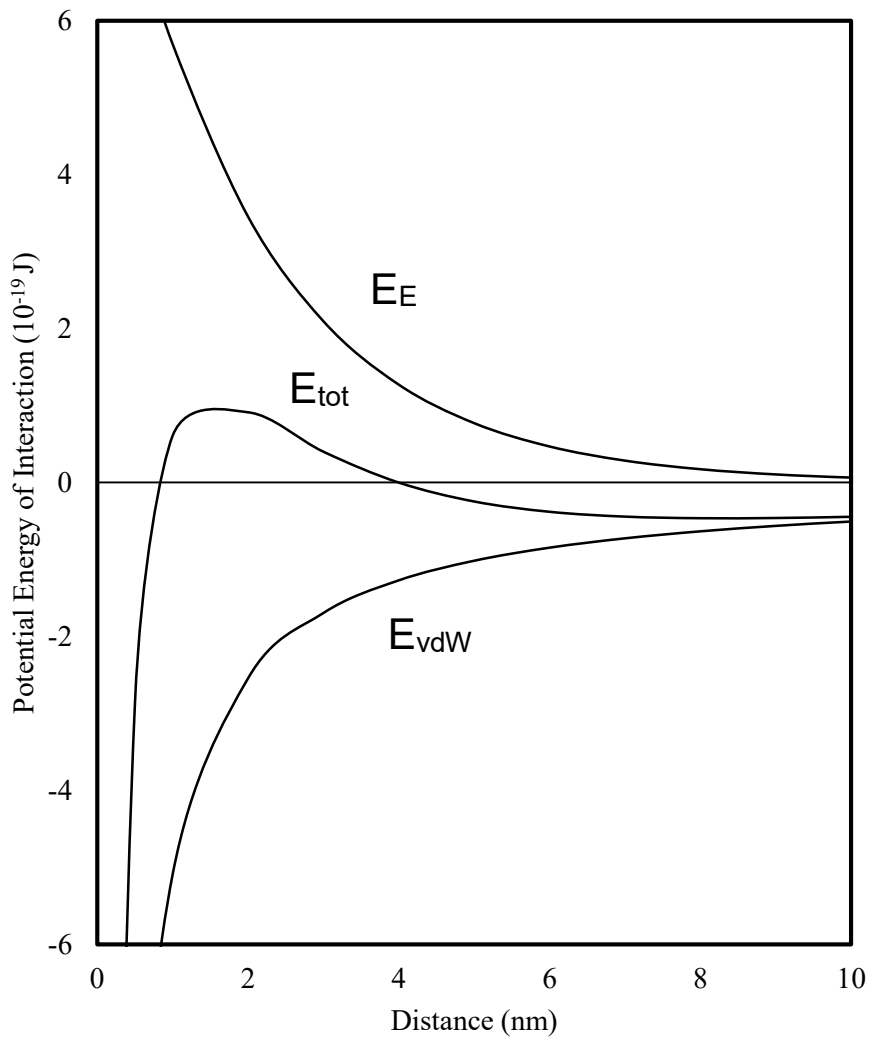


Figure A.3 A typical potential graph for DLVO interaction.

초 록

최근 나노입자를 석유공학 분야에 적용시키는 다양한 연구가 진행되고 있다. 이렇게 나노입자를 석유공학 분야에 적용시키기 위해선 먼저 나노입자의 합성 비용이 절감되어야 하며, 그러면서도 그렇게 합성된 나노입자들은 높은 염도와 같은 지하 유정의 극한 조건에서도 안정된 분산성을 유지할 수 있어야 한다. 본 논문에서는 이러한 두 가지 요소를 고려하면서, 지하 유정의 영상화에 적용될 수 있는 초상자성 산화철 나노입자를 합성하는 공정을 개발하였다. 먼저, 제철소의 산세 과정에서 발생하는 산화철 부산물로부터 초상자성 산화철 나노입자를 합성하는 방식이 개발되었다. 제철소 부산물을 철 이온 전구체로 사용하여, 고품질의 초상자성 산화철 나노입자를 공침법을 통해 합성할 수 있었다. 또한 고염도 조건에서도 분산이 가능한 초상자성 산화철 나노입자의 표면처리 방식도 개발되었다. 일반적으로 나노입자 표면처리에 사용되는 폴리에틸렌글리콜 (PEG), 폴리바이닐알코올 (PVA), 폴리아크릴산 (PAA)로는 고염도 조건에서도 분산이 가능한 나노입자를 합성할 수가 없었다. 하지만 술폰화된 페놀 레진 (SPR)을 이용하여 나노입자 표면처리를 진행해준 결과 중성~염기성 pH에서 5 wt% 염화나트륨 수용액에서 안정된 분산이 가능한 초상자성 산화철 나노입자를 합성할 수 있었다. SPR은 4-하이드록시 벤젠 술폰산과 폼알데하이드를 1:1 몰 비율로 혼합하여 가열해주는 방식으로 간단하게 합성할 수 있었다. 그 후 초상자성 산화철 나노입자를 SPR 용액 안에서 공침시켜주어 초상자성 산화철 나노입자의

합성과 표면처리를 한 번의 공정으로 완료할 수 있었다. 또한 산성 조건에서의 SPR 코팅의 안정성을 높이기 위해 PVA를 이용한 가교결합을 진행하였다. 이렇게 가교결합 반응을 해준 결과 산성 조건에서도 5 wt% 염화나트륨 수용액에서 분산이 가능한 초상자성 산화철 나노입자를 합성할 수 있었다. 또한 가교결합 반응을 진행한 초상자성 산화철 나노입자의 경우 칼슘 이온 같은 이가 양이온 용액에서도 향상된 분산성을 갖고 있음을 확인할 수 있었다. 이렇게 합성된 나노입자들의 물리/화학적 특성은 입도분포 분석, 제타전위 측정, 투과 전자현미경 및 X선 분광분석, 진동시료 자화율 측정, 열중량 분석 방법을 통해 분석되었다. 요약하여 말하면, 유정 개발 과정에서 지하 구조 영상화에 사용될 수 있는 초상자성 산화철 나노입자의 합성 공정이 (i) 제철소 부산물과 같은 저렴한 원료로부터, (ii) 저렴한 폴리머와 (iii) 복잡한 합성 과정 없이 단순히 혼합, 가열해주는 방식을 통한 표면처리를 통해 개발되었다.

핵심어: 산화철 나노입자; 나노입자 분산; 나노입자 표면 개질; 고염도 분산성; 술폰화된 페놀 레진; 단일 과정 표면처리

학번: 2013-23179